High Pressure Quantum Oscillation Study of BiTeI and Bi_2Te_3

Hong'En Tan

Churchill College

University of Cambridge

A thesis submitted for the degree of

Doctorate of Philosophy

Easter 2018

Declaration

This dissertation is the result of my own work and includes nothing which is the outcome of work done in collaboration except as specified in the text and in the acknowledgments. The total length of this dissertation does not exceed sixty thousand words.

Hong'En Tan
June 2018

High Pressure Quantum Oscillation Study of BiTeI and Bi_2Te_3

Hong'En Tan

Abstract

The work presented in this thesis investigates the behaviour of the Rashba semiconductor BiTeI and of the topological insulator Bi_2Te_3 under pressure. Using Shubnikov-de Haas quantum oscillation measurements, the evolution of the Fermi surface of both materials was tracked as a function of pressure.

At ambient pressure, two distinct quantum oscillation frequencies in BiTeI, corresponding to inner and outer Fermi surface orbits as a result of spin-splitting caused by the Rashba effect, were observed. Using a model Hamiltonian with a Rashba interaction term to model this system, experimental results were fitted to determine model parameters. Based on this model, carrier densities for the samples were calculated and there was good agreement with Hall effect measurements. The phase of the oscillations showed that both Fermi surfaces have a Berry phase of π associated with them, consistent with theoretical predictions for a Rashba system.

As pressure is applied, it was observed that the inner Fermi surface expands while the outer Fermi surface shrinks. Phase analysis of the oscillations showed deviations from the ambient pressure value, hinting at a topological transition.

For Bi_2Te_3 , we report the observation of two oscillation frequencies ($\sim$ 40 T and $\sim$ 340 T) at ambient pressures. Based on the angular dependence of the oscillation frequencies, phase analysis, and comparison against band structure from published ARPES results, it is deduced that the higher frequency oscillation corresponds to the surface state of Bi_2Te_3. Non-linear behaviour in the Hall measurement also suggests the presence of multiple bands, and a two-band model with parameters derived from quantum oscillation measurements is used to fit the experimental data.

Under pressure, a slight decrease in the low field Hall coefficient and a new frequency appearing at $\sim$ 20 kbar was observed. These may be signatures of a change in the Fermi surface of Bi_2Te_3 caused by an electronic topological transition.

Acknowledgements

This work would not be possible without the help and support of a number of people. In particular, I would like to thank

- my supervisor, Dr Malte Grosche, for taking me on as a PhD student, having the patience to explain complicated ideas to me, as well as his guidance and friendly support in all my work.
- Prof. Geetha Balakrishnan for providing plentiful high quality samples to study.
- Dr Mike Sutherland for his support with the dilution refrigerator; Dr Jordan Baglo and Xiaoye Chen for their help, advice and company in running/assembling/repairing equipment, as well as late night discussions of physics in the big fridge room.
- Prof. John Cooper for assisting and allowing me to run experiments on his 15T system, and Hui Chang for his assistance with setting up the 15T system.
- Dr Patricia Alireza, Philip Brown and Konstantin Semeniuk for their help in pressure related work.
- Jiasheng Chen and Hajime Shinohara for their guidance in using the X-ray system.
- Dan Cross and Mariusz Naguszewski for providing cryogenic liquid so that experiments can be carried out.
- A*STAR for providing the scholarship and funding to study in Cambridge.

I would also like to thank my housemates Jianding, Tiantian and Rita, as well as my A*STAR Singaporean friends for their company and fun times; John and Diane Lister, Ken, Cheryl and the Tuesday night Bible study group people for their support and prayers; my parents and family for their unconditional love and support for me.

Finally, I would also like to thank my wife, whom I have met during my time in Cambridge, for her patience, love and support throughout this period.

The works of the Lord are great, sought out of all them that have pleasure therein.

Psalm 111:2, KJV

Contents

List of Figures

List of Tables

Chapter 1

Introduction

From its days of infancy when physicists calculated the energy levels of the hydrogen atom using Bohr's model, to manipulating single atoms and engineering designer electronics for the modern-day consumer, our understanding of quantum physics has grown tremendously over the last century. Starting from single particle systems, we have made considerable progress in our attempt to understand many-body systems, many of which such as semiconductors feature in our computer-dominated everyday lives.

Our understanding of modern day condensed matter physics has been shaped enormously by two important theories developed by Landau – the Fermi liquid theory [1] and his theory of phase transitions [2].

The former enables us to understand why a seemingly complicated and computationally intractable system of $\sim 10^{23}$ interacting particles can be transformed into a smaller system whose particles do not scatter from one another, turning it into a much more manageable problem. Under such a transformation, the net effect of the particle-particle interactions can be viewed as a renormalization of the dynamical properties of the particles (e.g. mass) while properties such as charge, spin, and momentum remain unchanged. The particles in such a system are given the name quasi-particles. In spite of its simplicity, this theory is very successful in explaining and predicting the behaviour of many materials.

The latter provides an elegant and powerful way to describe phase transitions by expanding the free energy of the system in powers of an 'order parameter' of the system. A phase transition in the system then occurs when the order parameter is no longer invariant under a symmetry operation. For example, continuous translational symmetry is broken when water freezes into ice, magnetism breaks rotational symmetry, while type-I superconductivity breaks the more abstract gauge symmetry. This theory of symmetry breaking is also a macroscopic theory, and it can be used to explain different types of phase transitions even though the microscopic details of the systems might be vastly different.

As successful as these theories are, it is those materials that show deviation from standard theory that make us realise the limitations of our existing framework so that

boundaries of our understanding can be extended and new frontiers of research can be attained. Over the past few decades, there are a whole host of materials that have been found to violate Fermi liquid theory. In those systems, the assumptions that underlie Fermi liquid behaviour break down and the electron-electron interactions become important, resulting in strongly correlated electron motion. These highly correlated electron systems often exhibit collective modes that give rise to emergent novel states of matter, which could lead to a new generation of devices.

Our understanding of phase transitions from the point of symmetry breaking was also challenged when the (integer) quantum hall (QH) effect was discovered in 1980 [3]. It was found that the QH state – formed when a sufficiently strong magnetic field is applied to electrons confined in a plane – is not characterised by any kind of symmetry breaking order that physicists were familiar with. The magnetic field causes electrons in the QH state to circulate in quantised orbits, and the electrons in the bulk do not contribute to the conductivity – the system behaves like an insulator. However, electrons that are near the edges do contribute to the conductivity by performing a skipping motion along the boundary, moving in opposite directions along opposite sides of the sample. We now have a state that behaves like an insulator in the bulk, but conducts current along the edges – a state quite distinct from that in a traditional insulator. Physicists later found that there are deep underlying ideas related to topology, and thus coined the name topological order for this new type of phase.

In mathematics, topology is the study of the property of spaces that remain invariant under continuous deformation. Thus, the commonly used example of a doughnut and a coffee cup are considered topologically equivalent (genus of 1) as they can be continuously deformed into one another. A similar idea applies to topological order – the Hamiltonian describing such a state cannot be adiabatically changed ('deformed') into another without destroying such a topological state. Analogous to the genus of the doughnut, a topological invariant can be calculated for such systems to differentiate between the topological and topologically trivial cases. For the integer QH state, it turns out that Hall conductivity is proportional to the topological invariant of the system called the first Chern number [4, 5], providing an explanation to the robustness of the Hall plateaus seen in the experiments.

This topological behaviour was first predicted [6] and then experimentally observed [7] in 2D HgCdTe quantum wells without the need for an external field. It turns out that the crucial ingredient is strong spin-orbit interaction; and the important mechanism that takes place in such systems is the inversion of conduction and valence bands caused by the spin-orbit interactions – lower energy states that should be below the energy gap now appear above the gap. Such a 'twisting' of the electronic states cannot be easily

'unwound', giving this material its topological nature, and a new class of materials called topological insulators (TI) was born. Like the QH state, they exhibit highly conducting surface states, but are insulating in the bulk. Subsequently, the first generation of 3D TIs were predicted [8] and experimentally verified [9] in Bi_xSb_{1-x} , followed by the second generation of 3D TIs in a wide variety of materials (e.g. Bi_2Te_3 and Bi_2Se_3) [10, 11, 12].

Topological insulators are exciting not solely because they represent a new class of quantum matter, but also due to the possible applications made possible by the surface states exhibited by them. Due to the coupling between spin and momentum on the metallic surface states, TIs are ideal candidates for spintronics devices [13, 14]. An even more tantalising possibility offered by TIs is the generation of particle-like excitations when ferromagnets or superconductors are placed in close proximity to them. For the former, exotic composite particles called anyons which obeys neither Bose nor Fermion statistics are predicted to appear [15], while in the latter, the interface between the superconductor and the TI is predicted to host Majorana particles [16] (quasi-particles that are their own antiparticles) that could be used for quantum computing [17].

Recently, it was also predicted that effect of the spin-orbit interaction in BiTeI can be tuned by the application of pressure [18]. At a critical pressure, band inversion occurs and the material transitions from being a trivial insulator to a topological insulator. This thesis investigates the properties of BiTeI as well as the TI material Bi_2Te_3 under pressure using Shubnikov-de Haas (SdH) quantum oscillation measurements. Experimentally, we mainly used a piston-cylinder cell to pressurise the samples, and the resistivities of the samples were measured up to high fields using three different systems (two in Cambridge and one in the National High Magnetic Field Laboratory (NHMFL) in Tallahassee).

The structure of this thesis is organised as follows:

- Chapter 2 presents the theoretical background associated with quantum oscillations and the quantities that can be derived from the experimental data. An overview of the Hall effect is also outlined here.

- Chapter 3 presents the experimental techniques and methods used in this work. Various cryostats and probes, sample preparation methods, as well as high pressure techniques are detailed here.

- Results for the Rashba semi-conductor BiTeI are presented and discussed in Chapter 4. Hall and SdH measurements allow us to track the evolution of the Fermi surface as a function of pressure for three samples with different carrier concentrations.

- Results for the topological insulator Bi_2Te_3 are presented and discussed in Chapter 5. At ambient pressure, two frequencies – one of which is believed to be from the surface states – were observed in the SdH measurements. An additional frequency was observed at higher pressures, which we believe is a signature of an electronic topological transition reported previously.

Chapter 2

Theoretical background

2.1 Quantum Oscillations

2.1.1 Electrons in a Magnetic Field

For the motion of electrons in a magnetic field B, we use a semi-classical approach by equating the rate of change of momentum to the Lorentz force [19, 20]:

$$\hbar \frac{d\boldsymbol{k}}{dt} = -e\boldsymbol{v} \times \boldsymbol{B}, \tag{2.1}$$

where $\boldsymbol{k}$ is the wavevector of a Bloch electron, e is the charge of the electron and $\boldsymbol{v}$ is the velocity of the electron which is related to the energy E by

$$\boldsymbol{v} = \frac{1}{\hbar} \nabla_{\boldsymbol{k}} E. \tag{2.2}$$

From these two simple equations, we are able to draw several important conclusions regarding the motion of electrons in a magnetic field:

- Since the Lorentz force is perpendicular to $\boldsymbol{v}$, no work is done on the electron
  $\implies$ E remains constant as $\boldsymbol{k}$ changes in time
- $\dot{\boldsymbol{k}}$ is normal to $\boldsymbol{v}$, and $\boldsymbol{v}$ is normal to the constant E surface
  $\implies$ $\dot{\boldsymbol{k}}$ is tangential to the constant E surface
- $\dot{\boldsymbol{k}}$ is normal to B
  $\implies$ the possible electron orbits in k-space are the intersections between the constant energy surfaces with planes normal to the magnetic field
- Integrating equation 2.1 with time, we obtain

  $$(\boldsymbol{k} - \boldsymbol{k}_0) = \frac{e}{\hbar} \boldsymbol{B} \times (\boldsymbol{R} - \boldsymbol{R}_0), \tag{2.3}$$

  where $\boldsymbol{R}$ is the position vector of the electron in its real space trajectory with the constants from the integration indicated by the suffix zero. Equation 2.3 implies

that the real space orbits projected onto a plane normal to $\boldsymbol{B}$ are scaled versions of the k-space orbits, rotated 90° in its plane with respect to the k orbit. The scaling factor is given by $\eta = |e\boldsymbol{B}/\hbar|$.

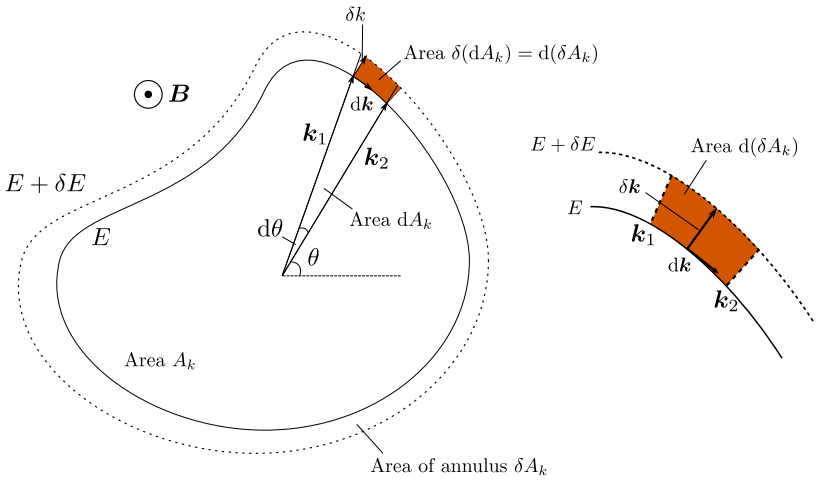

Figure 2.1: Left: Geometrical representation of the various quantities used for deriving the frequency of the cyclotron motion, for a particular component of $\boldsymbol{k}$ perpendicular to $\boldsymbol{B}$. Right: Enlarged segment in which the electron traverses from $\boldsymbol{k}_1$ to $\boldsymbol{k}_2$.

Consider a section of a k-space orbit of constant energy E in a plane perpendicular to the magnetic field B (see Figure 2.1). The time $\mathrm{d}t$ required to traverse a segment $\mathrm{d}\boldsymbol{k}$ of the orbit between k_1 and k_2 is given by

$$\mathrm{d}t = \frac{\hbar^2}{e} \frac{\mathrm{d}\boldsymbol{k}}{|\nabla_{\boldsymbol{k}} E \times \boldsymbol{B}|}, \tag{2.4}$$

where we have used equations 2.1 and 2.2. Resolving $\nabla_{\boldsymbol{k}}$ into components parallel $\nabla_{\boldsymbol{k}_\parallel}$ and perpendicular $\nabla_{\boldsymbol{k}_\perp}$ to the magnetic field, the component parallel to the magnetic field does not contribute to the cross product and we obtain

$$\mathrm{d}t = \frac{\hbar^2}{eB} \frac{\mathrm{d}\boldsymbol{k}}{|\nabla_{\boldsymbol{k}_\perp} E|} = \frac{\hbar^2}{eB} \frac{\mathrm{d}\boldsymbol{k}}{\delta E / \delta \boldsymbol{k}}, \tag{2.5}$$

where $\delta\boldsymbol{k}$ is the change in $\boldsymbol{k}$ (normal to the orbit of energy E) that corresponds to a change δE of E. [1]

Since $\delta\boldsymbol{k}$ is normal to $\mathrm{d}\boldsymbol{k}$, the quantity $\delta k\ \mathrm{d}k$ represents the area element between orbits of energy E and $E+\delta E$. Thus, the time taken for the electron to traverse between $\boldsymbol{k}_1$ and $\boldsymbol{k}_2$ is given by

[1] This can be seen by writing $\delta E = \nabla_{\boldsymbol{k}_\perp} E \cdot \delta\boldsymbol{k}$ and noting that $\nabla_{\boldsymbol{k}_\perp} E$ is perpendicular both to the magnetic field and to the orbit of energy E, i.e. parallel to $\delta\boldsymbol{k}$. Thus $\delta E = |\nabla_{\boldsymbol{k}_\perp} E| \delta k$.

$$t_{1\to 2} = \int_{t_1}^{t_2} \mathrm{d}t = \frac{\hbar^2}{eB}\frac{1}{\delta E}\int_{\boldsymbol{k}_1}^{\boldsymbol{k}_2} \delta k \; \mathrm{d}k = \frac{\hbar^2}{eB}\frac{\mathrm{d}(\delta A_k)}{\delta E}, \tag{2.6}$$

where $\mathrm{d}(\delta A_k)$ is the shaded $\boldsymbol{k}$-space area element between orbits of energy E and $E+\delta E$.

For a closed (cyclotron) orbit where $\boldsymbol{k}_1 = \boldsymbol{k}_2$, the time taken to traverse the loop is known as the cyclotron period τ_c, and the area element is integrated up to become the area of the annulus δA_k. In the limit where $\delta E \to 0$, we obtain

$$\tau_c = \frac{\hbar^2}{eB}\frac{\partial A(E, k_\parallel)}{\partial E}. \tag{2.7}$$

Since the cyclotron frequency $\omega_c = eB/m_c^*$, we can express the cyclotron mass m_c^* as

$$m_c^* = \frac{eB}{2\pi/\tau_c} = \frac{\hbar^2}{2\pi}\frac{\partial A(E, k_\parallel)}{\partial E}, \tag{2.8}$$

where we have emphasised that the area A depends on the energy E of the particular constant energy surface and on the component of $\boldsymbol{k}$ parallel to $\boldsymbol{B}$ at which the section is taken.

2.1.2 Quantisation of Energy Levels

For free electrons in a magnetic field, their energy states are quantised into Landau levels by the magnetic field. The Hamiltonian describing the system is given by:

$$\mathcal{H} = \frac{1}{2m^*}(\hat{\mathcal{P}}_{0x}^2 + \hat{\mathcal{P}}_{0y}^2 + \hat{\mathcal{P}}_{0z}^2), \quad \hat{\mathcal{P}}_{0i} = \hat{\mathcal{P}}_i - e\hat{A}_i, \tag{2.9}$$

where m^* is the effective mass of the electrons, $\hat{\boldsymbol{\mathcal{P}}}$ is the momentum operator, and $\mathbf{A}$ is the vector potential of the magnetic field $\mathbf{B}$ given by $\mathbf{B} = \nabla \times \mathbf{A}$.

Taking the magnetic field to be pointing in the z-direction, a suitable gauge chosen for $\mathbf{A}$ is the Landau gauge $\mathbf{A} = (-By, 0, 0)$. Substituting into the Hamiltonian, it becomes

$$\mathcal{H} = \frac{1}{2m^*}\left[(\hat{\mathcal{P}}_x + eB\hat{y})^2 + \hat{\mathcal{P}}_y^2 + \hat{\mathcal{P}}_z^2\right]. \tag{2.10}$$

Note that the Hamiltonian commutes with $\hat{\mathcal{P}}_x$ and $\hat{\mathcal{P}}_z$, thus the operators can be replaced with their respective physical quantities $P_x = \hbar k_x$ and $P_z = \hbar k_z$. The energy states E are given by the eigenvalues of the Hamiltonian $\mathcal{H}\psi = E\psi$,

$$\frac{1}{2m^*}\left[(\hbar k_x + eB\hat{y})^2 + \hat{\mathcal{P}}_y^2 + (\hbar k_z)^2\right]\psi = E\psi. \tag{2.11}$$

Equation 2.11 has the form of a 1-D harmonic oscillator centred about y_0 if we make

the substitution $y_0 = -\hbar k_x/eB$ and rearrange the terms:

$$\left[\frac{\hat{\mathcal{P}}_y^2}{2m^*} + \frac{(eB)^2}{2m^*}(\hat{y} - y_0)^2\right]\psi = (E - E_z)\psi, \tag{2.12}$$

with the angular frequency $\omega = eB/m^*$ and eigenvalues $E - E_z = (n + 1/2)\hbar\omega$. Thus, the energy values of an electron in a magnetic field are given by

$$E_n = \frac{\hbar^2 k_z^2}{2m^*} + (n + \frac{1}{2})\hbar\omega, \quad \omega = \frac{eB}{m^*}. \tag{2.13}$$

2.1.3 Quantisation of Electron Motion

The Bohr-Sommerfeld quantisation rule for periodic motion states that

$$\oint \boldsymbol{p} \cdot \mathrm{d}\boldsymbol{q} = (n + \gamma)2\pi\hbar, \tag{2.14}$$

where $\boldsymbol{p}$ and $\boldsymbol{q}$ are the canonically conjugated momentum and position variables with the integral taken over a complete period of motion at constant energy, n is an integer, and γ is a phase factor that will be discussed in the subsequent section. For an electron in a magnetic field, the appropriate meanings for the momentum and position variables are

$$\begin{aligned} \boldsymbol{p} &= \hbar\boldsymbol{k} - e\boldsymbol{A}, \\ \boldsymbol{q} &= \boldsymbol{R}, \end{aligned} \tag{2.15}$$

where $\boldsymbol{A}$ is the vector potential of $\boldsymbol{B}$. The integral can be rewritten using equation 2.3 and evaluated as

$$\begin{aligned} \oint (\hbar\boldsymbol{k} - e\boldsymbol{A}) \cdot \mathrm{d}\boldsymbol{R} &= -e \oint (\boldsymbol{R} \times \boldsymbol{B}) \cdot \mathrm{d}\boldsymbol{R} - e \int_s (\nabla \times \boldsymbol{A}) \cdot \mathrm{d}\boldsymbol{s} \\ &= e\left(\boldsymbol{B} \cdot \oint (\boldsymbol{R} \times \mathrm{d}\boldsymbol{R}) - \int_s \boldsymbol{B} \cdot \mathrm{d}\boldsymbol{s}\right), \end{aligned} \tag{2.16}$$

where we have dropped the constants of integration $\boldsymbol{R}_0$ and $\boldsymbol{k}_0$ as they do not contribute in a complete cycle, applied the simple identity of vector triple products to reorder the variables for the first term, and used Stoke's theorem for the second.

For the first term, the standard results in vector calculus give

$$\boldsymbol{B} \cdot \oint (\boldsymbol{R} \times \mathrm{d}\boldsymbol{R}) = \boldsymbol{B} \cdot 2\boldsymbol{A}_R = 2\Phi, \tag{2.17}$$

where $A_R = |\boldsymbol{A}_R|$ is the projection of the real-space area in the plane normal to the magnetic field and Φ is the magnetic flux; while the second term simply gives $-\Phi$.

Coupling these results together, we obtain the quantisation rule for real-space area

$$A_R = \frac{\Phi}{B} = (n+\gamma)\frac{2\pi\hbar}{eB}. \tag{2.18}$$

Another way to view this quantisation rule is that the motion of an electron in a magnetic field is such that the magnetic flux through its real-space orbit is quantised into units of $2\pi\hbar/e$.

In terms of $\boldsymbol{k}$-space orbits, we apply the scaling factor $\eta = eB/\hbar$ to obtain

$$\begin{aligned} A_k(E, k_\parallel) &= \eta^2 A_R \\ &= (n+\gamma)\frac{2\pi eB}{\hbar}. \end{aligned} \tag{2.19}$$

Equation 2.19 is known as the Onsager relation and it constrains the allowed values of $\boldsymbol{k}$ in a magnetic field. For a given n and B, a definite value of A_k that is not dependent on the component of $\boldsymbol{k}$ along the field direction is specified. Thus the effect of the magnetic field is to restrict the electron $\boldsymbol{k}$-states into a series of tubes in $\boldsymbol{k}$-space, each parallel to the magnetic field, with cross-sectional area A_k. Figure 2.2(a) shows a sketch of a spherical Fermi surface in a magnetic field, where the chemical potential of the Fermi surface is represented by the dashed line and the permitted states now lie on the Landau tubes.

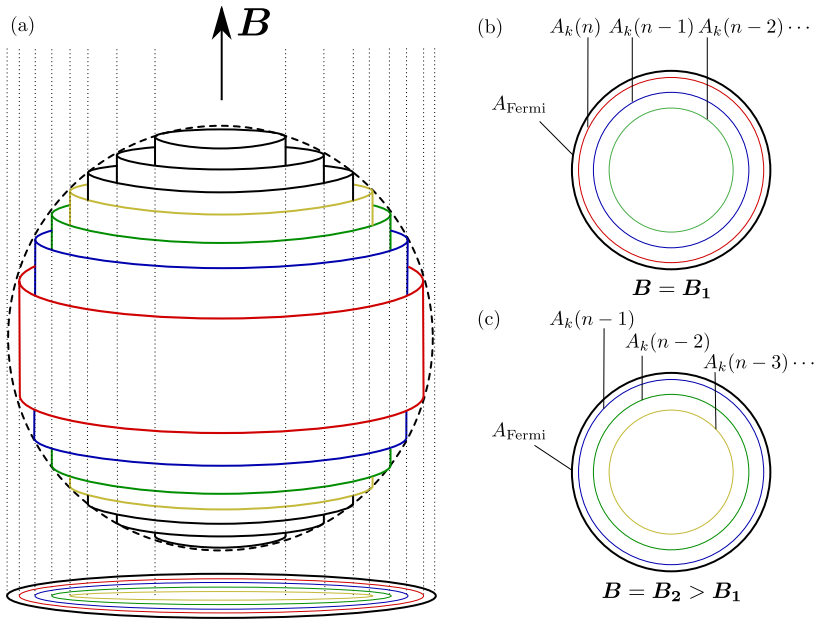

Figure 2.2: (a) Schematic of a spherical Fermi surface rearranged into Landau tubes. (b), (c) Sketch showing the evolution of the Landau tubes when the magnetic field is increased from $\boldsymbol{B}_1$ to $\boldsymbol{B}_2$.

Referring to equation 2.19, the $\boldsymbol{k}$-space area varies linearly with B, which implies that the Landau tubes expands (shrinks) when the field increases (decreases). We can see that as the field increases, there would always be Landau tubes crossing the constant

energy surface. However, the crossings that occur at the extremal orbits contribute most to the modulation of the density of states (more detailed explanation given in [21] or [20]), thus we will only focus on the Landau tube crossings that correspond to the extremal orbits.

Figures 2.2(b) and (c) illustrates the evolution of the Landau tubes, projected onto a plane normal to the field, as the field is increased. The outermost ring A_{Fermi}, represents the largest cross-sectional area a Landau tube can take, and for our hypothetical spherical Fermi surface, also corresponds to its extremal area. Suppose the n^{th} Landau tube (red) crosses the extremal orbit at a field $B = B_1$, we have

$$\frac{A_{\text{Fermi}}}{B_1} = (n + \gamma)\frac{2\pi e}{\hbar}. \tag{2.20}$$

Suppose again that when the field is swept to $B = B_2$, the $(n-1)^{\text{th}}$ Landau tube (blue) crosses the Fermi level, which would mean that the $(n-1)^{\text{th}}$ Landau tube now has the same cross-sectional area as the n^{th} Landau tube when the field was at $B = B_1$, i.e.

$$\frac{A_{\text{Fermi}}}{B_2} = (n - 1 + \gamma)\frac{2\pi e}{\hbar}. \tag{2.21}$$

Taking the difference between these two equations, we obtain a period T for the crossings

$$T = \left(\frac{1}{B_1} - \frac{1}{B_2}\right) = \frac{2\pi e}{\hbar}\frac{1}{A_{\text{Fermi}}}, \tag{2.22}$$

and the frequency F

$$F = (T)^{-1} = \frac{\hbar}{2\pi e}A_{\text{Fermi}}. \tag{2.23}$$

Here we have the famous *Onsager relation* that relates the frequency of crossings to the extremal cross-sectional area of the Fermi surface normal to the magnetic field. Whenever the field is swept, the successive crossings of the Landau tubes lead to a periodic modulation of the electronic density of states, which will show up as an oscillatory component in the quantity we are measuring. For example, the two most common experimental setups to observe quantum oscillations are: measuring the magnetoresistance oscillations in transport measurements (Shubnikov-de Haas effect), or probing the oscillatory behaviour in the magnetisation (de Haas-van Alphen effect).

2.1.4 Lifshitz-Kosevich Theory

The semi-classical treatment of the quantisation of electron motion under a magnetic field in the previous section gives us a qualitative feel of the oscillatory behaviour ex-

hibited by metallic materials. The full quantitative description given by Lifshitz and Kosevich [22, 19] allows for the derivation of various damping effects such as finite temperature, finite relaxation time and electron spin.

Starting with the thermodynamic grand potential Ω,

$$\Omega = E - TS - \mu N, \tag{2.24}$$

where E is the internal energy, T is the temperature, S is the entropy, μ is the chemical potential and N is the number of electrons in the system. It is more convenient to choose Ω over the free energy $F = E - TS$ when certain quantities such as magnetic moment are to be calculated which is further elaborated in Shoenberg [19].

In general, for a system that obeys Fermi-Dirac statistics and has energy states ε, the grand potential can be written as a sum over all possible energy states,

$$\Omega = -k_B T \sum \ln[1 + \exp((\mu - \varepsilon)/k_B T)], \tag{2.25}$$

In the limit that ε varies continuously, the summation can be replaced by an integral in $\boldsymbol{k}$-space (with the appropriate density of states factor). For a system with energy levels quantised into Landau tubes specified by equation 2.19, the grand potential becomes

$$\Omega = -k_B T \int_{-\infty}^{\infty} \rho \, \mathrm{d}k \sum_n \ln(1 + e^{(\mu - \varepsilon_n)/k_B T}), \tag{2.26}$$

where $\rho \, \mathrm{d}k = D = eBV \, dk/2\pi^2\hbar$ is the number of states between k and $k + \mathrm{d}k$ on a Landau tube, and ε_n is the allowed energy state for quantum number n, given by the solution of the implicit equation 2.19.

At $T = 0$, the contribution $\delta\Omega$ from a two-dimensional slab of $\boldsymbol{k}$-space simplifies to

$$\delta\Omega = D \sum_{n=0}^{N} (\varepsilon_n - \mu), \tag{2.27}$$

where the summation is taken over the values of n such that $\varepsilon_n < \mu$ and ε_N denotes the state of highest energy. The summation can be evaluated using the Euler-Maclaurin formula and the detailed algebra can be found in Shoenberg ([19] pp. 38–41). The oscillatory component of Ω, denoted with a tilde, has the form

$$\delta\widetilde{\Omega}_{2D} \sim \cos 2\pi \left(\frac{F}{B} - \gamma \right), \tag{2.28}$$

where F is the frequency of oscillation defined in equation 2.23.

For a real metal, contributions $\delta\Omega$ from the parallel two-dimensional slices must be added up by integrating over the component of k parallel to the direction of the magnetic

field (e.g. k_z direction). The details are found in Shoenberg ([19] pp. $53-55$) and the end result is quoted:

$$\tilde{\Omega}_{3D} \sim \frac{B^{5/2}}{\left(\frac{\partial^2}{\partial k_z^2} A_{\text{Fermi}}\right)^{1/2}} \sum_{p=1}^{\infty} \frac{1}{p^{5/2}} \cos\left[2\pi p\left(\frac{F}{B} - \gamma\right) \pm \frac{\pi}{4}\right], \tag{2.29}$$

where A_{Fermi} is the extremal area of the Fermi surface defined in equation 2.23 and p is the harmonic index.

With this result, an expression for the oscillations in the density of states (which are closely related to the oscillations in the resistivity in the Shubnikov-de Haas effect) can be derived.[2] Returning to equation 2.26, the equation can be rewritten as

$$\Omega(\mu, T) = -k_B T \int_{-\infty}^{\infty} \mathscr{D}(\varepsilon) \ln(1 + e^{(\mu-\varepsilon)/k_B T})\, \mathrm{d}\varepsilon, \tag{2.30}$$

where $\mathscr{D}(\varepsilon)$ is the density of states for an arbitrary energy ε and the integral is now taken over ε instead. At $T = 0$, this becomes

$$\Omega(\mu, 0) = \int_{-\infty}^{\mu} (\varepsilon - \mu)\mathscr{D}(\varepsilon)\, \mathrm{d}\varepsilon, \tag{2.31}$$

from which it follows after differentiating under the integral twice that $\mathscr{D}(\mu) = -\partial^2\Omega(\mu, 0)/\partial\mu^2$.

Thus, carrying out the differentiation on equation 2.29, the result for the oscillatory behaviour of $\tilde{\mathscr{D}}(\mu)$ is given by

$$\tilde{\mathscr{D}}(\mu) \sim \frac{B^{1/2}}{\left(\frac{\partial^2}{\partial k_z^2} A_{\text{Fermi}}\right)^{1/2}} \sum_{p=1}^{\infty} \frac{1}{p^{1/2}} \cos\left[2\pi p\left(\frac{F}{B} - \gamma\right) \pm \frac{\pi}{4}\right]. \tag{2.32}$$

Several observations can be noted from equation 2.32:

- Due to the factor $\frac{\partial^2 A_{\text{Fermi}}}{\partial k_z^2}$ in the denominator, the quantum oscillation amplitude is reduced for a Fermi surface that has a large curvature. On the other hand, for a quasi-two-dimensional cylindrical Fermi surface, the curvature factor is very small and the quantum oscillation amplitude is significantly enhanced.

- Comparing Ω_{2D} and Ω_{3D}, there is an additional phase shift of $\pm\frac{\pi}{4}$ brought about by the integration over k_z. This factor will play a role in the subsequent analysis of γ.

[2] It is noted that the oscillations in the magnetisation in the de Haas-van Alphen effect can also be derived via the relation $\tilde{M} = -(\partial\tilde{\Omega}/\partial B)_\mu$.

2.1.5 Phase Smearing

In order to complete the theory, we need to account for effects due to finite temperature, finite electron relaxation time due to scattering events, and also electron spin. These effects can be treated in the framework of phase smearing, whereby the real world experimental environment differs from the idealised condition, resulting in a superposition of oscillations, each with their own frequency F' distributed about an 'ideal' frequency F. This spread of frequencies, or equivalently phases, results in factors that cause a reduction in the amplitude of the periodic oscillations.

It is shown in [19] that the damping factors are proportional to the Fourier transforms of their respective phase distribution functions. The detailed derivations of the various damping factors can be found in Shoenberg (pp. 57–66) and we will simply quote the final results.

Spin-splitting factor

In a magnetic field, the degeneracy due to electron spin is lifted and the energy levels for the two spin states are split. This will lead to a phase difference between the oscillations coming from the spin-up and spin-down electrons and the resultant superposition of the oscillations will give rise to a reduction factor R_s

$$R_S = \cos\left(\frac{\pi p g m_b}{2m_e}\right), \tag{2.33}$$

where p is the harmonic index, $g \sim 2$ is the spin splitting factor , and m_b is the band mass of the electron.

Dingle reduction factor

When we consider that electrons have a finite relaxation time due to the presence of impurities in the sample, the Landau levels become broadened in accordance to the uncertainty principle, a phenomenon first shown by Dingle. The broadening is equivalent in effect to a spread of Fermi energies about its true value and consequently, this spread of Fermi energies results in a spread of frequencies, leading to the reduction in oscillation amplitude.

The broadening of the Landau levels is described by a Lorentzian function of the form $1/(1+z^2)$, which has a Fourier transform of the form $e^{-\lambda}$, where λ is the Fourier frequency domain variable. The full Dingle reduction factor is given by

$$R_D = \exp\left(-\frac{\frac{\hbar}{2e}\frac{C_F}{l}}{B}\right), \tag{2.34}$$

where C_F is the circumference of the orbit in $\boldsymbol{k}$-space and l is the mean free path. A high quality sample that has few impurities would have a long mean free path compared to the circumference of its orbits, and as a result, the reduction factor would be small (i.e. close to unity).

Thermal smearing factor

At finite temperature T, the quantum oscillations that correspond to a real metal with Fermi energy μ can be thought of as equivalent to the superposition of quantum oscillations from a hypothetical distribution of metals at $T = 0$, each with Fermi energy μ' spread about μ. This is because the Fermi-Dirac distribution is no longer a step function at finite temperatures, and there is a finite probability that states above or below μ can be occupied.

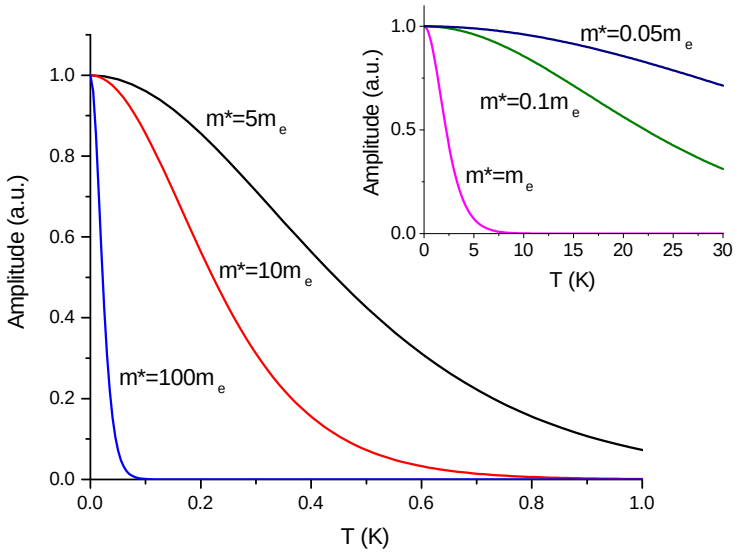

Figure 2.3: Simulation of the reduction of the quantum oscillation amplitude as a function of temperature. The simulations were carried out at a field of 15 T for various effective masses m^* – the heavier masses ($m^* > 1$) are plotted in the main diagram and the lighter masses ($m^* \leq 1$) in the inset.

The distribution of μ' is shown to be the negative derivative of the Fermi-Dirac function, which has the form $1/(1+\cosh z)$. The Fourier transform of such a distribution function has the form $\pi\lambda/\sinh(\pi\lambda)$. The full thermal damping factor is given by

$$R_T = \frac{X}{\sinh X}, \quad \text{where} \quad X = \frac{2\pi^2 p k_B T m^*}{e\hbar B} \simeq 14.7\,\frac{pTm^*}{B}. \tag{2.35}$$

Since X is proportional to m^*T, the thermal damping factor approaches unity as T approaches zero, highlighting the importance of a low temperature environment for ob-

serving quantum oscillations. This is especially evident for heavy quasi-particle effective mass m^* that arise from particle-particle interactions in strongly correlated systems, where the quantum oscillation amplitude is significantly attenuated before reaching 1 K (see Figure 2.3). Although damping effects due to finite temperatures hinder the observation and measurement of quantum oscillations, they serve as very useful tools for extracting the quasi-particle effective mass by use of equation 2.35.

Taking all these reduction factors into account, the full Lifshitz-Kosevich equation for the Shubnikov-de Haas oscillations in the conductivity $\tilde{\sigma}$ is

$$\tilde{\sigma} \sim \tilde{\mathscr{D}}(\mu) \sim \frac{B^{1/2}}{\left(\frac{\partial^2}{\partial k_z^2} A_{\text{Fermi}}\right)^{1/2}} \sum_p R_S R_D R_T \frac{1}{p^{1/2}} \cos\left[2\pi p\left(\frac{F}{B} - \gamma\right) \pm \frac{\pi}{4}\right]. \tag{2.36}$$

2.2 Carrier Concentration

The total number of electrons N in a system at a given temperature T is given by:

$$N = 2\sum_{\mathbf{k}} n_F\left(\beta(\epsilon_{\mathbf{k}} - \mu)\right) = 2\left(\frac{V}{(2\pi)^3}\right)\int n_F\left(\beta(\epsilon(\mathbf{k}) - \mu)\right)\, \mathrm{d}\mathbf{k} \tag{2.37}$$

where $n_F\left(\beta(\epsilon(\mathbf{k}) - \mu)\right) = \frac{1}{\exp((\epsilon(\mathbf{k})-\mu)/k_B T)+1}$ is the Fermi-Dirac distribution function and the sum over discrete energy states has been replaced by an integral in the continuum limit. In the low temperature limit where $T \to 0$, the Fermi-Dirac function becomes a step function and we can rewrite the equation as

$$n = \frac{N}{V} = \frac{2}{(2\pi)^3}\int \Theta\left(E_F - \epsilon(\mathbf{k})\right)\, \mathrm{d}\mathbf{k}, \tag{2.38}$$

where n is the number density, $\Theta\left(E_F - \epsilon(\mathbf{k})\right)$ is the Heaviside step function and $E_F = \mu|_{T=0}$ is the Fermi energy. By writing the integral in this way, we can see that the number density is proportional to a volume integral in $\boldsymbol{k}$-space that is bounded by the surface $\epsilon(k) \leq E_F$, i.e. the Fermi surface.

In particular, for a 3D free electron gas, the carrier concentration is

$$\begin{aligned} n &= \frac{2}{(2\pi)^3}\int \Theta\left(E_F - \epsilon(\mathbf{k})\right)\, \mathrm{d}\mathbf{k} \\ &= \frac{2}{(2\pi)^3}\int \Theta\left(E_F - \frac{\hbar^2\mathbf{k}^2}{2m_e}\right)\, \mathrm{d}\mathbf{k} \\ &= \frac{2}{(2\pi)^3}\left(\frac{4}{3}\pi k_F^3\right) \\ &= \frac{k_F^3}{3\pi^2}, \end{aligned} \tag{2.39}$$

a well-known result derived in condensed matter courses. For this special case, as the energy dispersion relation is isotropic in $\boldsymbol{k}$-space, the integral can be simply evaluated

as the volume of a Fermi sphere with radius $k_F = \left(\frac{2m_e E_F}{\hbar^2}\right)^{1/2}$.

In general, there may not be an analytic form for the volume enclosed by the Fermi surface and the integration has to be carried out numerically. The electronic properties and Fermi surface of the Rashba material BiTeI can be modelled by a Hamiltonian with a Rashba interaction term which will be discussed further in Chapter 4. A closed form solution for the carrier concentration described by such a Hamiltonian exists and is presented and compared against Hall effect measurements in that chapter.

2.3 Berry Phase

Returning to the phase factor γ that appears in the Onsager quantization rule 2.19, it is defined as

$$\gamma = \frac{1}{2} - \frac{\phi_B}{2\pi}, \tag{2.40}$$

where ϕ_B is the Berry phase. The Berry phase is defined to be the phase difference acquired when a classical or quantum mechanical system undergoes an adiabatic cyclic process. For our case in particular, it is the phase factor acquired due to the motion of electrons when they undergo cyclotron orbits and it depends on the shape of the energy band structure that the orbit encloses.

For a parabolic band dispersion $E = \hbar^2 k^2/2m^*$, the n^{th} Landau level has energy $E_n = \hbar\omega_c(n + 1/2)$ (equation 2.13). Each orbit in the $\boldsymbol{k}$-space plane perpendicular to the magnetic field is a circle with radius $k_n = \sqrt{2eB(n + 1/2)/\hbar}$. Thus the area of the n^{th} Landau level orbit in $\boldsymbol{k}$-space is given by

$$A_k = \pi k_n^2 = (n + \frac{1}{2})\frac{2\pi eB}{\hbar}. \tag{2.41}$$

A direct comparison of this equation with the Onsager equation 2.19 yields

$$\gamma = \frac{1}{2}, \tag{2.42}$$

i.e. the trivial case of $\phi_B = 0$.

In contrast, for a massless Dirac fermion that obeys a linear energy dispersion relation $E = \hbar\nu_F k$ (for example in graphene), the energy of the n^{th} Landau level can be shown to take the form $E_n = \text{sgn}(n)\sqrt{2e\hbar\nu_F^2|n|B}$. The radius of the n^{th} circular orbit is $k_n = \sqrt{2eB|n|/\hbar}$ and the $\boldsymbol{k}$-space area is given by

$$A_k = \pi k_n^2 = |n| \frac{2\pi eB}{\hbar}, \tag{2.43}$$

which gives the associated phase factor

$$\gamma = 0. \tag{2.44}$$

Thus we can see that for massless Dirac fermions that go through one cycle of orbit, they pick up a non-trivial Berry phase of $\phi_B = \pi$.

In the SdH effect, oscillations in the density of states give rise to periodic oscillations of the longitudinal conductivity $\Delta\sigma_{xx}$ as the external magnetic field is swept. From equation 2.32, the phase factor γ appears in the expression for the density of states which can be written in terms of longitudinal conductivity as

$$\Delta\sigma_{xx} \sim \tilde{\mathscr{D}} \sim \cos\left[2\pi\left(\frac{F}{B} - \gamma + \delta\right)\right], \tag{2.45}$$

where F is the frequency of the oscillations, $\delta = 0$ for 2D systems or $\delta = \pm 1/8$ for 3D systems (see equations 2.28 and 2.29).

2.3.1 Experimental Measurement of Berry Phase

From equation 2.45, the phase factor γ can be inferred from SdH experiments through a process called Landau level indexing. The maxima and minima of the observed quantum oscillations are given either integer or half-integer labels and plotted against inverse magnetic field, and the resultant intercept from the linear fit of the data gives the value of the phase. As the phase from the quantum oscillation study gives an indication as to the nature of the state – whether it is an 'ordinary' bulk state or the highly sought after topological surface state – the Landau level indexing method has been widely utilised in quantum oscillation work involving topological materials. For example, Landau level indexing was used to determine the value of the phase factor and hence the nature of the surface state for the class of 3D topological materials Bi_2Te_3, Bi_2Se_3 and their related compounds [23, 24, 25]. More recently, work done in [26, 27, 28] studied the phase factor of the SdH oscillations for the material BiTeI. A comprehensive review and discussion of applying this method to topological materials in general can be found in section 8.3 of [29] and also in [30].

There has been much confusion regarding the convention to adopt when it comes to assigning labels to the quantum oscillation maxima and minima – whether to assign an integer index to the minima in the resistivity ρ_{xx}, or to the minima in the conductivity

σ_{xx}. For example, in [31, 24, 25], minima of ρ_{xx} were indexed with integers while in [32, 33, 34], minima of σ_{xx} were used in the Landau level indexing. As the labelling conventions differ from each other by a phase of π, picking one over another would result in the phase γ being either 0 or 1/2, therefore it is important that the indexing process is carefully carried out. In Figure 2.4, the Landau level density of states is shown schematically as a function of energy. When effects due to scattering are ignored, the density of states appear as a series of perfect delta functions. However, these Landau levels are typically broadened due to thermal fluctuations or disorder in a real material.

When the chemical potential μ lies in between two neighbouring Landau levels, the density of states is a minimum – there are no empty states available at energies that are close to μ. In this situation, the material looks like an insulator as a certain number N of Landau levels are completely filled while the next Landau level is empty, and hence the electrical conductivity is at a minimum. Since we have completely filled Landau levels, we assign the integer number N to that conductivity minimum (Figure 2.4(c)).

Conversely, when μ lies at the centre of the Landau level (i.e. half-filled level), the density of states is a maximum. There are many available empty states near μ that can readily conduct electrical current. In this circumstance, the sample behaves like a metal which is reflected by a maximum in the conductivity, and we assign that maximum with a half-integer number (Figure 2.4(b)).

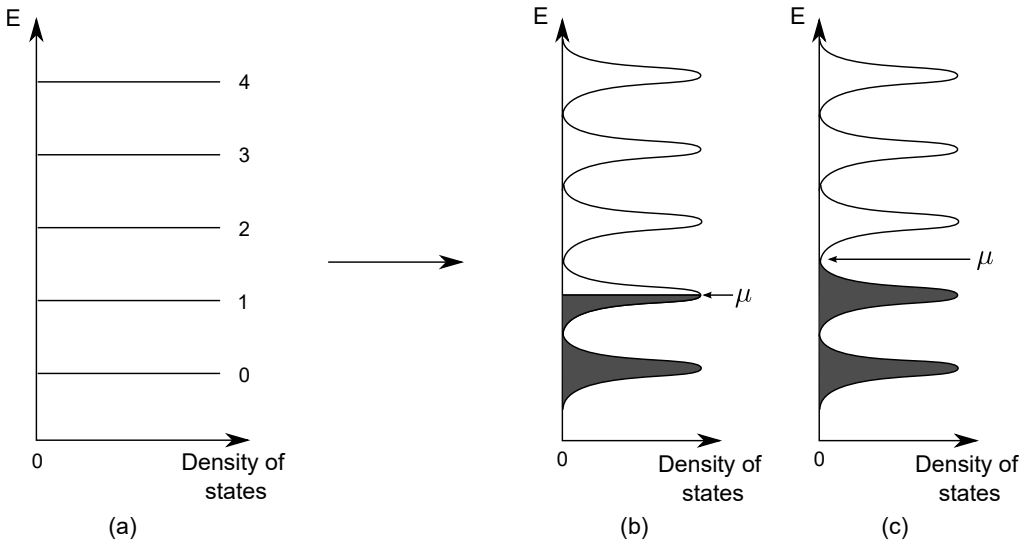

Figure 2.4: (a) Landau level density of states with zero scattering. In the presence of impurity scattering and thermal fluctuations, the levels are broadened in (b) and (c). When μ lies in the middle of the Landau level, the density of states is at a maximum; when μ lies in between two levels, the density of states takes a minimum.

According to equation 2.45, the n^{th} minimum occurs when the argument of the cosine function is an odd integer multiple of π, i.e. when

$$2\pi\left(\frac{F}{B}-\gamma+\delta\right)=(2n-1)\pi$$
$$\text{or} \qquad n=\frac{F}{B}-\gamma+\delta+\frac{1}{2}. \tag{2.46}$$

Thus, a plot of the Landau level index n against $1/B$ would yield a straight line, where the slope is the frequency of the quantum oscillation, and the n-axis intercept is $1/2-\gamma+\delta$.

However, experiments that involve the SdH effect measure the resistivity, rather than the conductivity of samples, and thus the resistivity data must be first converted into conductivity before performing the Landau level index analysis. The resistivity and conductivity tensors are related via

$$\begin{aligned}\begin{pmatrix} \sigma_{xx} & \sigma_{xy} \\ -\sigma_{xy} & \sigma_{xx} \end{pmatrix} &= \begin{pmatrix} \rho_{xx} & \rho_{xy} \\ \rho_{yx} & \rho_{xx} \end{pmatrix}^{-1} \\ &= \frac{1}{\rho_{xx}^2+\rho_{xy}^2}\begin{pmatrix} \rho_{xx} & -\rho_{xy} \\ \rho_{xy} & \rho_{xx} \end{pmatrix}.\end{aligned} \tag{2.47}$$

Thus we obtain the relationship between the longitudinal and transverse components of conductivity in terms of resistivity components ρ_{xx} and ρ_{xy}:

$$\begin{aligned}\sigma_{xx} &= \frac{\rho_{xx}}{\rho_{xx}^2+\rho_{xy}^2}, \\ \text{and} \qquad \sigma_{xy} &= \frac{-\rho_{xy}}{\rho_{xx}^2+\rho_{xy}^2}.\end{aligned} \tag{2.48}$$

The equation for σ_{xx} can be simplified when we consider the asymptotic limits (i) $\rho_{xx} \gg \rho_{xy}$ and (ii) $\rho_{xx} \ll \rho_{xy}$.

(i) When $\rho_{xx} \gg \rho_{xy}$,

$$\sigma_{xx} \simeq \frac{1}{\rho_{xx}}, \tag{2.49}$$

hence the minima of σ_{xx} coincides with the *maxima* of ρ_{xx}.

(ii) When $\rho_{xx} \ll \rho_{xy}$,

$$\sigma_{xx} \simeq \frac{\rho_{xx}}{\rho_{xy}^2}, \tag{2.50}$$

and the minima of σ_{xx} coincides with the *minima* of ρ_{xx}.

Depending on the relative magnitudes of ρ_{xx} and ρ_{xy}, different conclusions regarding σ_{xx} are drawn. Ideally, ρ_{xx} and ρ_{xy} should be simultaneously measured in order to construct σ_{xx}, so that the correct Berry phase can be obtained.

2.4 Hall Effect

The Hall effect refers to the transverse voltage measured when a magnetic field is applied perpendicular to an excitation current flowing along the sample. For an applied field $\boldsymbol{B}$ in the z-direction, and current density $\boldsymbol{J}$ in the x-direction, the Hall coefficient is defined as

$$R_H \equiv \frac{E_y}{J_x B}. \tag{2.51}$$

The force acting on a charge q with velocity $\boldsymbol{v}$ under the influence of both electric and magnetic fields is $\boldsymbol{F} = q\boldsymbol{E} + q\boldsymbol{v} \times \boldsymbol{B}$. Under the relaxation-time approximation, the steady state solution is given by

$$\begin{aligned} \frac{\boldsymbol{p}}{\tau} &= \boldsymbol{F} \\ m\frac{\boldsymbol{v}}{\tau} &= q\boldsymbol{E} + q\boldsymbol{v} \times \boldsymbol{B}, \end{aligned} \tag{2.52}$$

where $\boldsymbol{p}$ is the momentum, m is the mass, and τ^{-1} is the scattering rate of the charged particle. Evaluating the cross product gives two simultaneous equations for two unknowns v_x and v_y, which gives:

$$\begin{aligned} v_x &= \frac{q\tau}{m}\left(\frac{E_x + \frac{q\tau}{m}BE_y}{1 + \left(\frac{q\tau}{m}\right)^2 B^2}\right) \\ v_y &= \frac{q\tau}{m}\left(\frac{E_y - \frac{q\tau}{m}BE_x}{1 + \left(\frac{q\tau}{m}\right)^2 B^2}\right). \end{aligned} \tag{2.53}$$

Since current density can be written as $\boldsymbol{J} = nq\boldsymbol{v}$, where n is the carrier concentration, $\boldsymbol{J}$ can be written in terms of the electric field as:

$$\begin{aligned} \boldsymbol{J} &= \frac{nq^2\tau/m}{1 + (q\tau B/m)^2}\begin{pmatrix} E_x + q\tau BE_y/m \\ E_y - q\tau BE_x/m \end{pmatrix} \\ &= \frac{\sigma_0}{1+\gamma^2}\begin{pmatrix} 1 & \gamma \\ -\gamma & 1 \end{pmatrix}\begin{pmatrix} E_x \\ E_y \end{pmatrix}, \end{aligned} \tag{2.54}$$

where $\sigma_0 = nq^2\tau/m$, $\gamma = qB\tau/m$.

Since $\boldsymbol{J} = \underline{\underline{\sigma}}\boldsymbol{E}$, a direct comparison with equation 2.54 gives the expression for the conductivity tensor

$$\begin{aligned} \underline{\underline{\sigma}} &= \frac{\sigma_0}{1+\gamma^2}\underline{\underline{\gamma}}, \\ \underline{\underline{\gamma}} &= \begin{pmatrix} 1 & \gamma \\ -\gamma & 1 \end{pmatrix}. \end{aligned} \tag{2.55}$$

For materials that have more than one conduction band, with each band having different carrier mobilities and carrier concentrations, the ordinary Hall effect can show complex non-linear behaviour. Generalizing equation 2.55 for a system with N bands, the total conductivity is obtained by simply summing the contributions from each band, i.e.

$$\underline{\underline{\sigma}} = \sum_i^N \frac{\sigma_i}{1+\gamma_i^2}\underline{\underline{\gamma_i}}, \tag{2.56}$$

with $\sigma_i = n_i q_i^2 \tau_i / m_i$, $\gamma_i = q_i \tau_i B / m_i$.

As resistivity is measured during experiments, the more relevant quantity is the resistivity tensor $\underline{\underline{\rho}}$:

$$\begin{aligned}
\underline{\underline{\rho}} &= \underline{\underline{\sigma}}^{-1} \\
&= \frac{1}{\sigma_{xx}^2 + \sigma_{xy}^2} \begin{pmatrix} \sigma_{xx} & -\sigma_{xy} \\ \sigma_{xy} & \sigma_{xx} \end{pmatrix}, \\
\sigma_{xx} &= \sum_i^N \frac{\sigma_i}{1+\gamma_i^2}, \\
\sigma_{xy} &= \sum_i^N \frac{\sigma_i \gamma_i}{1+\gamma_i^2}.
\end{aligned} \tag{2.57}$$

For the case of $N = 1$, we find that the Hall resistivity ρ_{xy} is linear in B:

$$\rho_{xy} = \frac{\gamma}{\sigma} = \frac{1}{nq} B, \tag{2.58}$$

where we obtain the familiar result for the Hall coefficient $R_H = 1/nq$. The sign of the Hall coefficient would tell us the sign of the charge q and hence allow us to deduce the nature of the charge carriers responsible for electrical transport in the sample.

For $N = 2$, the full expression for ρ_{xy} takes the form

$$\begin{aligned}
\rho_{xy} &= \frac{\sigma_1\gamma_1 + \sigma_2\gamma_2 + \gamma_1\gamma_2(\sigma_1\gamma_2 + \sigma_2\gamma_1)}{(\sigma_1+\sigma_2)^2 + (\sigma_1\gamma_2 + \sigma_2\gamma_1)^2} \\
&= \frac{(q_1 n_1 \mu_1^2 + q_2 n_2 \mu_2^2)B + (\mu_1\mu_2)^2(q_1 n_1 + q_2 n_2)B^3}{(q_1 n_1 \mu_1 + q_2 n_2 \mu_2)^2 + (\mu_1\mu_2)^2(q_1 n_1 + q_2 n_2)^2 B^2},
\end{aligned} \tag{2.59}$$

where $\mu = q\tau/m$ is the carrier mobility. If one of the carrier charges has an opposite sign to the other, as in the case of electrons and holes in semiconductors, the equation reduces to the familiar form that is often used for modelling transport behaviour in semiconductors.[3]

For the two-band model, we see that the Hall resistivity is no longer linear in B as

[3]The expression for Hall resistivity in the presence of electrons and holes is $\rho_{xy} = \frac{(n_e\mu_e^2 - n_h\mu_h^2)B + (\mu_e^2\mu_h^2)(n_e - n_h)B^3}{e((n_e\mu_e + n_h\mu_h)^2 + \mu_e^2\mu_h^2(n_e - n_h)^2B^2)}$.

opposed to the case for the single band, and the behaviour of the function depends on the relative magnitudes of the parameters n_1, n_2, μ_1, μ_2. Different combinations of the parameters are explored and presented in Appendix C. We will use this model for fitting our Bi_2Te_3 Hall effect data in Chapter 5.

Chapter 3

Experimental Methods

3.1 Physical Property Measurement System (PPMS)

One of the helium-4 cryostats used for our measurements is the Physical Property Measurement System (PPMS), designed and sold by Quantum Design. The helium-4 option on the PPMS can cool to a temperature of 2 K by pumping on the helium gas above the liquid helium in a small volume surrounding the sample chamber, reducing the boiling point of the liquid helium. A more comprehensive description detailing the functionality of a helium-4 cryostat can be found in standard textbooks ([35] is an excellent resource). Our PPMS is equipped with a 9 T magnet and has a helium-3 option for cooling down to temperatures of 0.3 K by condensing and pumping on liquid ^{3}He.

The PPMS probe as illustrated in Figure 3.1 is immersed in a dewar of liquid helium. The superconducting magnet is positioned such that the field centre is above the sample platform, and the experiment is mounted as close to the field centre as possible, where the field is homogenous. The impedance assembly allows the PPMS fine control of the cooling power of the cryostat, where it draws liquid helium and fills the cooling annulus. Depending on the desired temperature, the liquid helium either vaporises or fills the annulus up, allowing for an even cooling or heating of the sample chamber.

For our pressure cell measurements, the pressure cells are physically screwed onto a PPMS puck, and the wires from the cells are then soldered onto the soldering pads on the puck. The puck has 12 connectors, so in theory it is possible to mount three samples on the puck and measure them using the 4-wire measurement technique. In order to measure four or more samples, samples can be wired together such that the excitation current flows through all of them in series, and the voltage drop across each of the samples are measured individually using a home-made multiplexer box.

3.2 Kelvinox Dilution Refrigerator with 18 T Magnet

In order to reach millikelvin temperatures, a dilution refrigerator by Oxford Instruments was used. The main mechanism that allows the dilution refrigerator to achieve

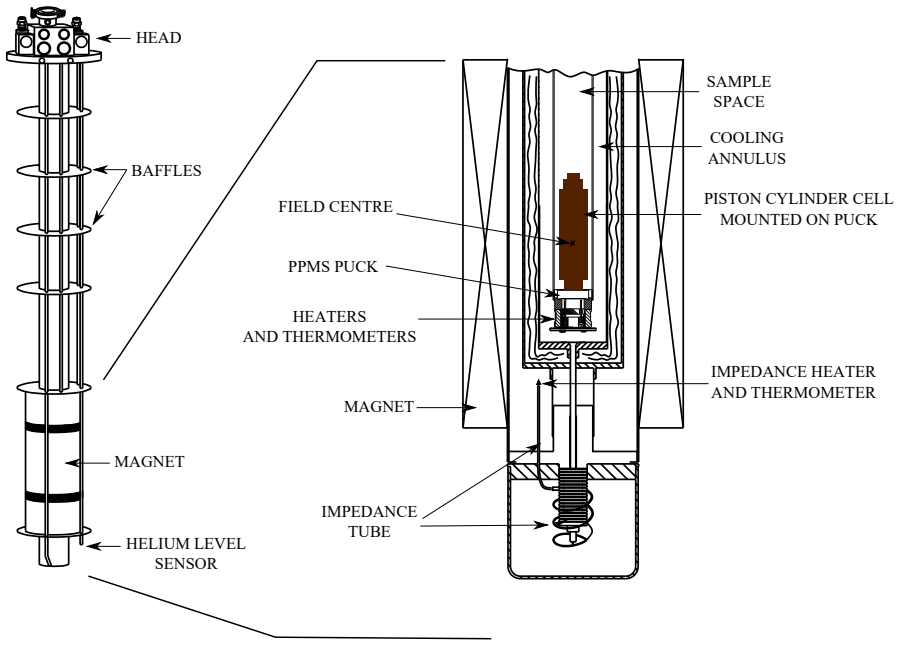

Figure 3.1: The figure on the left shows the PPMS insert with the superconducting magnet. The figure on the right shows an enlarged cross sectional view of the experimental stage with the cooling elements, thermometry and a piston-cylinder cell connected up to the PPMS via the PPMS puck [36].

millikelvin temperatures is through the mixing of helium-3 and helium-4 isotopes. When a mixture of the two helium isotopes is cooled below a critical temperature, it separates into two phases; a concentrated phase rich in ^{3}He and a dilute phase that is rich in ^{4}He (Figure 3.2). As the enthalpies of ^{3}He in the two phases are different, cooling can be achieved when ^{3}He from the concentrated phase is evaporated into the dilute phase. The crucial point is that the ^{3}He equilibrium concentration is always finite even at the lowest temperatures, thus this process will continue to occur, allowing the fridge to reach temperatures of about 10 mK. In order to achieve a continuously operating fridge, ^{3}He that has evaporated into the dilute phase must be extracted and returned into the concentrated phase to maintain dynamic equilibrium, and a schematic of that process is shown in Figure 3.2.

A pump connected to the still pumps ^{3}He gas away from the liquid surface in the still, which is maintained at around 0.7 K so that ^{3}He evaporates preferentially over ^{4}He. Osmotic pressure then drives a flow of liquid ^{3}He from the mixing chamber into the still, and the ^{3}He leaving the mixing chamber is used to cool the returning flow of ^{3}He through a series of heat exchangers. The gas (mostly ^{3}He) leaving the still is circulated back into the system through the condenser line, completing the circuit. Just

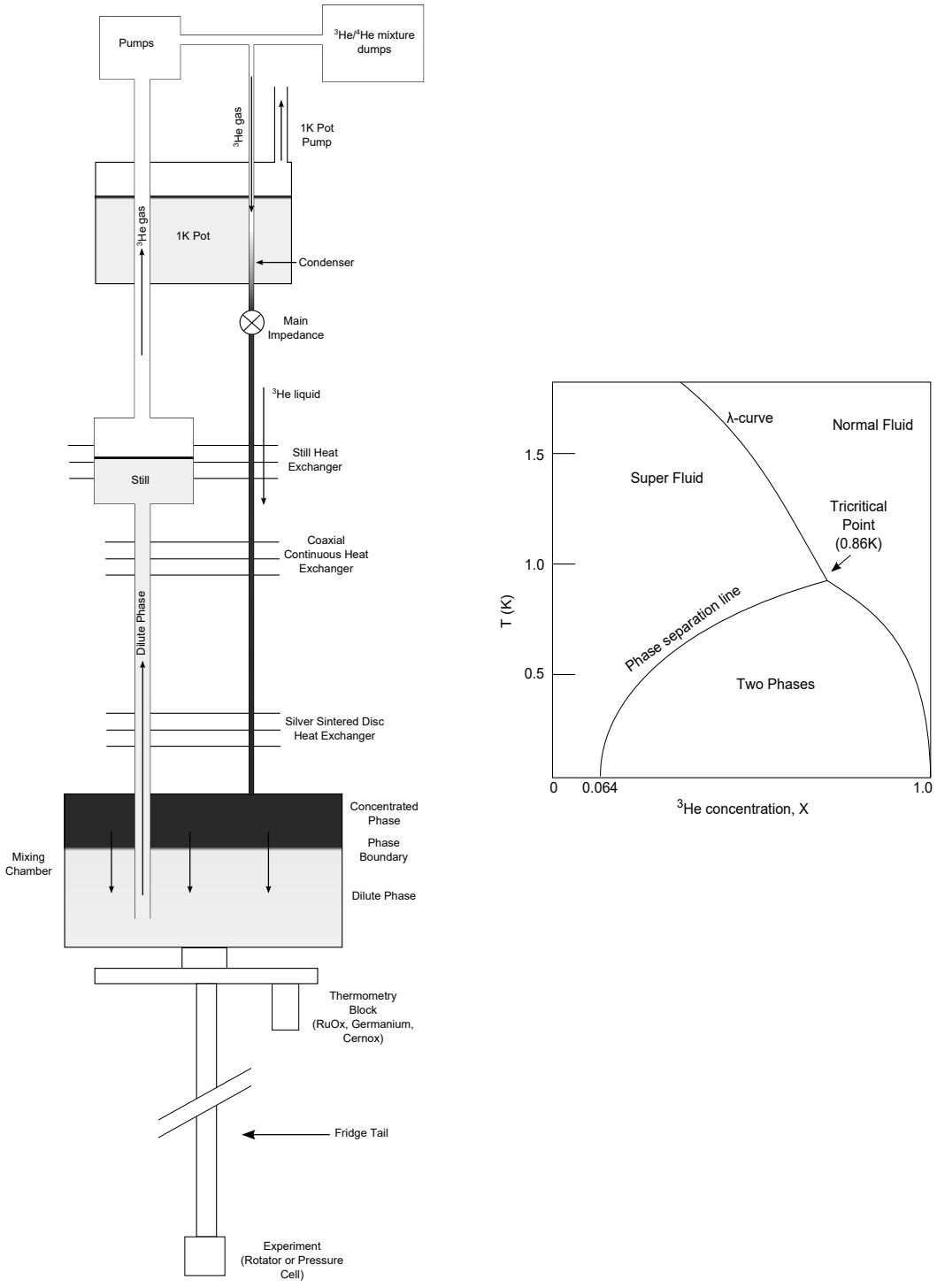

Figure 3.2: The figure on the left is a schematic of our dilution refrigerator, showing how ^{3}He is circulated in the system. The figure on the right is the phase diagram of ^{3}He/^{4}He mixtures. $X = n3/(n3 + n4)$ is the ^{3}He concentration, where $n3$ ($n4$) is the number of ^{3}He (^{4}He) atoms.

before entering the condenser line, this gas is passed through a series of cold traps in order to freeze out any impurities that might otherwise cause blockages and crash the fridge. It is then precooled by the main helium bath and then by the 1K pot, where a

flow impedance ensures a high pressure region for the gas to condense. A comprehensive discussion of how the dilution fridge works can be found in [35] and [37].

The fridge tail is mounted and thermally anchored to the bottom of the mixing chamber, and depending on the experimental setup, either a rotation mechanism or a pressure cell can be mounted at the end of the tail. The cryostat is then inserted into the magnet, which is capable of reaching 16 T at 4.2 K, and up to 18 T when it is cooled to around 2.2 K using the lambda point refrigerator. A set of bellows on top of the magnet dewar allows the cryostat to be lowered such that the experiment is in the field centre. The temperature of the mixing chamber is monitored by several thermometers, namely a ruthenium oxide chip, germanium sensor and a Cernox sensor. They are calibrated to measure temperatures below 1 K, from 1 to 1.2 K, and above 1.2 K respectively. At the time of writing, the magnet has been upgraded to reach 18 T at 4.2 K and 20 T using the lambda fridge.

3.3 15T Variable Temperature Insert System

The bulk of the experiments probing the quantum oscillations of BiTeI under pressure were carried out using our 15T system by Oxford Instruments. It has a Variable Temperature Insert (VTI) that hangs vertically down inside the magnet bore, and it shares a common vacuum space with the main cryostat. The samples are mounted on a probe which is lowered into the VTI space. Depending on the type of experiment, a different probe can be used and this system allows for great flexibility in running various measurements. In this regard, it is quite similar to the PPMS, where the user changes PPMS pucks or uses the PPMS ^{3}He-probe to suit the particular experimental run.

In terms of its operation, this system is also very similar to the PPMS. Liquid helium is drawn from the helium reservoir in the magnet dewar, and the flow is controlled using a needle valve adjusted at the top of the cryostat. Together with a suitable temperature controller (we are using the Oxford Instruments ITC4 with our system), the cooling power of the flowing helium can be balanced by electrical heater power, allowing the temperature of the insert to be varied from 1.5 K to 300 K.

There are essentially two modes of operation for the VTI system - temperatures below 4 K and temperatures from 4 to 300 K. For temperatures below 4 K, the needle valve is opened wide enough so that the VTI space will start to fill with liquid helium. Once filled, the vapour pressure above the helium liquid in the VTI space can be monitored and pumped down to the required pressure (and hence temperature) by using a manostat. A little fine tuning with the pumping valves is required to get the manostat to maintain the vapour pressure of the helium bath but once it is set, the manostat can hold the

temperature of the helium bath very reliably at 2 K, with a very slight drift of about 0.06 mK/min.[1] For temperatures above 4 K, the needle valve is just cracked open with the VTI heater turned on, such that the helium liquid is turned into gas as it enters the space. The required temperature is obtained by adjusting the power supplied to the heater.

The superconducting magnet comprises of concentric solenoid sections, each primarily wound using niobium titanium (NbTi) wire. In addition, the magnets responsible for the high fields are fitted with inner coil sections of niobium tin (Nb_3Sn) [38]. The magnet is equipped with a heat switch, allowing for persistent-mode operation. The heat switch consists of a segment of superconducting wire that is wound together with an electrical heater, and is wired parallel to the magnet. The heat switch can be opened (made resistive) or closed (superconducting) by heating the switch, allowing the magnet to be charged/discharged or be in the persistent mode state respectively. This magnet is capable of reaching fields of 13 T under normal operations, and up to 15 T when the magnet is further cooled to 2.2 K using the lambda point refrigerator. Rather than pumping on the entire helium bath to reduce its boiling point, the lambda fridge cools the helium around the magnet through conduction and convection. It draws and pumps on helium from the main bath into a cooling coil using a needle valve and the cold gas in the coil cools the surrounding helium by conduction. The cooler and denser helium sinks to the bottom of the cryostat, while the warmer helium at 4.2 K rises to take its place, creating a convection cooling cycle.

3.3.1 ICE Oxford Helium-3 Probe

For the first few measurements of the pressure cell, the ^{3}He-probe by ICE Oxford was used. The probe can reach temperatures of about 0.3 K by pumping on liquid ^{3}He and making use of the latent heat of vapourization of ^{3}He as the main cooling mechanism. It is interesting that just by using a different isotope of helium, we are able to access temperatures below 1 K even though the physical process of cooling through evaporation is the same in both ^{4}He and ^{3}He cryostats. Although they have the same electronic structure (completely filled s-shells) and behave in an identical way chemically, their different behaviours are made pronounced at low temperatures due to quantum mechanical effects, namely, the different spin-statistics they have to obey and their different zero-point energies.

As ^{3}He atoms have a smaller atomic mass m compared to ^{4}He atoms, they experience a larger quantum mechanical zero-point energy E_{ZPE}.[2] The larger zero-point energy

[1] This was estimated by comparing the starting temperature before the start of a field sweep with the final temperature after the field has been swept back to zero.

[2] $E_{ZPE} = h^2/8ma^2$ where $a = (V_m/N_A)^{1/3}$ is the radius of the sphere in which the atoms are

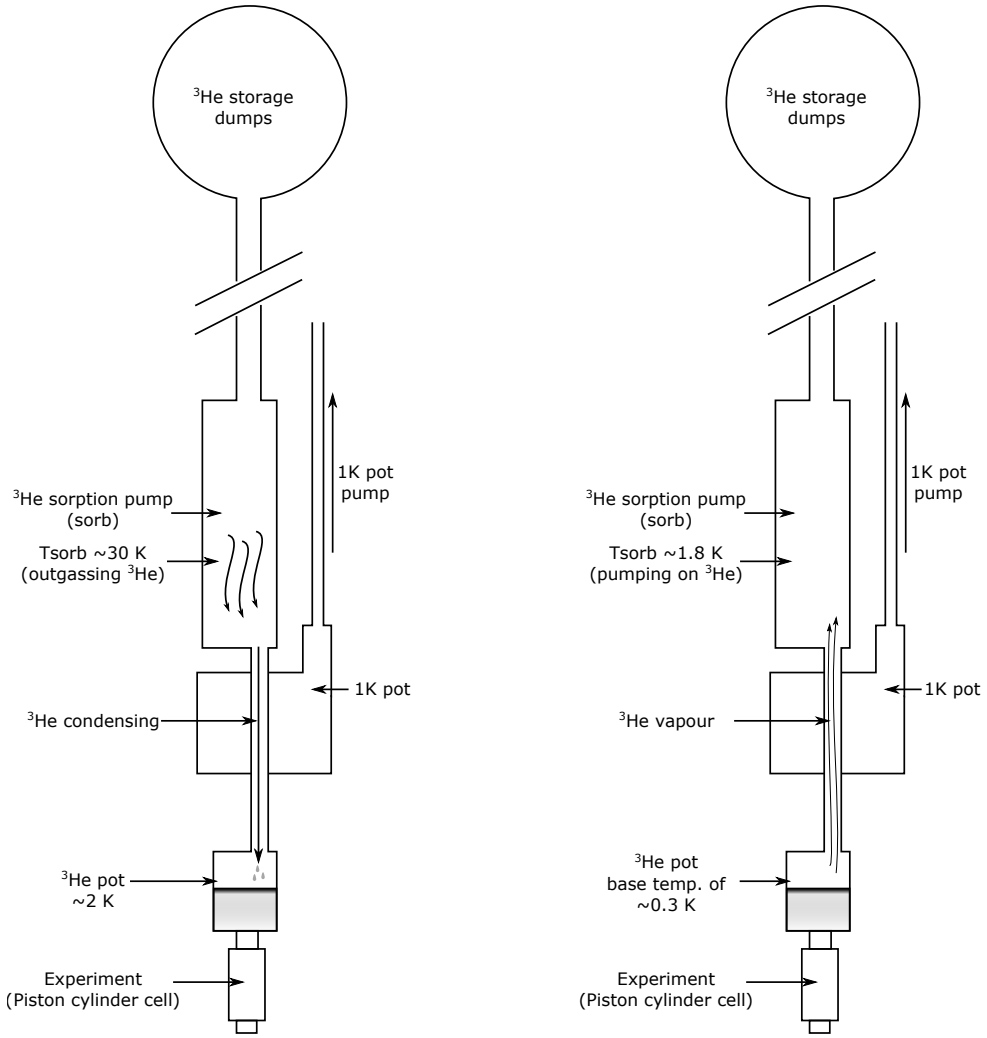

Figure 3.3: Schematic of the ^{3}He-probe with an internal adsorption pump. The figure on the left shows the ^{3}He being outgassed by the warm sorb, cooled and then condensed into the ^{3}He pot. Once all the ^{3}He has been condensed into liquid, the sorb is cooled and it starts pumping on the ^{3}He vapour, lowering the boiling point of the liquid, as shown by the figure on the right.

of ^{3}He gives rise to its lower boiling point and larger vapour pressure compared to ^{4}He. The total spin of ^{3}He atom is 1/2, as such it is a fermion and has to obey Fermi-Dirac statistics and the Pauli principle. In contrast, the ^{4}He nucleus has a spin of 0, and it can undergo a Bose-Einstein like condensation to form a superfluid at 2.17 K.

The main components of the ^{3}He-probe are outlined in the schematic in Figure 3.3. It consists of a hermetically sealed region containing the ^{3}He gas and charcoal that acts as the sorption pump. The probe has a 1K pot that is used to cool and condense the ^{3}He gas. This probe is designed to be used in a helium transport dewar, but it can also be used with the 15T VTI system. The typical operation of the probe is to first get it to cool down to around 4 K using liquid helium from the dewar, get the 1K pot cold, and

confined to and $N_A = 6.02 \times 10^{23}$ atoms mol^{-1} is Avogadro's number.

start to condense the ^{3}He. This is done by warming the charcoal sorb to around 30 K which causes the ^{3}He atoms to desorb, get cooled down by the 1K pot and condense into the ^{3}He pot. When all of the ^{3}He has been condensed, the 'one-shot' operation of the fridge can commence by allowing the sorb to cool. As it starts to cool, ^{3}He atoms will start to adsorb onto the charcoal, which is effectively pumping on the ^{3}He bath, thereby lowering the boiling point and reducing the temperature of the bath. Our probe is capable of reaching a base temperature of 0.3 K with an average hold time of around 4 hours. There are screw threads which allow different types of experimental stages or pressure cells to be attached directly below the ^{3}He pot, ensuring good thermalisation even at the base temperatures.

3.3.2 Helium-4 Probe

Due to other ongoing projects that require the use of the ^{3}He-probe, it was decided that an old ^{4}He-probe would be recommissioned and wired up to run quantum oscillation measurements under pressure. As the effective masses for the sample to be measured are quite light, temperatures less than 1 K are not necessary and the use of a ^{4}He-probe would suffice. This was made possible with Prof. John Cooper's old ^{4}He-probe, together with his help and advice on matters pertaining to wiring and machining parts for the probe.

The existing wires and sample platform were removed, and a new stage was designed and machined out of brass to minimise eddy current heating when the field is ramped. In order to minimise thermal conduction from the room temperature measurement connectors down to the probe, thin copper wires (90 μm) were used to make the new twisted wire pairs. The thermometry wires were kept separate from the measurement wires, which in turn were also separated into the 'current' pairs and the crucial 'voltage' or 'sensing' pairs. This is done to reduce any noise pickup that might otherwise interfere with the actual signal from the samples. The twisted wire pairs were then sheathed in Teflon tubes to protect them and soldered onto the probe connectors at the top. The other ends were soldered onto a circuit board further down the probe. Wires coming up from the experiment side were wound around copper posts and stuck down with generous amounts of GE-7031 Varnish to heat sink them, before being soldered onto the other end of the circuit board. The probe heater was made by winding roughly 50 Ω of Constantan wire around the stem of the brass platform, and anchored in place with GE Varnish. The use of removable heat sinking posts, thermometer bobbins and the circuit board was to make the various parts modular and easily changeable, and to make the wiring clear and well-documented. A schematic representation as well as pictures of various pieces of the probe are shown in Figure 3.4.

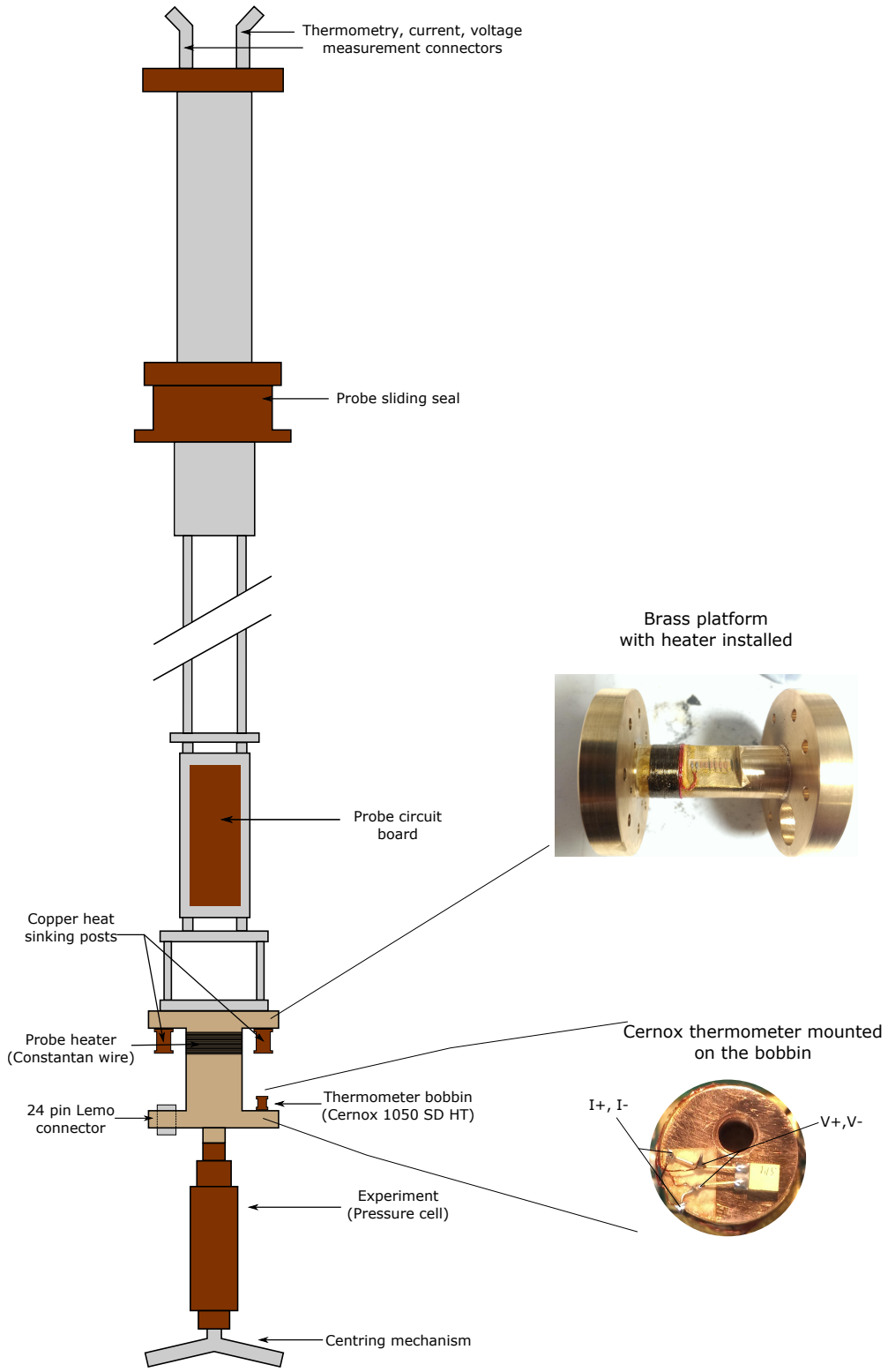

Figure 3.4: Left: Schematic of the ^{4}He-probe. Top right: Brass piece with Constantan heater installed. Bottom right: Top view of the thermometer bobbin with the Cernox chip attached.

The thermometer used is an uncalibrated Cernox 1050-SD-HT chip purchased from Elliot Scientific. It was calibrated from 300 K down to 0.8 K using our PPMS ^{3}He option.

The book by Ekin [39] was a very helpful resource as it contains useful information regarding machining parts for the probe, and aspects of probe-wiring such as heat sinking and soldering.

3.4 Powder X-ray Diffraction

Powder X-ray diffraction is a method commonly used to determine the structure of crystalline samples and also to detect the presence of any impurity phases in the main compound. Small pieces (about 10-20 mg) of BiTeI samples from three different growth batches, namely BiTeI grown in 5 percent and 10 percent excess iodine, and BiTeI grown using the chemical vapour transport (CVT) method, were powderised using a pestle and mortar. The powder was then smeared onto glass slides and loaded into the X-ray diffractometer with the help of Hajime Shinohara and Jiasheng Chen, both PhD students from the group.

These powder X-ray studies were carried out after the quantum oscillation measurements under pressure were completed because the measurements of the CVT samples were markedly different from that of BiTeI from other growth batches and we needed to verify that we were measuring BiTeI.

The X-ray diffraction data was collected between 10° and 60° with a step size of 0.05°. A quick 10 minute scan was sufficient to detect the positions of the Bragg peaks for all three samples in order to compare the peaks against published powder X-ray results carried out on BiTeI.

Using the open-source software package Profex to carry out X-ray data analysis, the diffraction data for BiTeI +5% and +10% excess iodine samples are plotted in Figures 3.5 and 3.6 respectively. The (hexagonal) lattice parameters obtained for the +5% sample are: $a = 4.34$ Å and $c = 6.86$ Å; $a = 4.35$ Å and $c = 6.86$ Å for the +10% sample, in agreement with previous reports of $a = 4.3392(1)$ Å and $c = 6.854(1)$ Å in [40].

The X-ray diffraction data for the sample grown using the chemical vapour transport method is plotted in Figure 3.7. Contrary to expectations, it was found that the sample is actually Bi_2Te_3 , as can be seen by comparing the diffraction peaks obtained from the measurements to that of Bi_2Te_3 . Refinement of the data yields values for the lattice parameters $a = 4.39$ Å and $c = 30.51$ Å , consistent with the reported values of $a = 4.38471(7)$ Å and $c = 30.4984(11)$ Å by [41].

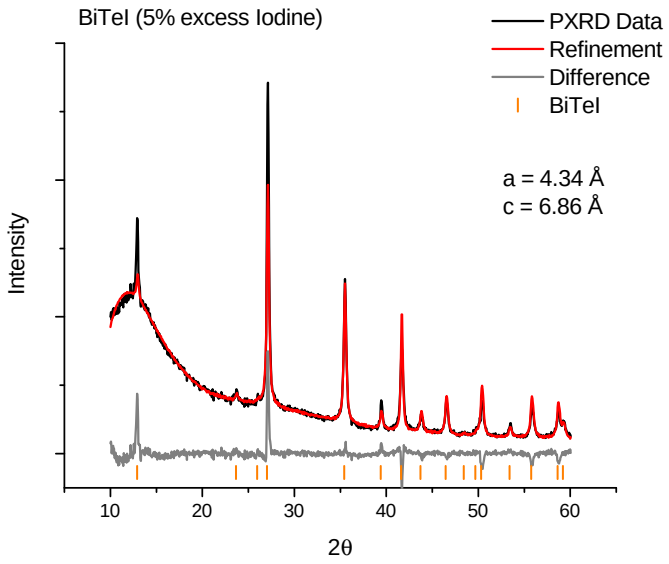

Figure 3.5: Powder X-ray diffraction of BiTeI +5% excess iodine.

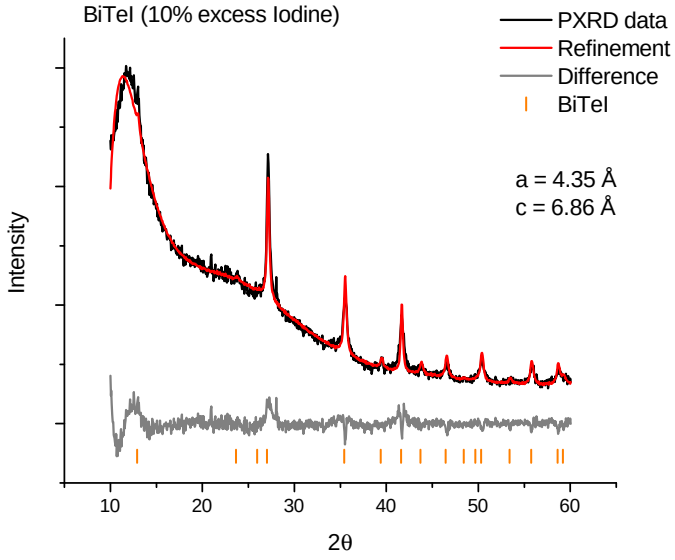

Figure 3.6: Powder X-ray diffraction of BiTeI +10% excess iodine.

3.5 Sample Preparation for Transport Measurements

Before the start of a successful measurement run, the initial stage of selecting and preparing samples is a crucial step. Smaller samples need to be cleaved from the parent crystal, and potential samples selected from the fragments of the cleaving process. For this work, thin and flat samples with smooth mirror-like surfaces were prioritised. Thin

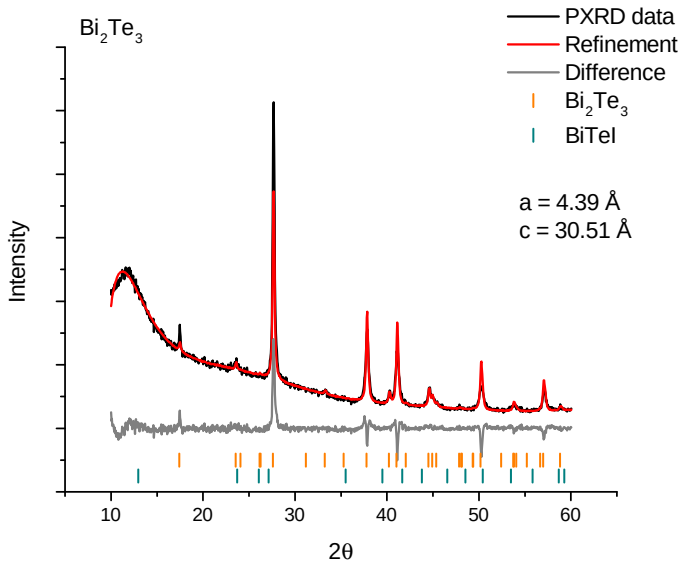

Figure 3.7: Powder X-ray diffraction of the sample grown by chemical vapour transport method, which turned out to be Bi_2Te_3 . Diffraction peaks for BiTeI are also plotted for comparison.

and long samples would give a larger geometric factor, and hence give rise to a larger voltage drop across it when measured by a lock-in amplifier. As BiTeI is a layered compound with weak van der Waals forces between the layers, it is fairly easy to cleave this material perpendicular to the crystallographic c-axis. In fact, we are able to use the 'scotch-tape method' to produce very thin pieces of BiTeI, in a manner similar to how graphene was first made [42].

For our material, a piece that was roughly flat and rectangular was first fixed onto a glass slide using double-sided tape. Another glass slide with double-sided tape was used to repeatedly peel layers of material off until a piece that is less than 10 μm thick was obtained (Figure 3.8). In order to avoid bending or warping the sample, the force used to separate the two slides has to be applied as evenly as possible across the surface area of the sticky tape. Retrieval of the thin flake of sample is a little tricky, as it is very easy to bend the material when trying to dislodge it from the tape. Soaking the entire glass slide in acetone for 5 to 10 minutes to dissolve the adhesive on the tape, followed by gentle prodding with the soft bristles of a fine paintbrush produced good results.

Depending on whether a resistivity or Hall measurement is to be carried out, either a long bar-shaped sample or a square-like sample can be cut from the flake using a sharp scalpel (Figure 3.9). Electrical contacts were then placed on the samples using a capacitive-discharge spot welder [43]. 25 μm gold wires are typically used for making contacts to bigger samples while 12.5 μm gold wires are used for the smallest of samples that go into anvil cells. The spot welder consists of a power supply that passes a short

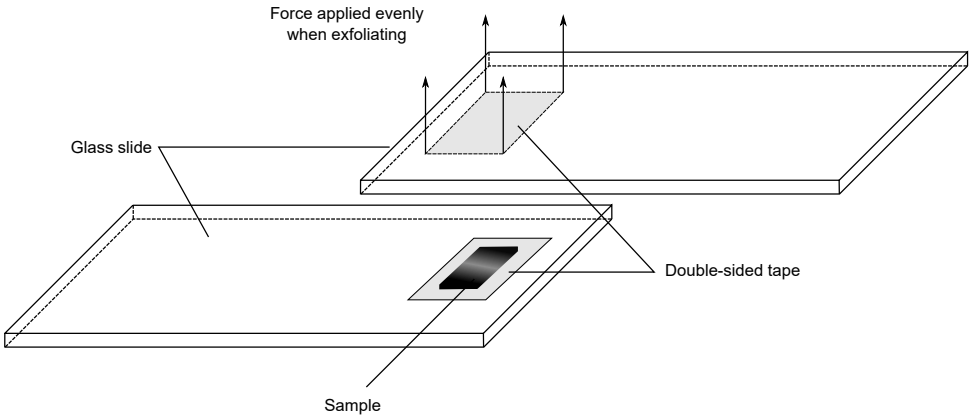

Figure 3.8: Obtaining thin pieces of BiTeI via exfoliation.

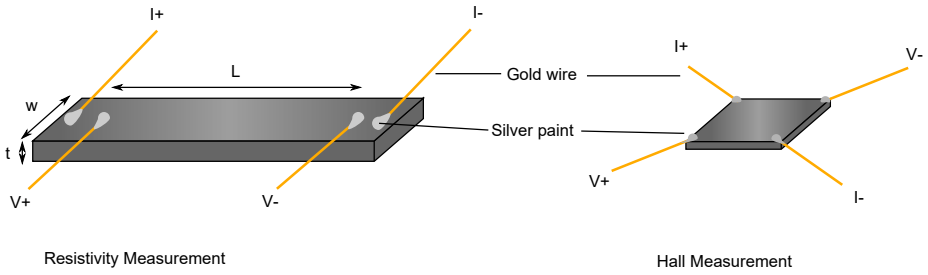

Figure 3.9: Samples contacted for a 4-wire electrical transport measurement.

pulse of current down a tungsten tip, through the gold wire and sample, melting the two materials together locally. The tungsten tip can be made very sharp through careful polishing with silicon carbide paper, making it possible to spot weld contacts onto tiny samples for pressure cell measurements. Besides making contacts at precise locations of the sample, the spot welded contacts are also generally of very high quality, giving very low contact resistances (less than 0.1 Ω at room temperature) to the sample.

After spot welding, the contacts can be further mechanically reinforced with silver conductive paste to make them more robust. For samples that can tolerate heat treatment, oven-cured Dupont 6838 paste (cured at 180°C for 1.5 hours) provides a strong bond, while the slightly weaker Dupont 4929N paste that sets in room temperature can be used for heat sensitive samples. For BiTeI, the electrical resistivity characteristics and also quantum oscillation frequencies measured in the PPMS show no appreciable difference between contacts fixed with 4929N and oven-cured 6838 silver paste, thus the stronger 6838 paste was favoured over 4929N to prepare sample contacts for subsequent measurements.

3.6 High Pressure Methods

In order to achieve the high pressures required to tune materials towards a phase transition for studying quantum critical phenomena, our group employs two main types of pressure cells: the piston-cylinder cell and the moissanite (or diamond) anvil cell.

3.6.1 Piston Cylinder Cell

For moderate pressures up to 30 kbar, the piston-cylinder cell is used. It is fairly reliable in reaching these pressures under hydrostatic conditions. A schematic of the pressure cell used in this work is shown in Figure 3.10 (left). The pressure cell is comprised of a beryllium copper outer body, with a tapered inner jacket made from an alloy called MP35N. The alloy has high tensile strength, is non-magnetic and consists mainly of cobalt and nickel, with small amounts of chromium and molybdenum. The alloy is heat treated to harden it even more, before being pushed into the outer cell body using a hydraulic ram. A narrow bore with diameter of 4 mm inside the MP35N jacket serves as the high pressure sample space region.

Pressure is applied using a hydraulic ram via a tungsten carbide piston. It is transmitted through the pressure pad that has a larger surface area to another piston to ensure that the force is applied evenly. This piston presses against beryllium copper anti-extrusion discs which in turn press against a Teflon cap filled with pressure transmitting fluid. The discs are there to ensure that the Teflon cap seals properly when pressure is applied and that the pressure medium does not escape. The force applied from the ramp is held in place by a beryllium copper lock-nut. Daphne oil 7373 was used as the pressure fluid, able to provide hydrostatic conditions for pressures below 2.2 GPa. Work done by Yokogawa *et al.* [44] showed that Daphne oil 7373 solidifies at room temperature at the pressure of 2.2 GPa. Thus for pressures above 2.2 GPa, a heat gun was used to gently warm the pressure cell with the hope of melting the pressure fluid prior to pressurization. At the other end of the Teflon cap lies the sample stage and wire feedthrough, which is held in place by another beryllium copper lock-nut and an end cap, and is often also used to mount the pressure cell onto the cryostat probe.

The most important part of the pressure cell can be said to be the wire feedthrough. It allows the wires that are responsible for measuring the properties of the samples to pass from the high pressure region to ambient pressure. The feedthrough is also the part of the pressure cell that is most susceptible to failure, and great care must be taken when preparing them to ensure the best chance of taking the cell up to the highest pressures. When preparing a new wire feedthrough, the bore of the feedthrough is checked to ensure that it is clear and free from any debris from previous pressure cell runs. Any

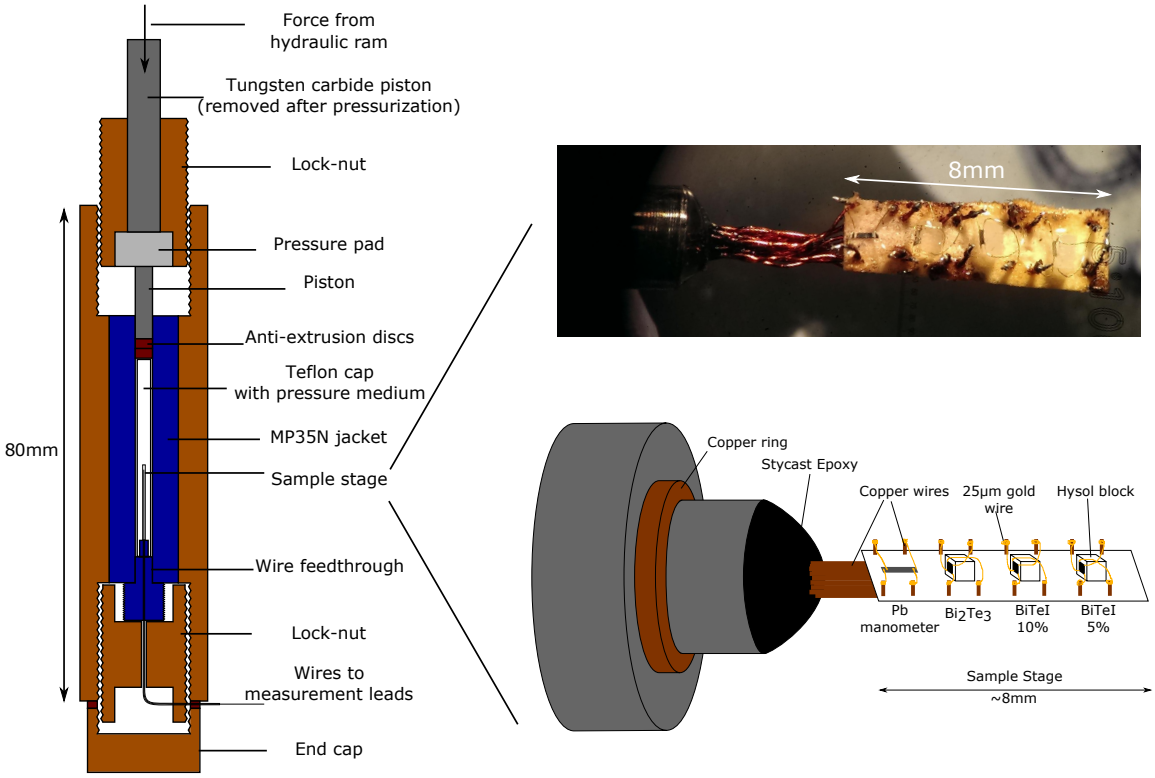

Figure 3.10: Left: Sketch of the piston-cylinder cell and its various components. Right: Picture (top) and drawing (bottom) of the wire feedthrough and the sample stage. The drawing shows four samples connected up on the sample stage, a lead manometer to measure the pressure inside the cell, and three samples of BiTeI grown under different conditions.

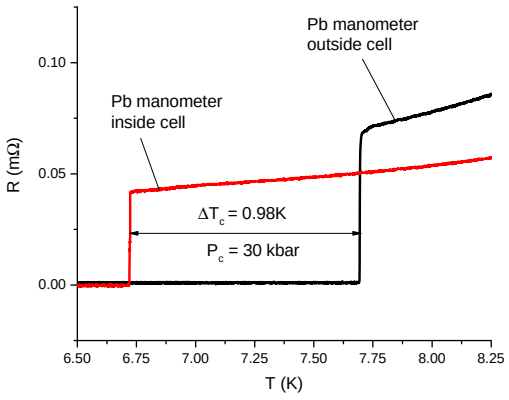

Figure 3.11: Using the superconducting transition of lead to determine the pressure inside the pressure cell. The black (red) curve corresponds to lead outside (inside) the cell.

old epoxy left in the bore is carefully drilled out and the feedthrough is cleaned with acetone in an ultrasonic bath. A two-part Stycast 2850 epoxy is used to seal the bore and it is crucial that the epoxy is thoroughly degassed in a vacuum chamber (such as a dessicator jar) after mixing to remove any trapped air. If there are any bubbles of air left in the epoxy after it has sealed the bore, the wires and epoxy can blow out as soon as the cell is pressurised, potentially crushing all the samples and ending a pressure cell run.

There are various techniques used to assemble the feedthrough, for example one that uses a vacuum set up to suck epoxy down the bore [45]. Even though our technique is less elaborate, the success rate is still fairly high. We fill the bore with epoxy by first threading the twisted pairs of wire through the feedthrough, and then simply applying the degassed epoxy onto the wires close to the mouth of the bore and gently pulling the wires through the bore, dragging the epoxy together with them. This action is repeated on both ends of the bore until the epoxy has completely filled the bore of the feedthrough. It is useful to keep the epoxy warm (either with a heat gun or in close proximity to a table lamp) to lower its viscosity and make it flow better. Since this entire procedure is based on visual inspection and there is a high degree of variability, extra feedthroughs are prepared in one sitting so that there is a high chance of having at least one working feedthrough. Any excess epoxy left on the wires must be carefully cleaned off using cotton buds dipped in acetone, otherwise the wires might become brittle and break when the epoxy hardens. The feedthrough is then left in an oven at 65 °C for 2.5 hours for the epoxy to cure.

Before mounting samples on the feedthrough, each feedthrough was individually tested by assembling the pressure cell, and applying pressure of up to 160 bar using the hydraulic ram. If the feedthrough survived, the cell can be taken apart and the sample stage can be prepared.

For the sample stage, a strip with dimensions of about 8×2 mm was cut from a stiff piece of card. Holes for the wires were made by piercing the stage using a needle and the copper wires were threaded through them (see Figure 3.10 (right)).

In order to align the samples such that the c-axis of the material points parallel to the direction of the applied magnetic field, they were supported by blocks made from a rigid plastic material called Hysol. Only the gold wires, not the samples themselves, were physically glued to the blocks using GE varnish. This was to ensure that the samples were surrounded by pressure medium and that they were under hydrostatic conditions. The gold wires were then wound around the copper wire posts and soldered onto them. Three samples from different growth conditions were mounted on the stage.

A thin piece of high purity lead was used as a manometer, and the pressure inside

the cell was determined by measuring the shift of the superconducting temperature (T_c) of lead. Under ambient pressure, lead becomes superconducting at 7.19 K and T_c shifts with pressure given by an empirically determined relation $T_c = 7.19 - 0.038P$, where pressure P is measured in kbar [46]. Another piece of lead was contacted in the same way and placed on the outside of the pressure cell. By comparing the relative shifts in their superconducting transitions, any systematic errors (such as that introduced by thermal gradients in the experiment stage, resulting in the pressure cell being at a different temperature to the thermometer) can be minimised and a more accurate reading of the pressure inside the cell can be obtained. Figure 3.11 shows the superconducting transition of two pieces of lead, one inside the pressure cell and one mounted on the outside, measured simultaneously in the 15T cryostat. In this particular plot, the shift in T_c corresponds to a pressure of 30 kbar inside the cell.

This work was done together with the help from Philip Brown and Konstantin Semeniuk, both PhD students in the Quantum Matter group. Their experience with setting up piston-cylinder cells has been invaluable in diagnosing problems when the cell failed.

3.6.2 Moissanite Anvil Cell

For experiments that require much greater pressures, diamond or moissanite anvil cells are used. Anvil cells achieve hydrostatic pressure conditions through the compression of a small volume of pressure fluid medium held within the walls of a metallic gasket. The gasket is made of beryllium copper or stainless steel and a hole is drilled into the gasket to serve as the space containing the sample and pressure medium. There are two anvils in each cell, each made of a very hard material such as diamond or moissanite. The business end used to generate the high pressures is the smooth, flat surface of the anvil also known as the culet. As force is applied, the gasket that is held between the two culets gets compressed and starts to flow, reducing the volume of the sample chamber, resulting in an increase in pressure within the fluid. The anvils are held in place by pistons, with one anvil fixed relative to the other. The piston assembly comes with alignment screws, allowing the anvils to be aligned such that they are centred and their surfaces are parallel to each other. A very thorough and in-depth discussion has been given by Dunstan and Spain on this matter, from the theory of the gasket [47], to operational procedures [48], to cell design and build considerations [49]. A schematic of the anvil cell is shown in Figure 3.12.

The pressure inside an anvil cell is determined by measuring the fluorescence spectra of a piece of ruby placed alongside the sample in the sample space. When the chromium impurities in ruby are excited to higher energy states by laser light, they will relax back to the ground state after transitioning through a metastable state, emitting photons in

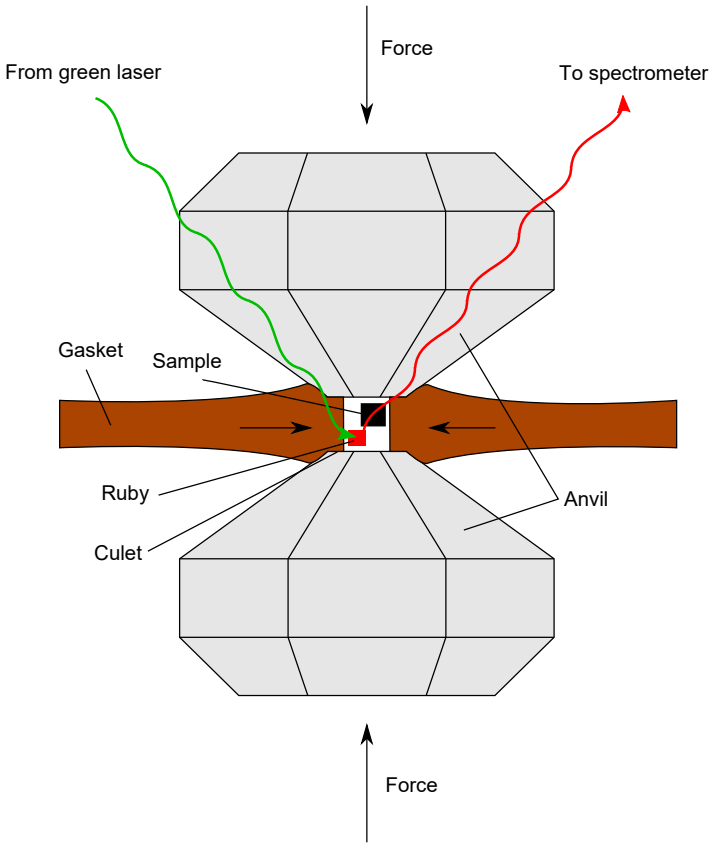

Figure 3.12: Operating principle of an anvil cell.

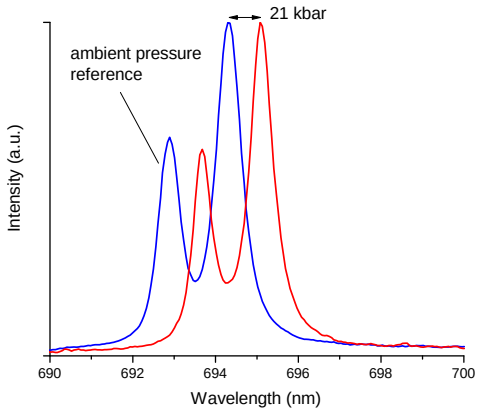

Figure 3.13: Ruby fluorescence spectra showing the shift in peak positions as pressure is increased.

the process. A green laser is used in our lab to excite the ruby in our anvil cells and the ruby spectra shows two characteristic peaks at specific wavelengths. These peaks are dependent on pressure, and they shift to higher wavelengths as the pressure increases [50]. Figure 3.13 shows a typical ruby fluorescence spectra taken from one of the pressure

runs.

Depending on the size of the culet used, the anvil cell can reach pressures of up to 140 kbar once it is properly set up. Even higher pressures in the megabar range have been recently attained by other groups using anvils with extremely small culet dimensions, e.g. the work involving metallization of H_2S at about 0.9 Mbar with a superconducting transition at 203 K [51]. The drawback of anvil cells is the severe difficulty in setting a cell up as compared to a piston-cylinder cell due to the tiny space available for the samples. I am very grateful for the help of Dr Patricia Alireza in setting up a moissanite anvil cell for high pressure measurements of BiTeI.

Chapter 4

BiTeI

4.1 Introduction

BiTeI has a trigonal crystal structure, belonging to the space group $P3m1$. The compound is composed of layers of Bi, Te, and I atoms. Within each layer, the atoms are arranged in a triangular network and stacked along the c-axis, as shown in Figure 4.1a. The structure of BiTeI can be explained using the semi-ionic model [40], where the Bi and Te atoms couple together to form positively charged $(BiTe)^+$ layers while the I^- anions form negatively charged layers. This results in the material having an intrinsic polar axis oriented along the c axis. Although each triple layer is held together strongly by this semi-ionic bond, adjacent triple layers are weakly bonded together by van der Waals forces, which allowed for the preparation of thin sample flakes using exfoliation.

The Rashba-Bychkov effect was originally used to describe the motion of confined electrons in a 2D electron gas under the influence of an electric field normal to the

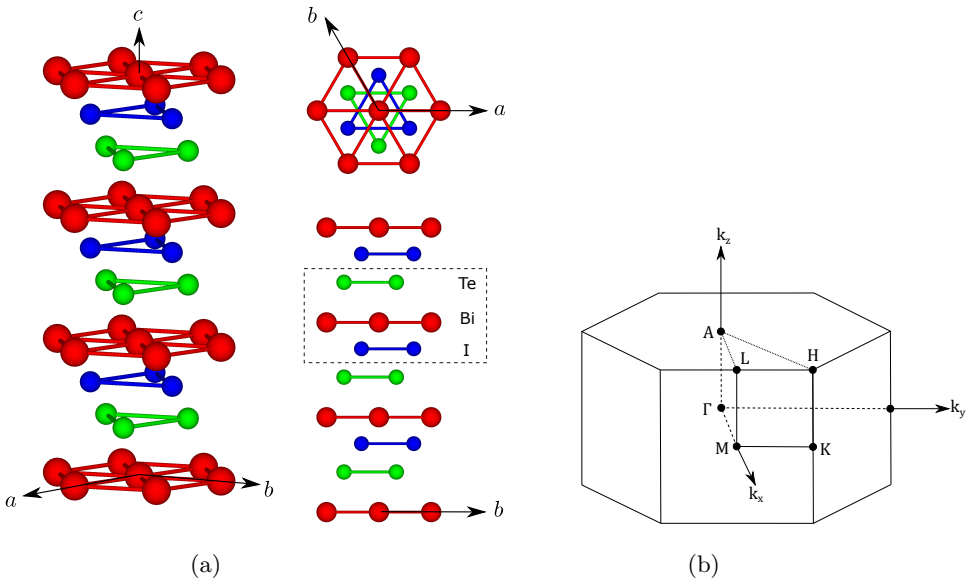

(a) (b)

Figure 4.1: (a) Crystal structure of BiTeI generated using VESTA. (b) Hexagonal Brillouin zone.

plane of the electron gas [52]. With respect to the rest frame of the electron, this electric field is an effective magnetic field, which couples to the electron spin. As a result of this interaction term, the once spin-degenerate parabolic bands are split into dispersions with oppositely spin-polarised states. Ishizaka *et al.* [53] performed angle resolved photoemission spectroscopy (ARPES) measurements in order to probe the band dispersion of BiTeI and showed that such a spin-splitting due to the Rashba effect indeed occurs in BiTeI. From the experiments, the binding energy for the conduction band minimum was determined to be $E_{CBM} = 0.29$ eV, located at $k_{CBM} = 0.052$ Å^{-1}, and the energy gap was estimated to be ~ 0.38 eV. The strength of the Rashba interaction is characterised by the amount of spin splitting of the bands, which is measured by E_R – the energy difference between the Dirac point located at the band crossing and the conduction band minimum (see Figure 4.2). Measurements indicate that this material has an E_R of about 100 meV, which is one of the largest among Rashba systems (typically of the order of several meV). Another consequence of the Rashba coupling is that the momentum and spin of the electron are constrained to be perpendicular to each other, resulting in a non-trivial Berry phase in the cyclotron orbit [26]. Moreover, the polarised spins circulate in opposite directions between the upper and lower bands when the chemical potential lies above the Dirac point. Such a spin texture of the conduction band was observed via spin-resolved ARPES (SRAPRES) carried out by Ishizaka *et al.* [53].

Due to self-doping effects from iodine deficiencies [54], BiTeI is considered a degenerate semiconductor with metallic behaviour. This enabled quantum oscillation studies

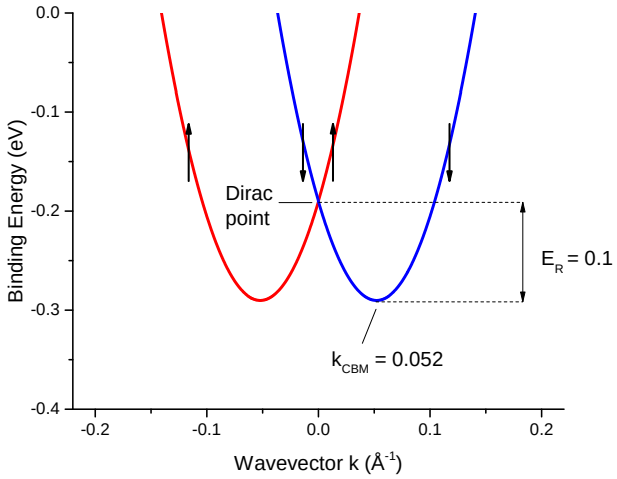

Figure 4.2: Rashba split conduction band dispersion, based on results obtained from ARPES measurements [53].

that probe the Fermi surface to be carried out on this material. Shubnikov-de Haas (SdH) measurements conducted by Bell *et al.* [55] showed the existence of two Fermi surface sheets having oscillation frequencies of ~ 360 T and ~ 4 T. The angular dependence of the oscillation frequencies was consistent with theoretical density functional theory (DFT) calculations of the Fermi surface structure. Martin *et al.* [56] reported only one SdH frequency ~ 280 T, and from their optical reflectance measurements, showed that this is likely due to bulk carriers. They concluded that the chemical potential for their sample sits just above the Dirac point, such that only one frequency was observed. Park *et al.* [57] performed both SdH and de Haas-van Alphen (dHvA) angular studies on BiTeI and established that the bulk Fermi surface has a spindle-torus topology. By analysing the phase of the quantum oscillations, they concluded that both surfaces exhibit non-trivial Berry phase, each with polarised spins circulating in opposite directions from one another.

These experiments demonstrate that BiTeI is indeed a system hosting a large Rashba interaction, which makes BiTeI a potentially interesting candidate material for spintronic devices [58], as well as studying unconventional superconductivity in non-centrosymmetric materials [59]. Interest in this material was further piqued when Bahramy *et al.* [18] predicted that the crystal-field splitting and spin-orbit interaction in BiTeI can be tuned by the application of hydrostatic pressure such that above a critical pressure, the conduction and valence bands undergo band inversion, turning the material into a topological insulator (TI). Unlike conventional TIs where this gap closure and band inversion occurs at a single high symmetry k-point (e.g. the Γ point for Bi_2Te_3 and Bi_2Se_3), the gap closure for BiTeI occur at six k-points along the $A-H$ directions, resulting in a different topological order compared to Bi_2Te_3 or Bi_2Se_3.[1] From their calculations, it is predicted that the critical pressure occurs in the range of 1.7–4.1 GPa.

Several optical experiments have been carried out to validate this theoretical prediction, with mixed conclusions regarding the presence or absence of a topological phase transition in BiTeI. Tran *et al.* [60] measured the optical reflectivity and transmission of BiTeI up to a pressure of 15 GPa and they found clear evidence for a structural transition at 9 GPa. They concluded that since this structural transition occurs before the predicted topological phase transition, it precludes the observation of such a topological transition. Xi *et al.* [61] used powder x-ray diffraction and infrared spectroscopy techniques to study BiTeI under pressure. From their powder x-ray diffraction measurements, they too reported that BiTeI undergoes a structural transition at 8 GPa. However, from the analysis of the lattice parameters c/a as well as optical conductivity

[1] Due to T-symmetry, the six k-points are two-by-two paired with each other ($\boldsymbol{k}$,$\uparrow$ paired with $-\boldsymbol{k}$,$\downarrow$ states), thus the TI state is described by three pairs of 2×2 Dirac fermions compared to the single 2×2 Dirac fermion for Bi_2Te_3 or Bi_2Se_3.

data, they found signatures that point to a pressure-induced topological quantum phase transition occurring at around 2.2–2.9 GPa.

Besides optical measurements, transport measurements under pressure have also been carried out. VanGennep *et al.* [62] performed SdH experiments to track the Fermi surface of BiTeI up to a pressure of 2 GPa. Up to those pressures, they did not observe any signs of the predicted topological transition. More recently, Park *et al.* [27] carried out SdH measurements of BiTeI up to a pressure of 3.35 GPa. Based on the unusual increase in the SdH oscillation frequency for the inner Fermi surface and an abrupt phase shift in the outer Fermi surface, they concluded that these observations are the consequence of a change in Fermi surface shape caused by the topological quantum phase transition.

Motivated by the theoretical predictions of BiTeI, researchers have also started investigating BiTeCl, a cousin compound belonging to the class of Rashba semiconductors BiTeX (X = Cl, Br, I). Compared to BiTeI, the chlorine atom is smaller than the iodine atom, resulting in a smaller unit cell volume in BiTeCl, thus BiTeCl can be thought of as the high pressure analogue of BiTeI. However, just like BiTeI, results regarding the presence of a Dirac surface state have not been conclusive. ARPES measurements performed by Y. Chen *et al.* [63] demonstrated the presence of a surface Dirac cone in the bulk energy gap, providing strong evidence for the topological insulating phase in BiTeCl. Results from SdH transport measurements performed by another group F. Chen *et al.* [64] showed otherwise. Angular dependence of the oscillation frequencies as well as Hall measurements on samples of BiTeCl with varying carrier concentrations point to a 3D Fermi surface from a bulk state rather than a 2D surface state.

In view of these uncertainties, we aimed to carry out our own set of transport and quantum oscillation measurements of BiTeI under pressure to clarify the issue.

4.2 BiTeI Zero Percent Excess Iodine

The very first measurements of BiTeI were carried out on the first batch of single crystals provided by Prof. Geetha Balakrishnan from the University of Warwick. These single crystals were grown using the Bridgman method, with stoichiometric amounts of elemental bismuth, tellurium and iodine used in the growth process. Flakes of BiTeI with dimensions of $2 \times 0.8 \times 0.1$ mm^3 had gold wires spot welded onto them in order to carry out 4-wire transport measurements. Preliminary resistivity measurements on the PPMS (Figures 4.3 and 4.4a) indicated a metallic conductivity while a field scan up to 9 T shows a low frequency quantum oscillation in the resistivity, suggesting that the single crystals are of high quality with a long mean free path ideal for doing quantum

oscillation studies.

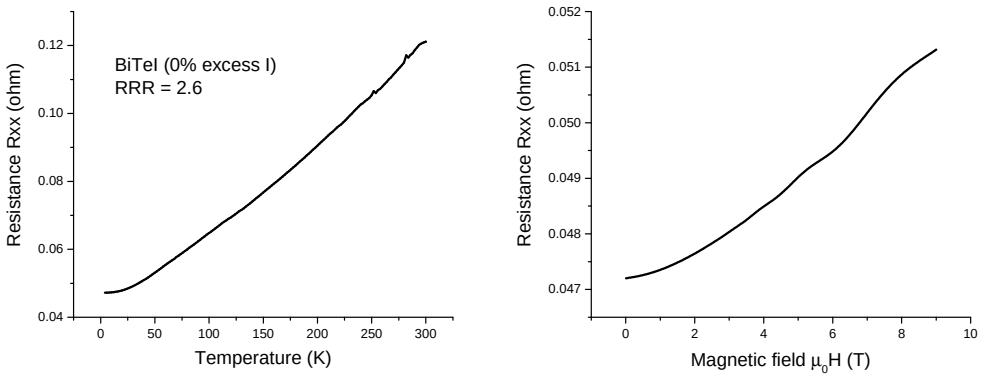

(a) (b)

Figure 4.3: (a) Resistance measurement of BiTeI that shows a metallic conductivity with a $RRR = R_{300K}/R_{2K} = 2.6$. (b) Field scan from 0–9 T. A low frequency oscillation in the resistance is apparent at fields above 5 T.

4.2.1 Piston Cylinder Cell Measurements

After the samples were shown to exhibit quantum oscillations from the preliminary measurements, smaller samples with estimated dimensions of $1 \times 0.4 \times 0.05$ mm^3 were cut and contacted in a similar manner for resistivity quantum oscillation measurements. The material was mounted on the side of a Hysol block which was then stuck down onto the sample stage using GE varnish so as to align the material's c-axis parallel to the magnetic field (similar to how samples were mounted in Figure 3.10). The sample stage was then loaded into a 18 mm diameter piston cylinder cell, using a 4:1 mixture of methanol-ethanol as the pressure medium.

The pressure in the piston cylinder cell was determined by measuring the shift in the superconducting temperature of a piece of lead manometer that was also mounted within the cell using the PPMS. The cell was then transferred to the dilution fridge in order to measure the samples to fields up to 16 T. The plots in Figure 4.4b are obtained by taking a derivative of the raw signal, followed by a second order polynomial background subtraction. Two frequencies can be clearly observed – a low-frequency oscillation corresponding to the smaller inner Fermi surface (IFS), and a higher-frequency oscillation corresponding to the larger outer Fermi surface (OFS) that can be observed at fields above 11 T.

Figure 4.5 plots the fast Fourier transform (FFT) spectrum of the data using two different field ranges. The FFT peaks corresponding to the IFS are plotted in the main figure while the OFS peaks are plotted in the inset. It can be seen that with increasing

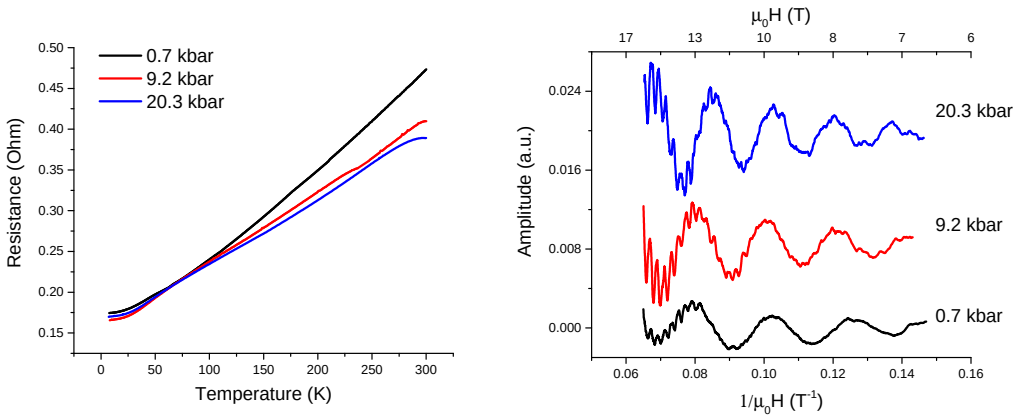

(a) (b)

Figure 4.4: (a) PPMS measurements of resistance as a function of temperature at different pressures. (b) Measurements from 7–16 T carried out in the dilution fridge. Plots are of the derivative of the signal against inverse field, with offset for clarity.

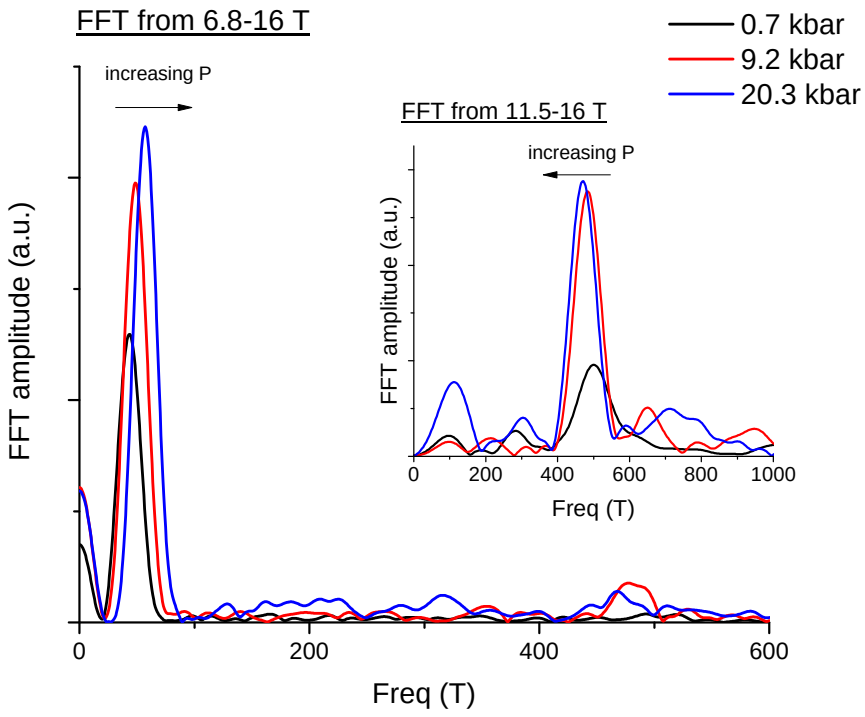

Figure 4.5: FFT spectrum of the quantum oscillation data taken across two different field ranges to capture the frequencies corresponding to the inner and outer Fermi surface (inset). The peaks for the inner Fermi surface shift towards higher frequencies while the peaks for the outer Fermi surface shift towards lower frequencies with increasing pressure.

pressure, the IFS peaks shift to higher frequencies, while the OFS peaks shift to lower frequencies.

The actual frequency of the oscillation can be determined by fitting the data to the Lifshitz-Kosevich (LK) formula 2.36. In order to help with convergence of the fits, the frequencies can be cleaned up by applying a band-pass filter on the data. The band-pass filter works by multiplying a suitably chosen top-hat function with the FFT spectrum of the data, such that frequencies that lie outside of the top-hat are excluded. Figures 4.7a and 4.8a plot the filtered data for the IFS and OFS sheets respectively, together with the frequency values obtained from the LK fit. The uncertainty associated with the quantum oscillation frequency is obtained by first using a Gaussian to fit the Fourier spectrum peak, and taking the width (one standard deviation) of the Gaussian fit as the measurement uncertainty (shown in Figure 4.6). A MATLAB program was written to assist in the analysis of the quantum oscillation data, and more details can be found in Appendix A.

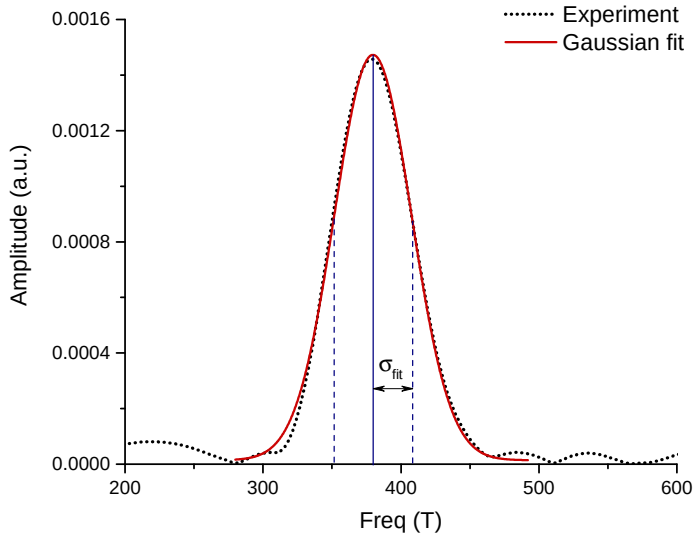

Figure 4.6: The uncertainty in the measurement of the quantum oscillation frequency is estimated from the standard deviation (σ_{fit}) of the Gaussian fit to the FFT spectrum peak.

As temperature was varied from 100 mK to about 30 K, the quantum oscillation amplitude was determined for each frequency. The temperature dependence of the quantum oscillation amplitude is plotted in Figures 4.7b and 4.8b for the respective Fermi surface sheets, together with the fits to the LK temperature factor R_T. The masses extracted from the fits are very light, as evidenced by the fact that the oscillations could still be observed at 30 K. The frequency and effective mass results are summarised in Table 4.1.

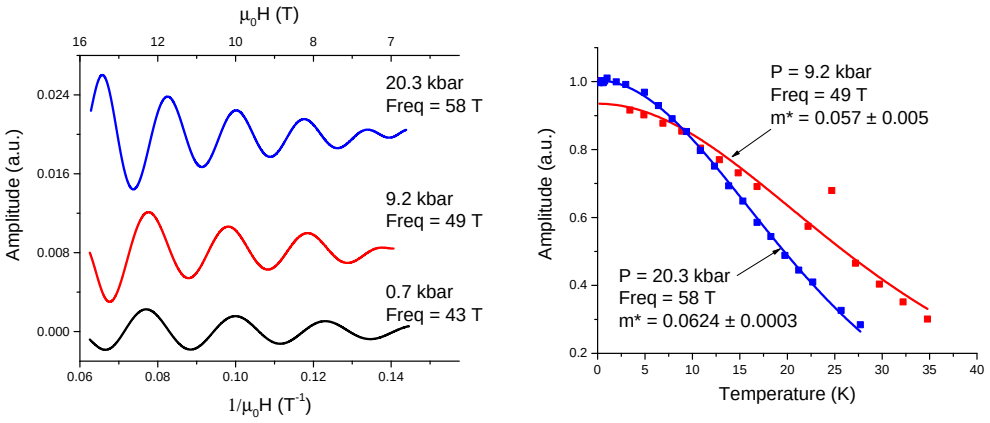

(a) (b)

Figure 4.7: (a) Quantum oscillation data corresponding to the inner Fermi surface after applying a band-pass filter. (b) Mass study plots for the 9 kbar and 20 kbar runs.

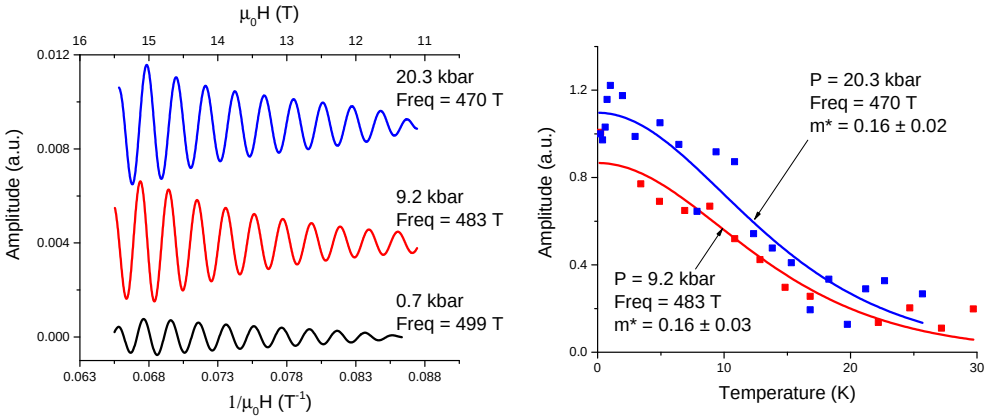

(a) (b)

Figure 4.8: (a) Quantum oscillation data corresponding to the outer Fermi surface after applying a band-pass filter. (b) Mass study plots for the 9 kbar and 20 kbar runs.

Pressure (kbar)	IFS Freq. (T)	m^*_{IFS}	OFS Freq. (T)	m^*_{OFS}
0.7	43 ± 4	-	499 ± 55	-
9.2	49 ± 4	0.057 ± 0.005	483 ± 42	0.16 ± 0.03
20.3	56 ± 5	0.0624 ± 0.0003	470 ± 40	0.16 ± 0.02

Table 4.1: Summary of the results for BiTeI zero percent excess iodine measured in piston cylinder cell. Mass studies at ambient pressure were not completed successfully.

The BiTeI sample was mounted alongside two other materials, and one of the contacts for another sample came off after pressurisation. A decision was made to open up the pressure cell in order to repair that sample and whilst doing so, contacts for the BiTeI

sample were damaged as well, thus this pressure study concluded at 20 kbar.

4.2.2 Moissanite Anvil Cell

For pressure studies of BiTeI above 30 kbar, the moissanite anvil cell was used. This cell was set up with the help of Dr Patricia Alireza with the sample wired up for a Hall measurement (see Figure 3.9) with glycerol as the pressure medium. The sample dimensions were $190 \times 200 \times 10$ μm^3 with an uncertainty of about 1 μm for the thickness. The plan was to do low pressure measurements on the PPMS to test whether the cell was working, before increasing the pressure for high field measurements in the dilution refrigerator. The cell survived pressurisation up to 21 kbar, but one of the sample contacts broke upon the next pressurisation, thus the pressure study concluded prematurely at 21 kbar. Nevertheless, this pressure cell run still gave us useful information regarding sample preparation and experimental setup. As we were still able to observe quantum oscillations from such small samples in the Hall signal, it gave us confidence in preparing samples with similar dimensions and geometries in the subsequent piston-cylinder run.

The plots below show the measurements taken from the PPMS. Figure 4.9 shows the resistance trace of BiTeI as the field is swept from -9 T to 9 T. We observe a non-zero resistivity signal at zero field, indicating that the voltage and current contacts may not be exactly opposite to each other, resulting in a small contribution in the longitudinal component of the resistivity being measured. Since the longitudinal component R_{xx} and the transverse component R_{xy} is expected to be symmetric and antisymmetric respectively under a reversal of magnetic field, the data can be symmetrised and antisymmetrised to obtain R_{xx} and R_{xy} as follows:

$$\begin{aligned} R_{xx}(H) &= \frac{R(+H) + R(-H)}{2}, \\ R_{xy}(H) &= \frac{R(+H) - R(-H)}{2}. \end{aligned} \tag{4.1}$$

The Hall coefficient R_H and hence the carrier density n can be obtained using equation 2.58. Rearranging the terms in the equation, we obtain:

$$R_{xy} = \frac{R_H}{t} B, \tag{4.2}$$

where we have used $\rho_{xy} = R_{xy}t$, with t being the thickness of the sample. Plotting R_{xy} against B gives a straight line with a slope of R_H/t. The sign of the slope tells us the type of carriers present in our sample and we can see from the negative slope in Figure 4.10b that our sample is n-type, with a carrier density of about 10^{21} cm^{-3}. Since the uncertainty obtained from the linear fit is very small, the overall uncertainty for the carrier density would be dominated by the uncertainty in the sample thickness which

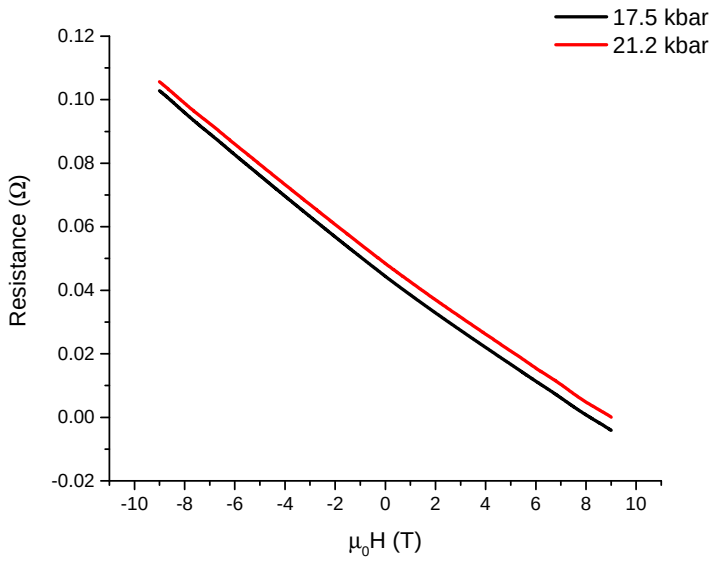

Figure 4.9: Field scan of BiTeI in the anvil cell from -9 T to 9 T. The data can be symmetrised and anti-symmetrised to obtain the longitudinal R_{xx} and transverse R_{xy} components respectively.

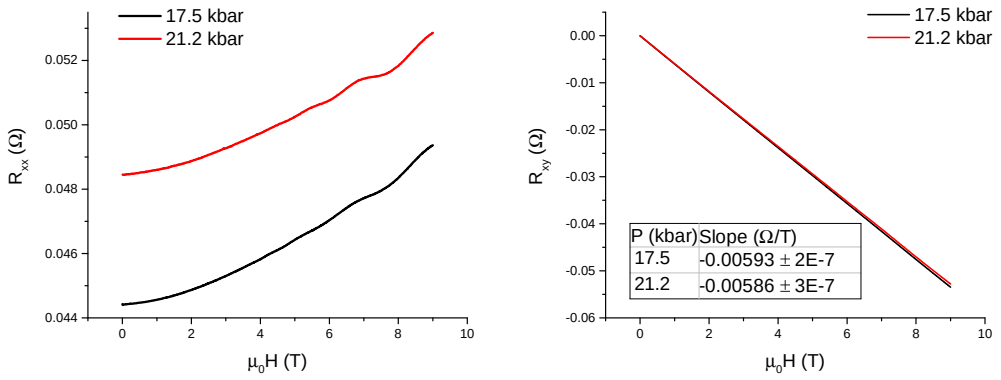

(a) (b)

Figure 4.10: (a) Longitudinal R_{xx} component of the resistance as a function of field. Quantum oscillations corresponding to the IFS sheets can be seen. (b) Transverse R_{xy} component as a function of field. The Hall coefficient can be obtained by taking the product of the slope with the thickness of the sample.

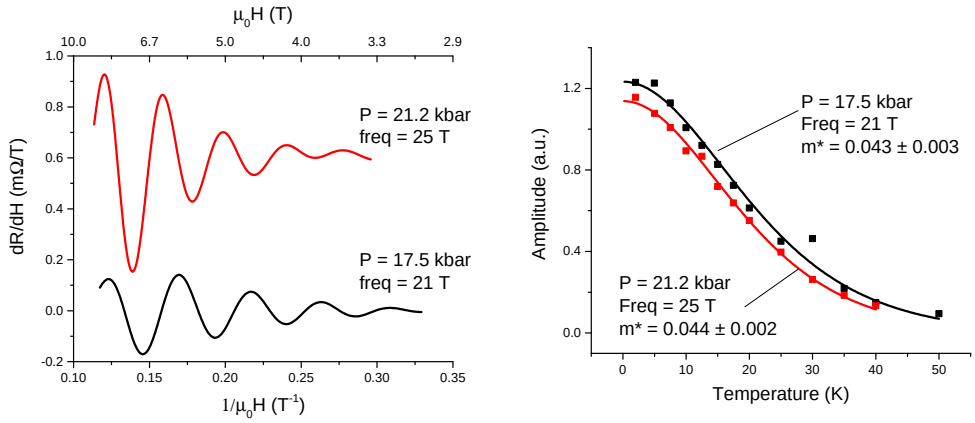

(a) (b)

Figure 4.11: (a) Band-pass filtered quantum oscillation data corresponding to the inner Fermi surface at 17.5 and 21.2 kbar. (b) Mass study plots used to determine the effective mass m^*.

Pressure (kbar)	IFS Freq. (T)	m^*_{IFS} (m_e)	R_H (cm^3 / Coul)	n (cm^{-3})
17.5	21 ± 3	0.043 ± 0.003	-0.059	$1.1(1) \times 10^{21}$
21.2	25 ± 3	0.044 ± 0.002	-0.059	$1.1(1) \times 10^{21}$

Table 4.2: Summary of the results for BiTeI zero percent excess iodine measured in the moissanite anvil cell.

has a fractional error of 10%.

Quantum oscillations corresponding to the inner Fermi surface sheet can be extracted from the longitudinal component after taking a derivative with respect to the magnetic field, followed by a second order polynomial background subtraction, similar to previous treatments. As the larger frequency oscillations from the OFS can only be observed at fields above 11 T, we were only able to track the IFS oscillations for this sample in the anvil cell. The IFS quantum oscillations are plotted against inverse field in Figure 4.11a alongside the mass study plots in Figure 4.11b. Similar to the sample measured in the piston cylinder cell, the IFS frequencies increased with increasing pressure from 21 T at 17 kbar to 25 T at 21 kbar. Even though the samples were cleaved from the same single crystal, both samples showed a different IFS oscillation frequency at similar pressures of 20 kbar (56 T for the piston-cylinder cell sample). This seems to indicate growth inhomogeneity along the crystal, resulting in slightly different characteristics of the sample, which is perhaps unsurprising since BiTeI is sensitive to the level of self-doping.

The Hall effect measurements, quantum oscillation frequencies and effective mass for the anvil cell sample for the two pressure points are summarised in Table 4.2.

From the study of the first batch of BiTeI crystals, it can be seen that the sample

is metallic with relatively high carrier concentration ($n \sim 10^{21}$ cm^{-3}). Kanou and Sasagawa [54] attributed this metallic behaviour to self-doping effects caused by iodine deficiencies arising from the growth method. Thus as a follow-up, new samples of BiTeI were grown under excess iodine conditions, with the hope of reducing non-stoichiometric effects and suppressing the metallic behaviour of BiTeI. It was also reported by Kanou and Sasagawa that their best quality samples came from the vapour transport growth method, thus one batch of BiTeI samples was grown using this particular method.

These samples of chemical vapour transport (CVT) grown BiTeI as well as those grown under 5 and 10 percent excess iodine were once again supplied by Prof. Geetha Balakrishnan from the University of Warwick. We will present results obtained from the 5 and 10 percent excess iodine in the subsequent section. The CVT samples were identified to be Bi_2Te_3 rather than BiTeI and will be discussed in the next chapter.

4.3 BiTeI Five Percent Excess Iodine

Thin flakes of BiTeI grown with five percent excess iodine (BiTeI +5%) were prepared using the exfoliation method described previously and they were cut into tiny squares with contacts placed at the corners for Hall measurements (Figure 3.10). These samples were mounted in a 24 mm diameter piston cylinder cell using Daphne oil 7373 as the pressure medium. The quantum oscillation measurements were carried out in the 15T system up to a pressure of 30 kbar.

The BiTeI +5% sample with gold wire spot-welded contacts was photographed under a microscope as shown in Figure 4.12. Sample dimensions were obtained by measuring

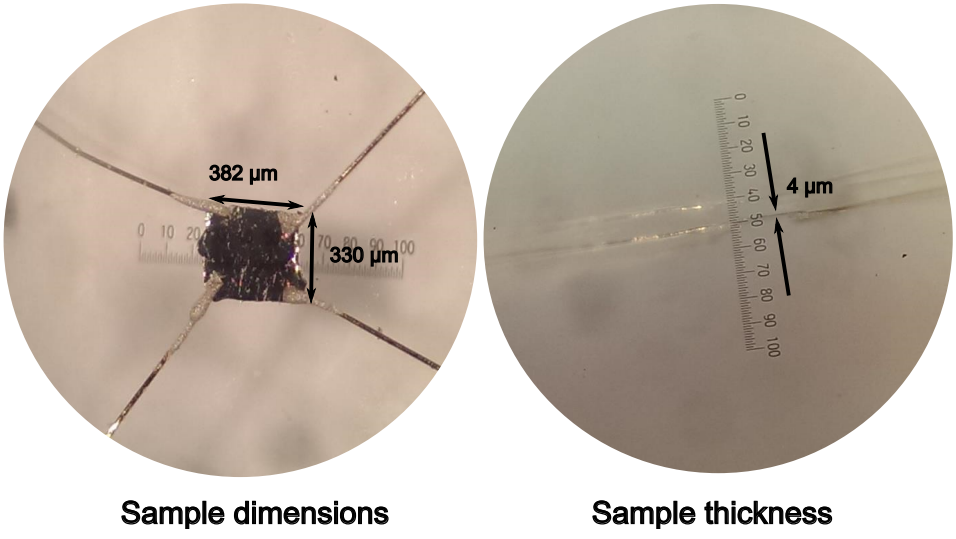

Figure 4.12: Left: BiTeI +5% sample with spot-welded gold wire contacts, strengthened with silver epoxy. Right: Sideways photograph for measuring thickness of sample.

the number of pixels in a image processing software (e.g. GIMP) and comparing that against the calibrated microscope scale in the photograph. The sample thickness was obtained in a similar manner by taking an image of the sample on its side. The uncertainty involved with using a digitised image is of the order of a few pixels, which is about 1 μm in physical dimensions. The dimensions obtained for the 5% sample are estimated to be $382 \times 330 \times 4$ μm^3.

4.3.1 Hall Measurements

Similar to the previous anvil cell, Hall measurements were carried out by sweeping the magnetic field in the positive and negative directions. The transverse component can then be obtained by anti-symmetrising the positive field and negative field signal.

The Hall measurements were measured using both the PPMS and the 15T system. For the 13.2, 17.6 and 19.7 kbar pressure points, the measurements were carried out in the PPMS, and so the R_{xy} data was only measured up to 9 T.

Figure 4.13 is a plot of R_{xy} against B after anti-symmetrisation. Similar to the first batch of samples, the transverse resistance varies linearly against field with a negative slope. Fitting the Hall measurement data with a straight line, the Hall coefficient and carrier densities can be obtained from the value of the slope and the results are presented in Table 4.3. Uncertainty in the carrier density is estimated based on the uncertainty in measuring the thickness of the sample – we obtained a fractional uncertainty of about 25% for this sample.

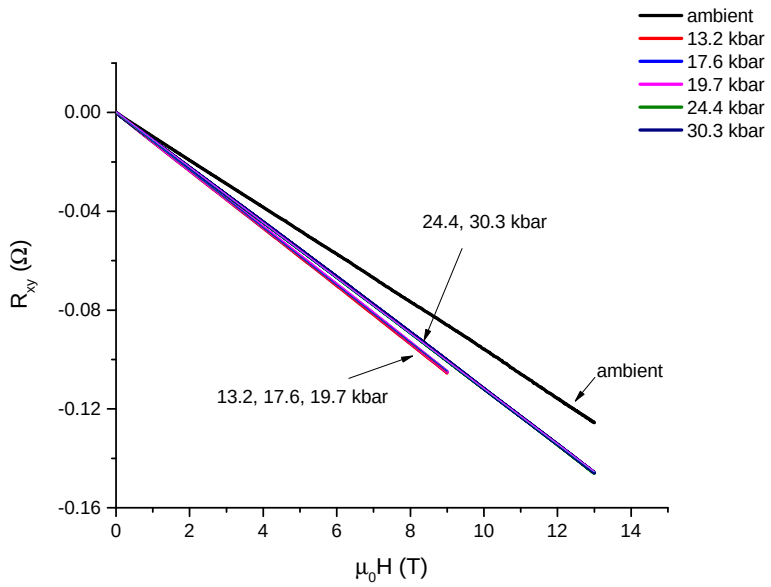

Figure 4.13: Antisymmetrised component R_{xy} as a function of field for different pressures.

Pressure (kbar)	ambient	13.2	17.6	19.7	24.4	30.3
R_H (cm^3 / Coul)	-0.038	-0.047	-0.046	-0.047	-0.045	-0.045
n (10^{20} cm^{-3})	1.6(4)	1.3(3)	1.3(3)	1.3(3)	1.4(4)	1.4(4)

Table 4.3: Summary of results obtained from Hall measurement of BiTeI +5%.

4.3.2 Quantum Oscillation Measurements

For the 5% sample, oscillations in the transverse component of the resistivity could be seen as the field was swept up to 15 T. The temperature of the probe was kept at 2 K by pumping on a bath of liquid helium at constant pressure.

Figure 4.14 is a plot of the quantum oscillation data against inverse field for different pressure points after performing a polynomial background subtraction. The data is then normalised by the zero field value and offset for clarity. Two frequencies, one corresponding to the IFS and the other to the OFS can be visually distinguished at all pressures up to 30 kbar.

Similar to the previous treatments, the quantum oscillations corresponding to the different sheets can be separated by applying a band-pass FFT filter centred along the respective FFT peaks for the IFS and OFS oscillations. The result is shown in Figure 4.15a and Figure 4.15b for the IFS and OFS oscillations respectively.

For the IFS quantum oscillations, the frequency at ambient pressure is determined to be 20 T both from the FFT spectrum peak as well as from direct fitting using the LK formula. It is also observed that as pressure is increased, the frequency shifts towards higher frequencies and undergoes a gradual splitting. Except for the ambient pressure run, a two-frequency LK fit produces a better fit compared to a one-frequency fit, and this is particularly evident at the higher pressures.

Using the 30 kbar pressure run as an example, the fit using two frequencies is compared with the fit using a single frequency as shown in Figure 4.16. The fits were carried out using Matlab's nonlinear least squares fitting function with the initial guess given by peaks in the FFT spectrum (see Figure 4.18) – 27 T and 41 T for the two-frequency fit, while the larger amplitude 27 T peak was used as the initial guess for the single-frequency fit. Visually, it is quite clear that the maxima and minima for the two-frequency fit lines up with that of the experimental data while the single-frequency fit does not reasonably reproduce the data.

This splitting of frequencies can also be observed in the FFT spectrum, especially at pressures above 20 kbar (Figure 4.18), where another peak can be clearly resolved. For pressure points for which the second FFT peak cannot be clearly resolved, the frequency of the second oscillation is obtained through fitting. The fitted curves (dashed lines)

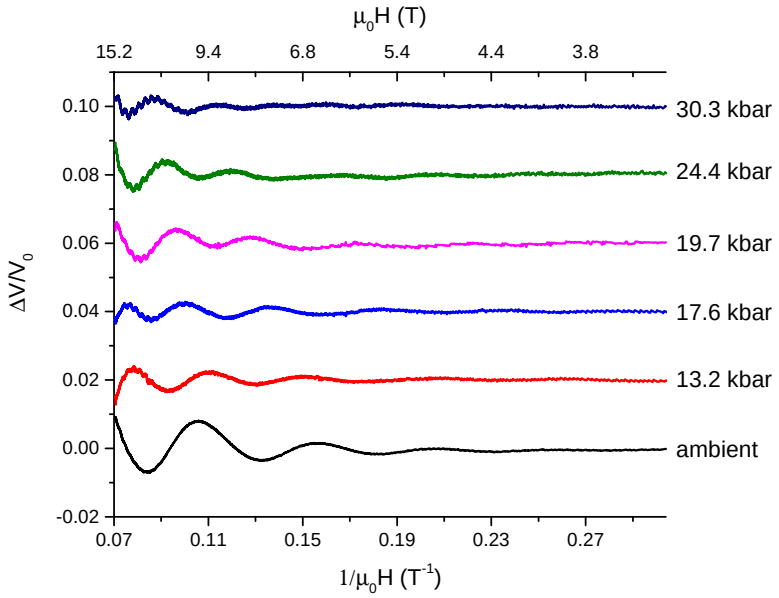

Figure 4.14: Normalised BiTeI +5% quantum oscillation data after polynomial background subtraction.

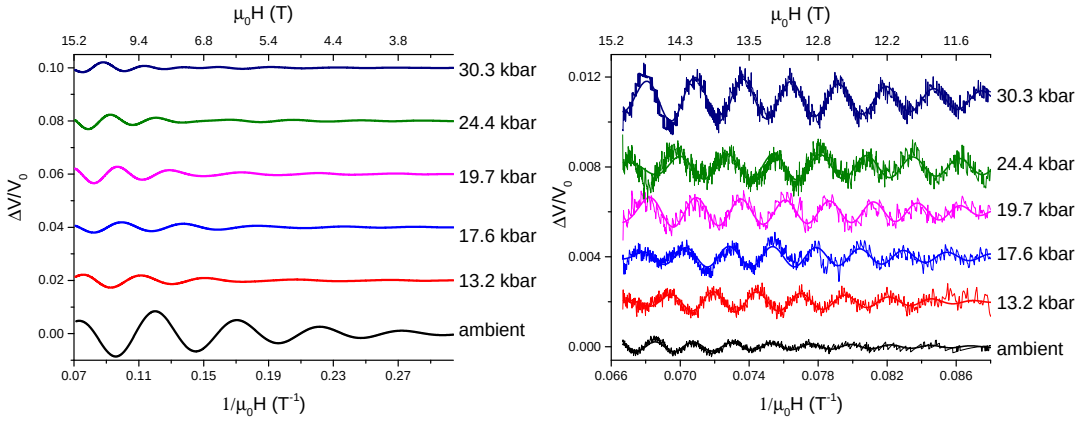

(a) (b)

Figure 4.15: Filtered signal corresponding to the (a) IFS and (b) OFS. In (b), the filtered signal is overlaid on top of the background subtracted data.

and raw data (solid lines) are plotted together in Figure 4.17 for comparison. In general, we see that the two frequency fits line up well with the experimental data, especially at higher pressures where the two frequencies are more distinct.

For the OFS quantum oscillations, the frequency at ambient pressure is determined to be 440 T. Figure 4.19 plots the background subtracted data (solid lines) together

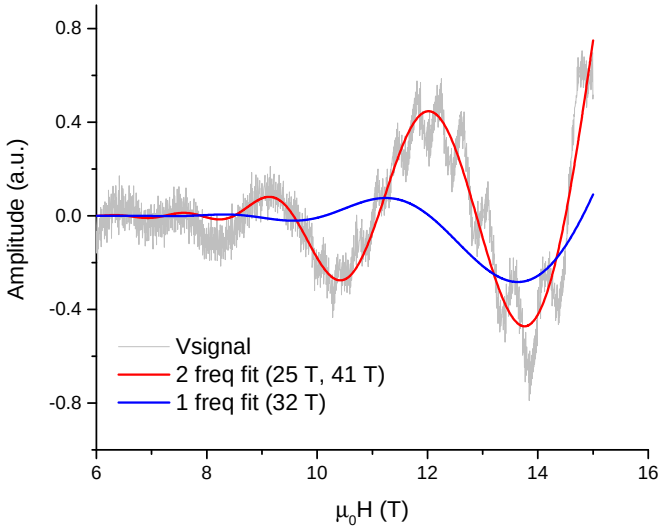

Figure 4.16: Measurement run at $P = 30$ kbar. At higher pressures, quantum oscillation data is better described by two-frequency fits rather than single-frequency fits.

with the LK curve fits (dashed lines). The OFS quantum oscillations can be observed at fields above 11 T at lower pressures, growing in amplitude and extending to lower fields as pressure is increased. The OFS frequency also shifts towards lower frequencies as pressure is increased, which can be seen from the general trend in the FFT spectrum plot (Figure 4.20). Similar to the IFS frequencies, there is good agreement (±3 T) between the frequencies obtained from the LK fits and from the peak position in the FFT spectrum.

The temperature dependences of the quantum oscillation amplitude for a few selected pressure points are shown in Figures 4.21 and 4.22 for the IFS and OFS respectively, with the rest of the results of the quantum oscillation study presented in Table 4.4.

Pressure (kbar)	IFS freq (T)	m^*_{IFS} (m_e)	OFS freq (T)	m^*_{OFS} (m_e)
ambient	20 ± 3	0.042 ± 0.001	440 ± 32	0.20 ± 0.02
13.2	21 ± 3	0.04 ± 0.01	393 ± 39	0.16 ± 0.04
	29 ± 4	0.04 ± 0.01		
17.6	23 ± 3	0.041 ± 0.004	392 ± 35	0.14 ± 0.05
	32 ± 2	0.046 ± 0.005		
19.7	23 ± 3	0.05 ± 0.01	389 ± 40	0.13 ± 0.02
	34 ± 9	0.05 ± 0.01		
24.4	24 ± 3	0.052 ± 0.003	370 ± 34	0.14 ± 0.02
	36 ± 4	0.051 ± 0.003		
30.3	27 ± 3	0.049 ± 0.009	359 ± 34	0.12 ± 0.01
	41 ± 4	0.045 ± 0.005		

Table 4.4: Summary of the results obtained from the quantum oscillation study of BiTeI +5%.

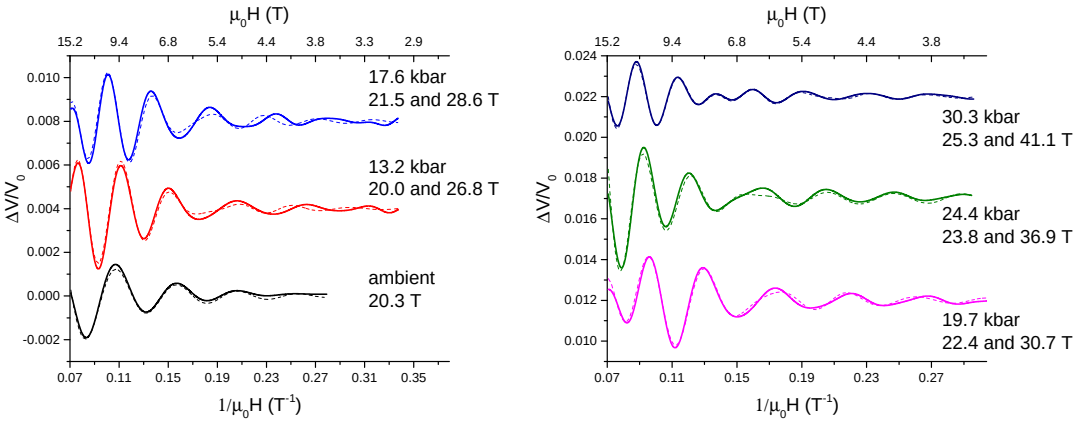

(a) (b)

Figure 4.17: Background-subtracted data (solid lines) plotted together with the fitted curves (dashed lines) for (a) ambient pressure to 18 kbar, (b) 20 kbar to 30 kbar for the IFS quantum oscillations.

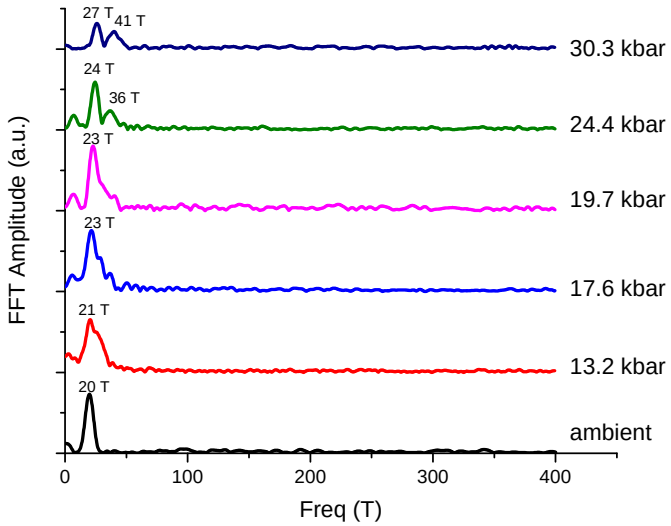

Figure 4.18: FFT spectrum of the IFS quantum oscillation frequencies for the various pressure points, offset for clarity. The FFT is taken over the field range of 2-15 T. The IFS quantum oscillation frequency shifts towards larger frequencies as pressure is increased. Moreover, the peak appears to split as pressure is increased, and two distinct peaks are observed at pressures above 20 kbar.

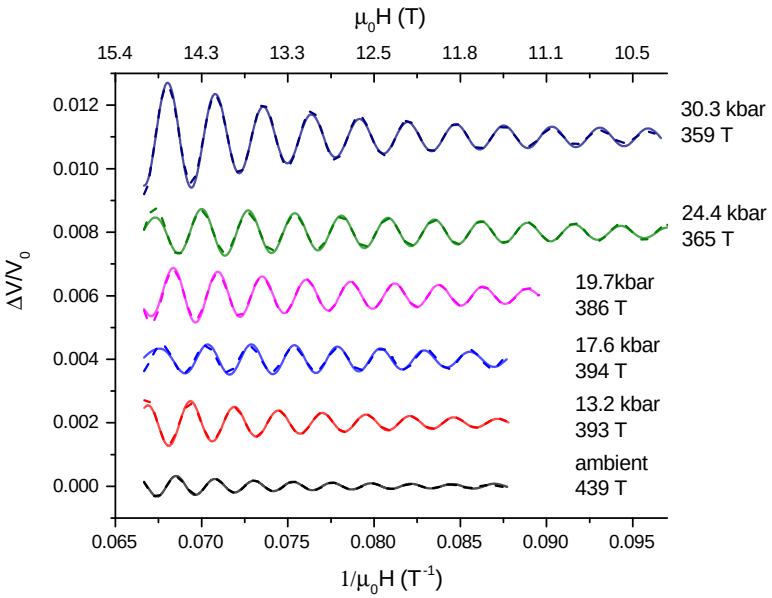

Figure 4.19: Background-subtracted data (solid lines) plotted together with the fitted curves using the LK formula (dashed lines) for the OFS quantum oscillations. The OFS quantum oscillations become discernible at magnetic fields above about 11 T at low pressures, extending to lower fields as pressure is increased.

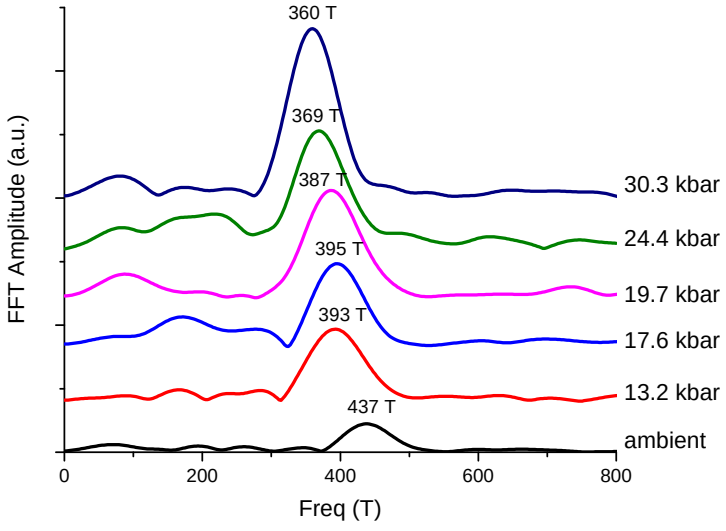

Figure 4.20: FFT spectrum of the OFS quantum oscillation frequencies for the various pressures, taken in the field range 10–15 T, and offset for clarity. The amplitude of the peak increases while the peak itself shifts towards lower frequencies as pressure is increased.

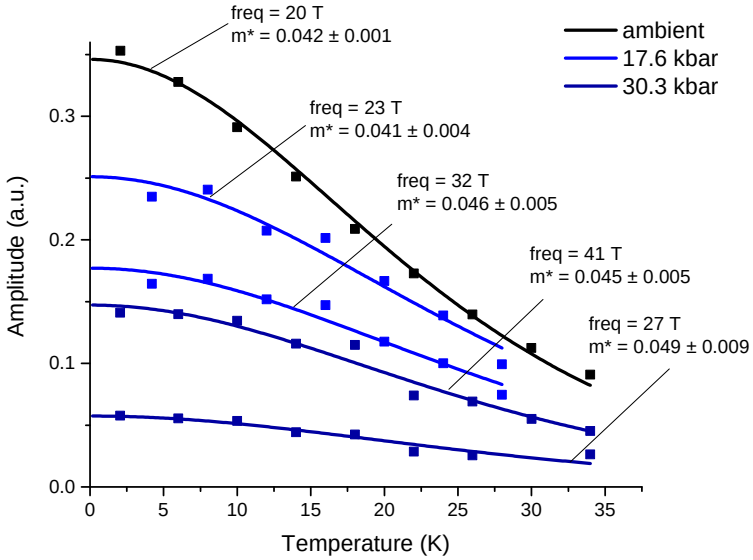

Figure 4.21: Temperature dependence of the normalised quantum oscillation amplitude for the IFS at selected pressures.

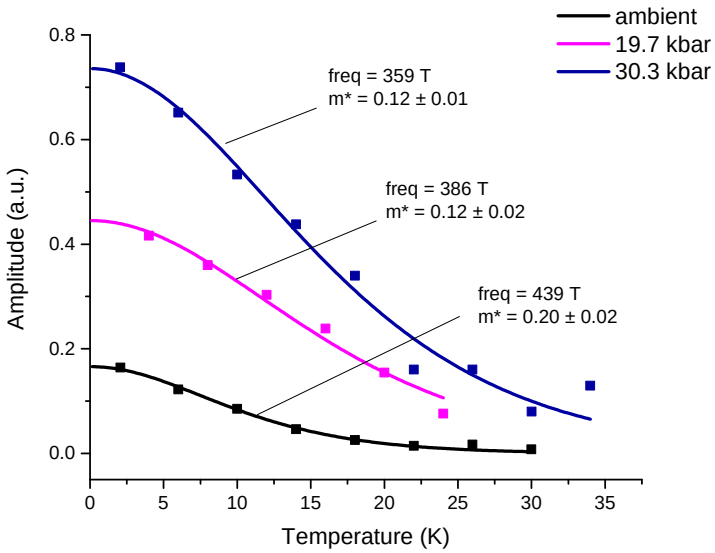

Figure 4.22: Temperature dependence of the normalised quantum oscillation amplitude for the OFS at selected pressures.

4.4 BiTeI Ten Percent Excess Iodine

The sample of BiTeI grown with ten percent excess iodine (BiTeI +10%) was prepared in a similar manner to the +5% sample, and the dimensions are measured to be 421 × 359 × 9 μm^3 with an uncertainty of about 1 μm.

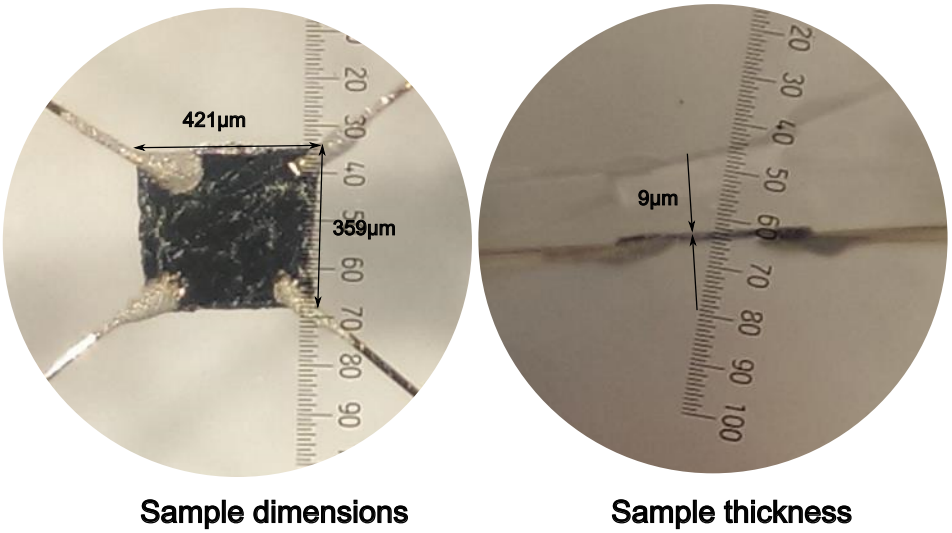

Figure 4.23: Left: BiTeI +10% sample with spot-welded gold wire contacts, strengthened with silver epoxy. Right: Sideways photograph for measuring thickness of sample.

4.4.1 Hall Measurements

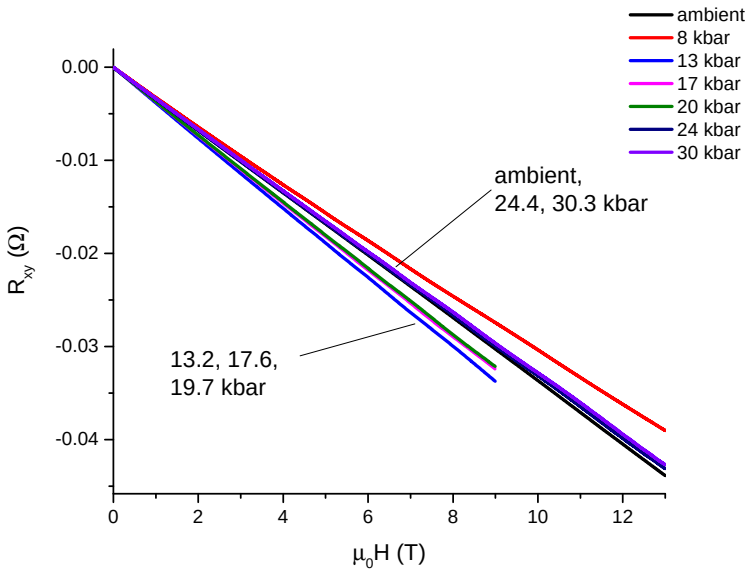

Figure 4.24: Anti-symmetrised component R_{xy} as a function of field for different pressures.

The Hall coefficient and carrier density are obtained from the slope of the plot of R_{xy} against magnetic field in Figure 4.24 and the values obtained at different pressures are presented in Table 4.5. The 10% and 5% samples have similar carrier densities with the 10% sample having a marginally higher carrier density.

Pressure (kbar)	ambient	8.0	13.2	17.6	19.7	24.4	30.3
R_H (cm^3 / Coul)	-0.030	-0.027	-0.034	-0.032	-0.032	-0.030	-0.029
n (10^{20} cm^{-3})	2.1(2)	2.3(3)	1.8(2)	1.9(2)	1.9(2)	2.1(2)	2.1(2)

Table 4.5: Summary of results obtained from Hall measurement of BiTeI +10%.

4.4.2 Quantum Oscillation Measurements

Like previous samples, the 10% sample also showed quantum oscillations corresponding to two distinct frequencies across the different pressure points as the magnetic field is swept to 15 T. The oscillations at each pressure point after performing background subtraction are shown in Figure 4.25.

The FFT spectra corresponding to the IFS quantum oscillations are plotted in Figure 4.26b, where the FFT is taken over the field range 3-15 T. A band-pass filter centred on the FFT peak is used to clean up the data before fitting it to the LK formula, with the resulting filtered signal and fitted curves plotted in Figure 4.26a. Apart from the anomaly at ambient pressure, the frequency for the IFS quantum oscillations generally

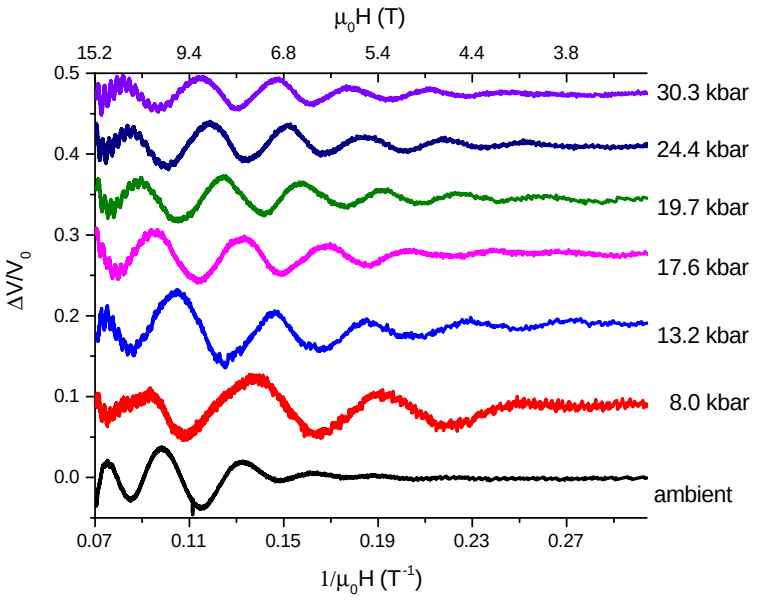

Figure 4.25: Normalised BiTeI +10% quantum oscillation data after polynomial background subtraction.

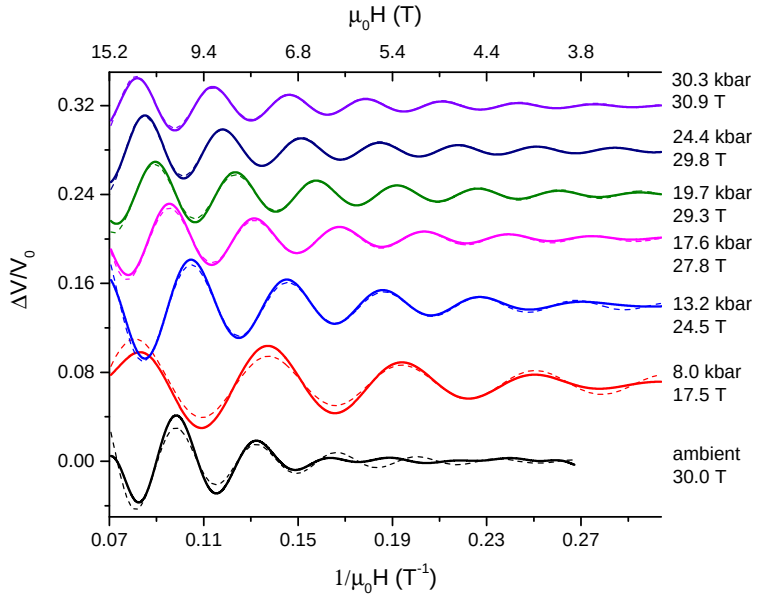

(a)

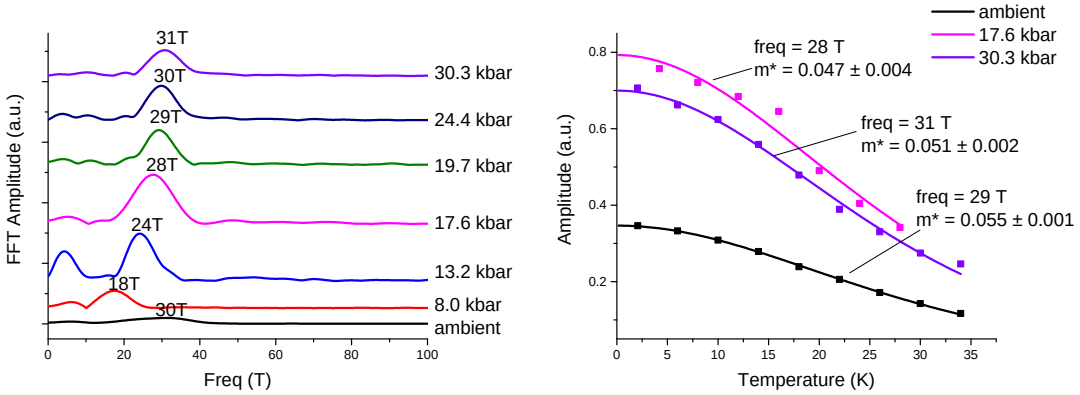

(b) (c)

Figure 4.26: (a) Filtered quantum oscillation data (solid lines) corresponding to the IFS. Fits using the LK formula are plotted in dashed lines. (b) FFT spectrum of the IFS frequencies. (c) Temperature dependence of the normalised quantum oscillation amplitude for the IFS at selected pressures.

increases with increasing pressure, consistent with measurements done on the 0% and +5% sample. However, unlike the +5% sample, this sample did not show any splitting of the IFS frequencies as pressure was increased.

The OFS quantum oscillations can be treated in a similar manner, by taking the FFT over the field range 10-15 T and applying a band-pass filter to the data. The filtered data and fits to the LK formula are plotted in Figure 4.27a and the FFT spectra is plotted in Figure 4.27b. As pressure was increased, the OFS frequencies show a gradual shift towards lower frequencies, alongside an increase in the amplitude of the FFT peak,

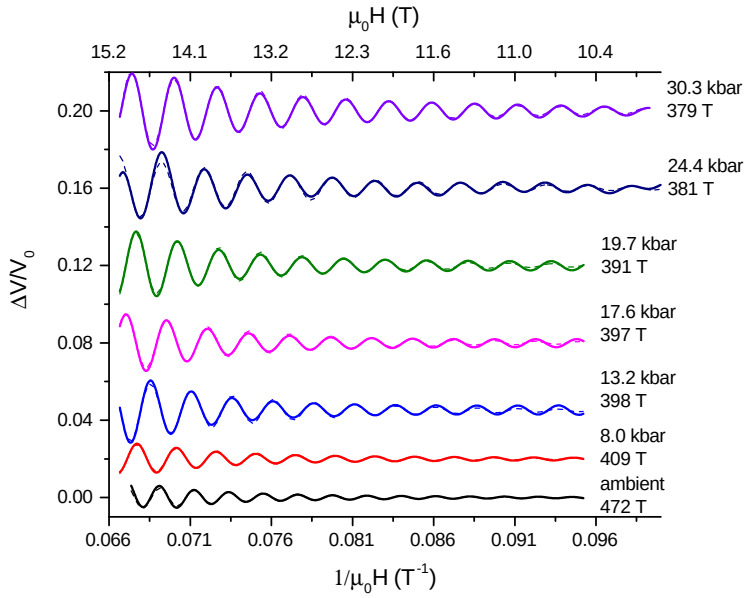

(a)

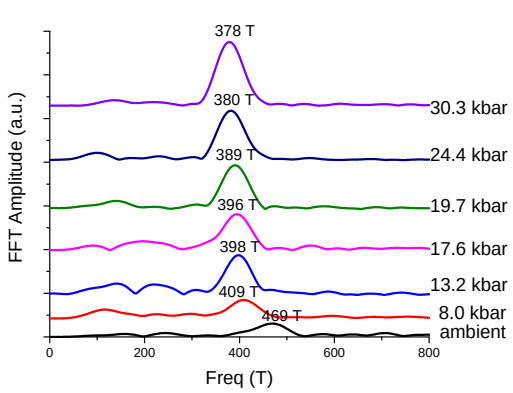

(b)

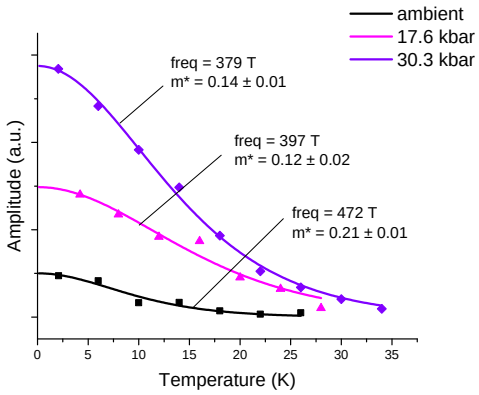

(c)

Figure 4.27: (a) Filtered quantum oscillation data (solid lines) corresponding to the OFS. Fits using the LK formula are plotted in dashed lines. (b) FFT spectrum of the OFS frequencies. (c) Temperature dependence of the normalised quantum oscillation amplitude for the OFS at selected pressures.

extending the field range in which the oscillations can be observed. The temperature dependence of the quantum oscillations for both the IFS and OFS at a few selected pressures are shown in Figures 4.26c and 4.27c respectively.

High field measurements conducted at the National High Magnetic Field Laboratory in Tallahasee were also carried out on the +10% sample at ambient pressure. The sample was retrieved from the pressure cell, and any broken contacts were fixed before it was sent over to Tallahassee. These were secondary measurements carried out by members of the group: Dr Jordan Baglo, Hui Chang and Konstantin Semeniuk, alongside the

primary pressure cell experiment. The samples were measured to fields of 34.5 T in a Helium-3 system with a base temperature of 0.4 K.

Sweeping to high fields enabled us to observe more periods that correspond to the OFS, as well as to check for frequencies belonging to other Fermi surface sheets that had not been observed due to the smaller field range back in Cambridge. The high field measurements showed two oscillation frequencies for our BiTeI sample, consistent with expectations and with results from our earlier runs.

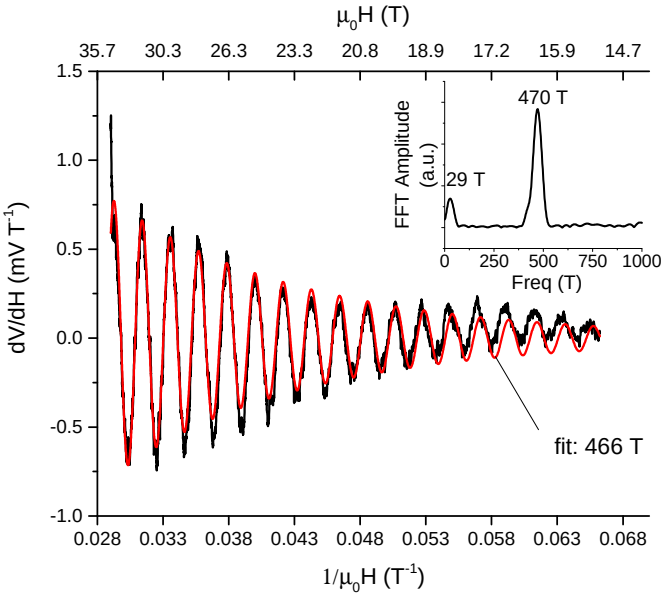

Figure 4.28: High field measurements of BiTeI +10%. Data is plotted after taking derivative with respect to field and after a linear background subtraction. Inset: FFT spectrum showing two peaks corresponding to IFS and OFS quantum oscillations.

Presented in Figure 4.28 is the quantum oscillation data when the field was swept from 15–34.5 T, with the FFT spectrum plotted in the inset. Assuming that the quantum oscillations corresponding to the IFS had a frequency between 20–30 T, it would have only gone through at most half a period in this field range, making it hard to distinguish the IFS quantum oscillations from artefacts caused by polynomial background subtraction. As such, a derivative of the signal with respect to the field, followed by a linear background subtraction was performed in order not to introduce any low frequency oscillations. The frequencies for both the IFS and OFS obtained from this measurement are in good agreement with the values obtained from the 15T system.

The results of the quantum oscillation study for BiTeI +10% sample are summarised in Table 4.6.

Pressure (kbar)	IFS freq (T)	m^*_{IFS} (m_e)	OFS freq (T)	m^*_{OFS} (m_e)
ambient (Tallahassee)	29 ± 19	-	466 ± 21	-
ambient (Cambridge)	30 ± 8	0.055 ± 0.001	472 ± 33	0.21 ± 0.01
8.0	18 ± 4	0.054 ± 0.005	409 ± 29	0.17 ± 0.03
13.2	25 ± 3	0.045 ± 0.004	398 ± 27	0.13 ± 0.03
17.6	28 ± 5	0.047 ± 0.004	396 ± 28	0.12 ± 0.02
19.7	29 ± 3	0.049 ± 0.004	391 ± 30	0.13 ± 0.02
24.4	30 ± 4	0.050 ± 0.002	380 ± 27	0.15 ± 0.01
30.3	31 ± 4	0.051 ± 0.002	378 ± 28	0.14 ± 0.01

Table 4.6: Summary of the results obtained from the quantum oscillation study of BiTeI +10%.

4.5 Discussion

4.5.1 Model Hamiltonian

The valence band maximum and conduction band minimum for BiTeI are located near the A point of the hexagonal shaped Brillouin zone (Figure 4.1b). Taking A as the origin, the conduction electrons near the band edge can be described by the Rashba Hamiltonian:

$$\mathcal{H} = \frac{\hbar^2 k_z^2}{2m_z} + \frac{\hbar^2 \boldsymbol{k}_\parallel^2}{2m_0} + \boldsymbol{\alpha} \cdot (\boldsymbol{\sigma} \times \boldsymbol{k}_\parallel) - \mu, \tag{4.3}$$

where the momentum $\boldsymbol{k}$ is decomposed into $\boldsymbol{k}_\parallel$ and k_z, components in the A-L-H plane and in the A-Γ direction respectively. m_0 and m_z are the corresponding in-plane and out-of-plane band masses, $\boldsymbol{\alpha}$ is the parameter describing the coupling strength of the Rashba interaction and is parallel to k_z, $\boldsymbol{\sigma}$ is the vector of Pauli matrices, and μ is the chemical potential.

Solving the Hamiltonian for the energy eigenvalues, we obtain the energy dispersion for our system:

$$E^{\pm}(k_x, k_y, k_z) = \frac{\hbar^2 k_z^2}{2m_z} + \frac{\hbar^2 (k_x^2 + k_y^2)}{2m_0} \pm \alpha \sqrt{k_x^2 + k_y^2} - \mu, \tag{4.4}$$

where '+' and '−' corresponds to the inner and outer Rashba sub-bands respectively.

The energy dispersion along the k_x direction (i.e. $k_z = k_y = 0$) is plotted in Figure 4.29a. For this system, the level of the chemical potential μ relative to the Dirac-point formed at the splitting of the sub-bands determines the topology of the Fermi surface. As μ changes from positive to negative, the three-dimensional Fermi surface of BiTeI evolves from that of a spindle-torus ($\mu > 0$), to a horn-torus ($\mu = 0$), to that of a ring-

torus ($\mu < 0$). This is visualised in Figure 4.29b by plotting the constant energy surface for the three different cases. We can see that when $\mu = 0$ at the Dirac point, the opposite walls of the inner Fermi surface touch each other such that for a magnetic field pointing in the k_z direction, there is only one quantum oscillation frequency corresponding to the outer Fermi surface.

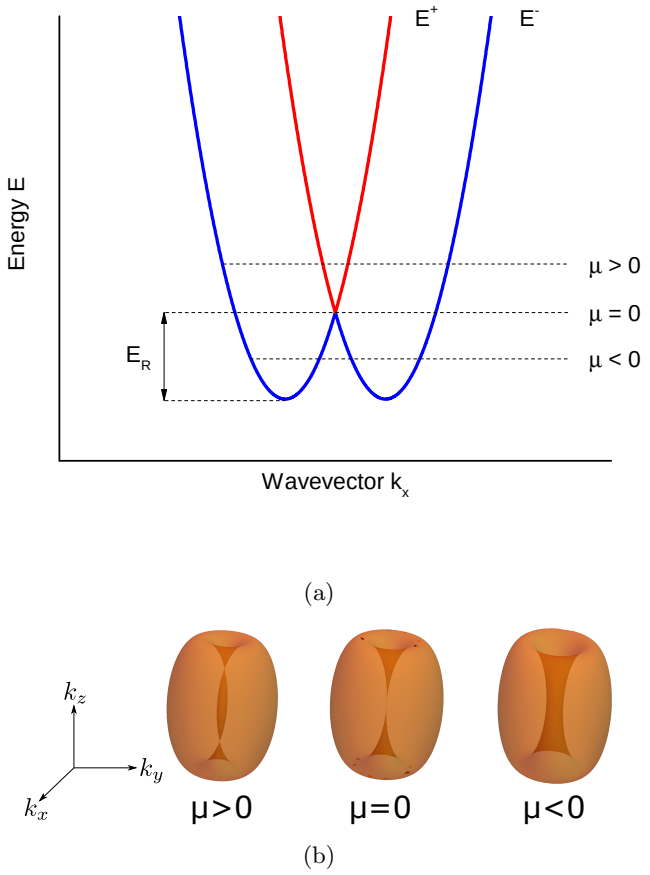

Figure 4.29: (a) Conduction band structure of the Rashba Hamiltonian taken along the $A - L$ direction. (b) Different Fermi surface topologies based on the level of the chemical potential: spindle-torus ($\mu > 0$), horn-torus ($\mu = 0$) and ring torus ($\mu < 0$).

4.5.2 Estimating Band Parameters From SdH Oscillations

As quantum oscillations probe the cross sectional area of the Fermi surface, we can derive how the band parameters in our model Hamiltonian are related to the quantum oscillation frequencies observed in experiments. When a magnetic field is applied along the z-direction, k_z remains a good quantum number while the energy levels are quantised

into Landau levels given by [52, 62]:

$$E_n^{\pm} = \hbar\omega_c \left(n \pm \sqrt{\frac{4E_R}{\hbar\omega_c} n + \Delta^2} \right), \quad n \geq 1, \tag{4.5}$$

where $\omega_c = \frac{Be}{m_0}$ is the cyclotron frequency, $\Delta = \frac{1}{2}(1 - \frac{gm_0}{2m_e})$ is the Zeeman term, with the effective g-factor and the bare electron mass given by g and m_e. $E_R = \frac{1}{2}m_0(\frac{\alpha}{\hbar})^2$ measures the minimum of the conduction band relative to the Dirac point.

Quantum oscillatory phenomena occurs whenever the n^{th} Landau tube crosses the Fermi surface, i.e. at magnetic fields in which $E_n = \mu$. Solving equation 4.5 for the cyclotron frequency ω_c in terms of n, we obtain a quadratic equation in terms of $\frac{1}{\hbar\omega_c}$:

$$\left(\frac{1}{\hbar\omega_c}\right)^2 - \left(\frac{1}{\mu} + \frac{2E_R}{\mu^2}\right)\frac{2n}{\hbar\omega_c} + \frac{n^2 - \Delta^2}{\mu^2} = 0. \tag{4.6}$$

Substituting $\omega_c = eB/m_0$, the solutions to equation 4.6 are given by:

$$\frac{m_0\mu}{\hbar e}\left(\frac{1}{B_n^{\pm}}\right) = n\left(1 + \frac{2E_R}{\mu}\right) \pm \sqrt{4\left(\frac{E_R}{\mu}\right)\left(1 + \frac{E_R}{\mu}\right) + \Delta^2}. \tag{4.7}$$

For small values of Δ, equation 4.7 can be expanded in powers of Δ as

$$\frac{m_0\mu}{\hbar e}\left(\frac{1}{B_n^{\pm}}\right) = n\left(1 + 2f \pm 2\sqrt{f(1+f)}\right) + \mathcal{O}\left(\frac{\Delta^2}{4n\sqrt{f(1+f)}}\right), \tag{4.8}$$

where we have simplified the notation by writing $f = \frac{E_R}{\mu}$.

It can be seen from equation 4.8 that the Landau index plots obtained by plotting inverse field $(1/B_n)$ against peak index (n) will be linear down to the lowest n provided that the Zeeman term Δ is small. From our own measurements carried out using the 15 T magnet and also at the high field facility, the linearity of the index plots (see Figures 4.40, 4.41, 4.39) justifies this assumption, and we will drop the last term when deriving the quantum oscillation cyclotron mass in terms of f.

The period of the quantum oscillations measured in inverse field is given by:

$$\Delta\left(\frac{1}{B^{\pm}}\right) = \frac{1}{B_{n+1}} - \frac{1}{B_n} = \frac{\hbar e}{m_0\mu}\left(\sqrt{1+f} \pm \sqrt{f}\right)^2, \tag{4.9}$$

and the frequency $F^{\pm}$, is just the reciprocal of the period:

$$F(\mu)^{\pm} = \left[\Delta\left(\frac{1}{B^{\pm}}\right)\right]^{-1} = \frac{m_0\mu}{\hbar e}\left(\sqrt{1+f} \mp \sqrt{f}\right)^2, \tag{4.10}$$

where F^+ and F^- are the frequencies of the inner and outer Fermi surfaces respectively, expressed in terms of the band parameters m_0, α and μ. The quantum oscillation

frequencies can be plotted as a function of chemical potential μ as shown in Figure 4.30. When the chemical potential is at the Dirac point (i.e. $\mu = 0$), the terms inside the bracket cancel for F^+, and the associated quantum oscillation frequency for the inner Fermi surface vanishes.

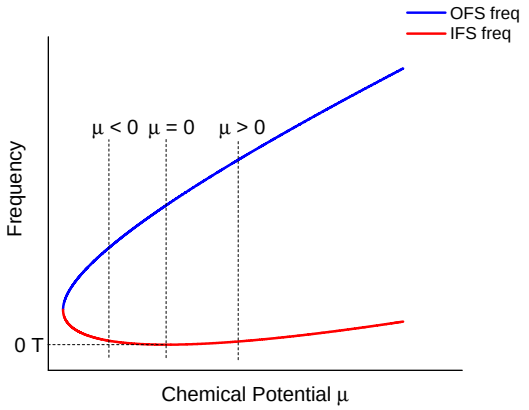

Figure 4.30: Qualitative plot of the quantum oscillation frequencies as a function of μ.

Thus far, we have two equations expressed in terms of three unknowns: m_0, α, μ. In order to solve for the three band parameters, we can bring in the cyclotron masses obtained from the temperature dependence of the Shubnikov-de Haas oscillation amplitude. From equation 2.8, the effective mass for quasi-particles undergoing cyclotron motion is proportional to the derivative of the area of the orbit, evaluated at the Fermi level:

$$m^* = \frac{\hbar^2}{2\pi}\frac{\partial A}{\partial E}\Big|_{E=\mu}. \tag{4.11}$$

Recalling that $A = \frac{2\pi e}{\hbar}F$ and using the expression of $F^{\pm}$ from equation 4.10, the derivative can be evaluated so that the effective mass $m^{*\pm}$ associated with the inner and outer Fermi surfaces can be written as:

$$m^{*\pm} = m_0\left(1 \mp \frac{\sqrt{f}}{\sqrt{f+1}}\right). \tag{4.12}$$

Comparing equations 4.10 and 4.12, the ratio of the effective masses m^{*+} and m^{*-} is found to depend on the square root of the ratio of frequencies F^+ and F^-:

$$\frac{m^{*+}}{m^{*-}} = \frac{\sqrt{1+f}-\sqrt{f}}{\sqrt{1+f}+\sqrt{f}} = \sqrt{\frac{F^+}{F^-}}. \tag{4.13}$$

Using equations 4.10 and 4.12, we are able to use the measured values of the SdH oscillation frequencies and their corresponding effective masses to estimate the values of

the band parameters, while equation 4.13 serves as a consistency check.

4.5.3 Band Parameters Obtained From SdH Oscillations

Solving for the band parameters m_0, α, μ at different pressure points using the frequencies and effective masses obtained from the quantum oscillation experiments, the results are shown in Table B.1 in Appendix B. The pressure dependence of the band parameters α, E_r, m_0 and μ are plotted in Figure 4.31.

Without enough data points to fit each concentration individually, we take a coarse-grained approach and assume that the three different samples of BiTeI behave in a similar manner under pressure – approximating the 'average' pressure dependence of the parameters via a linear fit. Up to the pressure range reached in the experiments, the Rashba interaction term α shows little variation with pressure while the band mass m_0 (and thus also E_r) decreases slightly with pressure. The chemical potential μ on the other hand increases with pressure.

Substituting the values of α, m_0 and μ back into the Rashba dispersion relation equation 4.4, we can plot how the electronic structure near the bottom of the conduction band changes with pressure. Figure 4.32 presents how the energy dispersion of our model Hamiltonian would evolve with pressure. It is evident from the plot that the sub-bands $E+$ (corresponding to the inner Fermi surface) expand with pressure while sub-bands $E-$ (corresponding to the outer Fermi surface) shrink with pressure – consistent with the trends observed from the quantum oscillation pressure study. Furthermore, we also see that with increasing pressure, the bottom of the conduction band is pushed lower towards the valence band. Although this is consistent with the prediction of band gap closing by Baharamy *et al.* [18], the magnitude of the change does not show a significant decrease in the band gap of the system.

In order to quantify the effect of pressure on the closure of the band gap, we first assume that the valence band and the conduction band gets pushed towards each other by the same amount. Using a value of 0.33 eV for the band gap (obtained by averaging the reported values of between 0.28 and 0.38 eV [65, 53, 18]), we can do a linear extrapolation to estimate what pressures are required for closing the band gap in BiTeI. From Figure 4.33, the linear fit gives the rate of decrease in the band gap energy as 2.1 meV/kbar, which translates to a band gap closure at a critical pressure $P_c \sim 160$ kbar. This is not consistent with the P_c of around 17 to 41 kbar predicted in [65]. However, our simple model does not take into account higher order effects such as coupling between conduction bands and valence bands, which may become more prominent closer to the critical pressure.

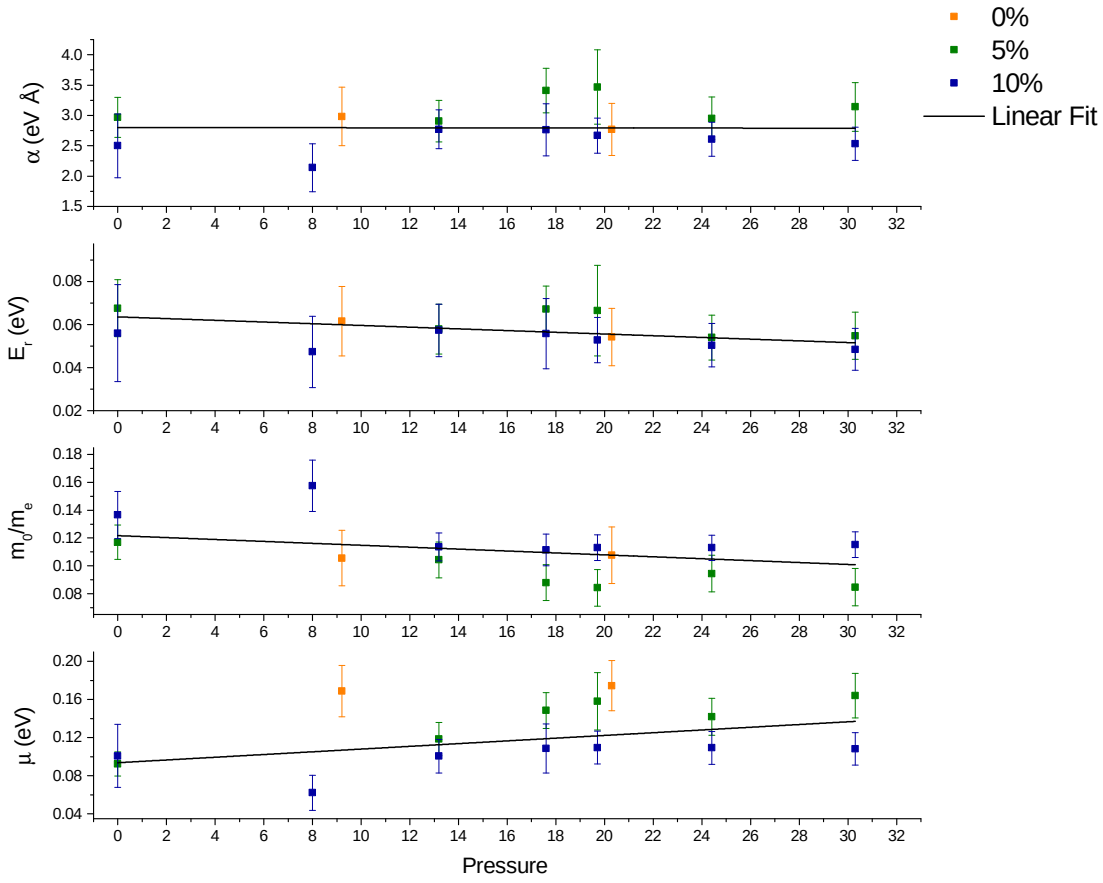

Figure 4.31: Plot of calculated band parameters as a function of pressure. Approximating the pressure dependence of the parameters with a linear fit, the Rashba coupling term α appears to be pressure independent, while the other three parameters show a slight variation in pressure – negative for E_r and m_0 and positive for μ.

4.5.4 Carrier Concentration

Having estimated values for the band parameters, the carrier concentration n of the material can be determined by calculating the volume enclosed by the Fermi surface using equation 2.38

$$n = \frac{N}{V} = \frac{2}{(2\pi)^3} \int \mathrm{d}\boldsymbol{k}\ \Theta(E_f - \varepsilon(\boldsymbol{k})). \qquad \text{(2.38 revisited)}$$

Substituting the Rashba band dispersion given by equation 4.4 into $\varepsilon(\boldsymbol{k})$, the expression can be evaluated analytically by performing the integration in the cylindrical polar coordinates system. The final result written in full is given by:

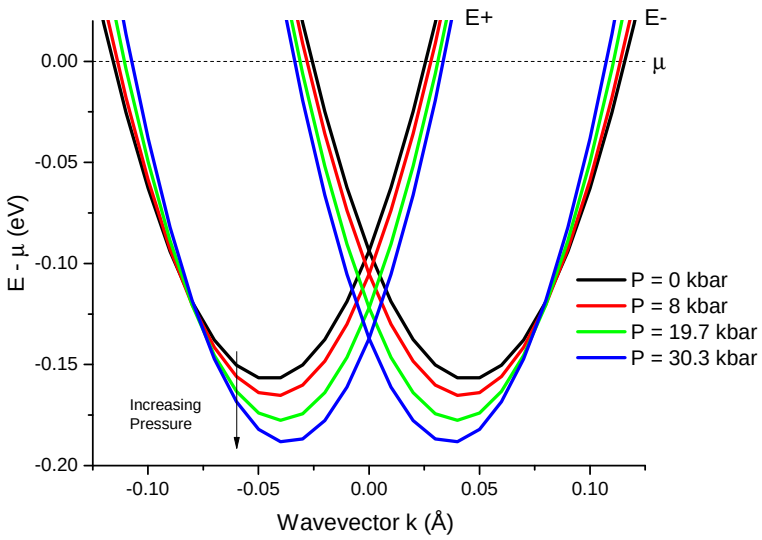

Figure 4.32: Evolution of band structure with pressure; bottom of conduction band is pushed closer towards the valence band. The band structure is calculated using parameters at four pressure points.

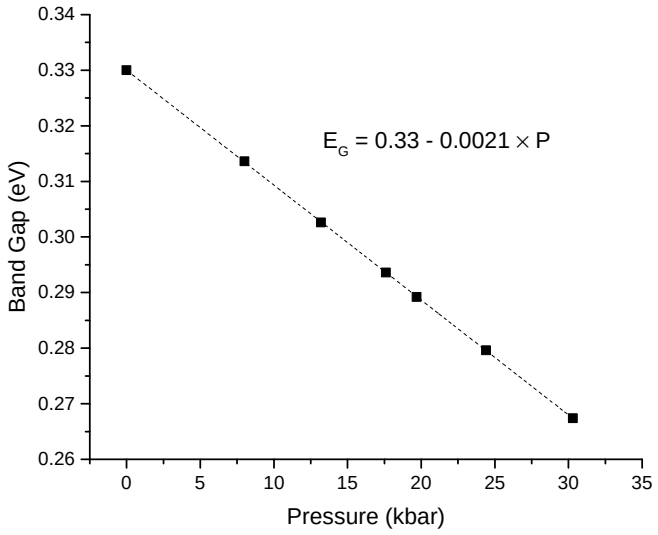

Figure 4.33: Closing of band gap with pressure, estimated using model parameters derived from SdH oscillations.

$$n^{\pm} = \frac{1}{\pi^2}\sqrt{\frac{m_z}{m_0}}\left\{-\frac{1}{3}(a^2-\rho^2)^{\frac{3}{2}} \pm \frac{\alpha m_0}{2\hbar^2}\left[\rho\sqrt{a^2-\rho^2} - a^2\arctan\left(\frac{-\rho}{\sqrt{a^2-\rho^2}}\right)\right]\right\}_{\rho=ll}^{\rho=ul}, \tag{4.14}$$

where the variables are defined:

- n^+ and n^- are the carrier concentrations from the inner and outer Rashba bands respectively,
- $a^2 = \left(\frac{\alpha m_0}{\hbar^2}\right)^2 + m_0\mu$,
- ul and ll are the upper and lower limits for the integration, given by:

$$ul^+ = a, \qquad ul^- = a,$$
$$ll^+ = \frac{\alpha m_0}{\hbar^2}. \qquad ll^- = -\frac{\alpha m_0}{\hbar^2}.$$

Using the ambient pressure values for the parameters (α, m_0, μ) obtained from our experiments, and a value for m_z given by $m_z \sim 5m_0$ obtained from optical studies [66], the carrier concentration is computed for the 0%, +5%, +10% excess iodine samples of BiTeI. The results are shown in Table 4.7 alongside the results obtained from the Hall measurements for comparison:

	Calculation (cm^{-3})	Hall Measurements (cm^{-3})
BiTeI 0%	1.1×10^{20}	$1.1(1) \times 10^{21}$
BiTeI +5%	0.84×10^{20}	$1.6(4) \times 10^{20}$
BiTeI +10%	0.98×10^{20}	$2.1(2) \times 10^{20}$

Table 4.7: Comparison between calculated carrier concentrations and measurements at ambient pressure.

For the 0% excess iodine sample, although the samples were cleaved from the same crystal growth batch, the sample that was contacted for the Hall measurement (carried out in an anvil pressure cell) was different to the one that was measured in the piston cylinder cell. Unfortunately, only the low quantum oscillation frequencies were observed in the anvil cell setup so there was insufficient information to infer the model parameters; while the sample in the piston cylinder cell was not prepared for performing a Hall measurement. Thus the calculated and measured quantities for carrier concentration can only be indirectly compared via two different samples cleaved from the same growth batch, and the numbers obtained from the two methods differ by a factor of 10. For subsequent experiments using the +5% and +10% excess iodine samples, we ensured

that both quantum oscillation studies and Hall measurements could be carried out on the same sample and we see that the calculated carrier concentrations are about a factor of 2 smaller than those obtained from Hall measurements, lending support that the model Hamiltonian captures the essential physics that is happening in the bulk at ambient pressures.

The band parameters obtained from the linear fits can also be used to calculate and predict the carrier concentration as a function of pressure in Table 4.8. The calculated values show a small decrease in the carrier concentration as pressure increases; this can be explained by the larger rate of decrease in the outer Fermi surface compared to the increase in the inner Fermi surface, resulting in an overall decrease in the Fermi surface volume. However, it is difficult to observe this small decrease in the carrier concentration in the Hall effect results due to the uncertainties (e.g. sample thickness) in the experimental measurements.

Pressure (kbar)	Calculated Carrier Concentration (10^{20} cm^{-3})	Hall Measurements (10^{20} cm^{-3})	
		BiTeI +5%	BiTeI +10%
0	0.84	1.6 ± 0.4	2.1 ± 0.2
8	0.82	-	2.3 ± 0.3
13.2	0.80	1.3 ± 0.3	1.8 ± 0.2
17.6	0.79	1.3 ± 0.3	1.9 ± 0.2
19.7	0.78	1.3 ± 0.3	1.9 ± 0.2
24.4	0.77	1.4 ± 0.4	2.1 ± 0.2
30.3	0.74	1.4 ± 0.4	2.1 ± 0.2

Table 4.8: Calculated carrier concentrations as a function of pressure.

4.5.5 Landau Level Indexing and Phase Analysis

Ambient Pressure Longitudinal Resistivity

As mentioned in section 2.3.1, the transverse and longitudinal components of resistivity need to be extracted in order to obtain the conductivity σ_{xx}, so that the Landau level indexing and phase analysis can be correctly done. In this section, we present our analysis used for extracting the quantum oscillation phase factor and results of the phase as a function of pressure.

Since the samples were prepared such that they were approximately square in shape (roughly 300 to 400 μm for each side) and made very thin (less than 10 μm thick) by exfoliation, the van der Pauw method [67] is suited for measuring the resistivity of these sample geometries.

Using the numbering convention in Figure 4.34, the resistance measurement $R_{12,34} = V_{34}/I_{12}$ corresponds to the voltage drop V between contacts 3 and 4 when a current I

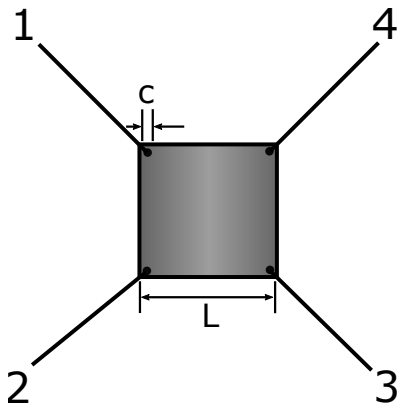

Figure 4.34: Contacts laid out for performing a van der Pauw resistivity measurement. The size of the contacts and length of the sample are labelled as c and L respectively.

is passed across contacts 1 and 2. In his paper, van der Pauw showed that the sheet resistance R_s of an arbitrarily shaped sample can be determined from two generalised resistance measurements – for example the vertical edge resistance $R_{12,34}$ and the horizontal edge resistance $R_{23,41}$.

The sheet resistance is related to these two quantities according to

$$e^{-\pi R_{12,34}/R_s} + e^{-\pi R_{23,41}/R_s} = 1. \tag{4.15}$$

We expect that interchanging voltage and current contacts should result in the same resistance measurement, thus we can make two additional reciprocal measurements $R_{34,12}$ and $R_{41,23}$ so that the values can be averaged for additional accuracy.

The relevant equations thus become

$$\begin{aligned} R_{vert} &= \frac{R_{12,34} + R_{34,12}}{2}, \\ R_{hor} &= \frac{R_{23,41} + R_{41,23}}{2}, \\ e^{-\pi R_{vert}/R_s} + e^{-\pi R_{hor}/R_s} &= 1, \end{aligned} \tag{4.16}$$

where R_{vert} and R_{hor} are the averaged values for the 'vertical' and 'horizontal' resistance values respectively. The van der Pauw relation can be solved numerically for the value of the sheet resistance, and given the thickness t of the sample, the average longitudinal resistivity ρ_{xx} can be obtained using $\rho_{xx} = R_s t$.

The van der Pauw technique assumes that the electrical contacts to the samples are point-like; whereas in reality, this is difficult if not impossible to achieve, especially for small samples used for pressure cell measurements and also when conductive paste is applied to strengthen the contacts. Analysis done by Look [68] showed that the correction factor $\Delta\rho/\rho$ due to finite sized contacts for a square sample is proportional to $(c/L)^2$,

where c is the size of the contact and L is the length of the sample. By measuring the ratio c/L from the digital photographs of the samples, the measurement error is estimated to be between 4–5%.

The van der Pauw measurements were carried out after the samples were retrieved from the piston cylinder cell, and they were measured at temperatures of 2 K using the Helium-4 probe. The samples were first contacted to measure R_{vert} before rewiring current and voltage leads to measure R_{hor}. The sheet resistance and longitudinal resistivity were calculated from these values and the results are presented in Table 4.9.

Sample	R_{hor}(mΩ)	R_{vert}(mΩ)	R_s(mΩ)	ρ_{xx}($\mu\Omega$-m)	ρ_{xy}($\mu\Omega$-m)	ρ_{xy}/ρ_{xx}
+5%	2.67	10.9	26(1)	0.12(3)	0.5(1) (13 T)	4(1)
+10%	15.9	2.46	32(2)	0.31(4)	0.39(4) (13 T)	1.3(2)
Murakawa [26]	-	-	-	6.9	2.0 (14 T)	0.3
Park [27]	-	-	-	1.6	2.5 (15 T)	1.6

Table 4.9: Van der Pauw technique for measuring longitudinal resistivity compared against transverse resistivity. Resistivity values for our samples are slightly smaller compared to samples in previously published work.

Using equation 2.48 to convert ρ_{xx} and ρ_{xy} into longitudinal conductivity σ_{xx}, we were not able to resolve the quantum oscillations in $\Delta\sigma_{xx}$ after performing the background subtraction on the longitudinal conductivity. This might be due to the phase difference between the oscillations in the ρ_{xy} and ρ_{xx} components, causing the overall oscillations in σ_{xx} to be smeared out. Without observing oscillations in $\Delta\sigma_{xx}$, we can only assume that we are in or close to the regime $\rho_{xx} < \rho_{xy}$ such that $\Delta\sigma_{xx} \sim \Delta\rho_{xx}$ based on the relative magnitudes of the measured ρ_{xy} and ρ_{xx} components (see equation 2.50). This implies that the equation to use for performing the phase analysis is

$$\Delta\rho_{xx} \sim \Delta\sigma_{xx} \sim \cos\left[2\pi\left(\frac{F}{B} - \gamma + \delta\right)\right]. \tag{4.17}$$

This conclusion is supported by the work done by Murakawa *et al.* [26], where they have also used this equation as a starting point for performing the Landau level indexing. Moreover, Park *et al.* [27] managed to observe oscillations in the conductivity component and showed that oscillations in σ_{xx} are in phase with oscillations in ρ_{xx}, justifying the use of equation 4.17 for performing Landau level indexing.

In both papers, resistivity measurements for both components are published and can

be digitised for comparison. The values for the transverse and longitudinal component for their samples are shown in Table 4.9 and comparing the ratio ρ_{xy}/ρ_{xx} between the different samples, our samples are quite similar to Park's samples in that the transverse component is larger than the longitudinal component of resistivity. It is noted that the measured components of resistivity for our samples are about an order of magnitude smaller than those reported by them. This is consistent with their observation of a lower carrier concentration ($10^{19}\,\mathrm{cm}^3$) as compared to $10^{20}\,\mathrm{cm}^3$ for our samples and indicates that our samples are slightly more metallic compared to theirs (see figure 4.35).

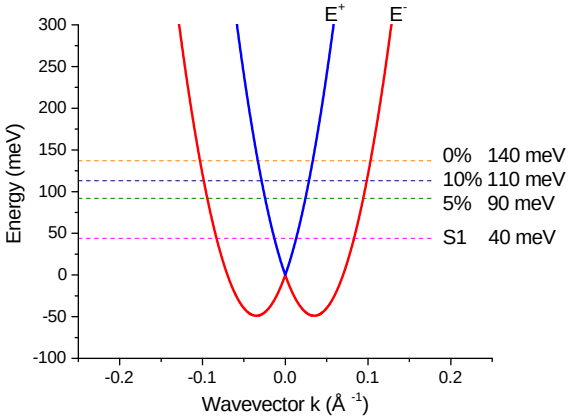

Figure 4.35: Chemical potentials of different samples of BiTeI grown under 0%, 5%, and 10% excess iodine. S1 is sample 1 from Park's measurements [27]. The samples are plotted together for comparison.

In order to extract the phase factor from equation 4.17, it is convenient to assign integer indices to the positions of ρ_{xx} maxima and half-integer indices to the positions of ρ_{xy} minima.[2] Oscillations take on a maximum whenever the argument in the cosine function is a multiple of 2π, i.e. for the N-th maximum:

$$\begin{aligned} 2\pi\left(\frac{F}{B_N} - \gamma + \delta\right) &= 2N\pi, \\ N &= \frac{F}{B_N} - \gamma + \delta. \end{aligned} \tag{4.18}$$

Thus, a plot of N against $1/B_N$ would yield a straight line with a slope F corresponding to the quantum oscillation frequency and an intercept of $\gamma + \delta$ as $1/B_N \to 0$. For systems that exhibit non-trivial Berry phase, $\gamma = 0$ and the expected intercept would be between δ, that is 0 or $\pm 1/8$ depending on the dimensionality of the system. As a reminder, for systems that have a trivial Berry phase, $\gamma = 0.5$ and the expected intercept would be $0.5 + \delta$.

[2]Once the relationship between σ_{xx} and ρ_{xx} is determined, the convention adopted for Landau level indexing does not matter as long as the algebra for working out the intercept is done consistently. For example, if integer indices are assigned to minima, the intercept would be $1/2 - \gamma + \delta$ instead.

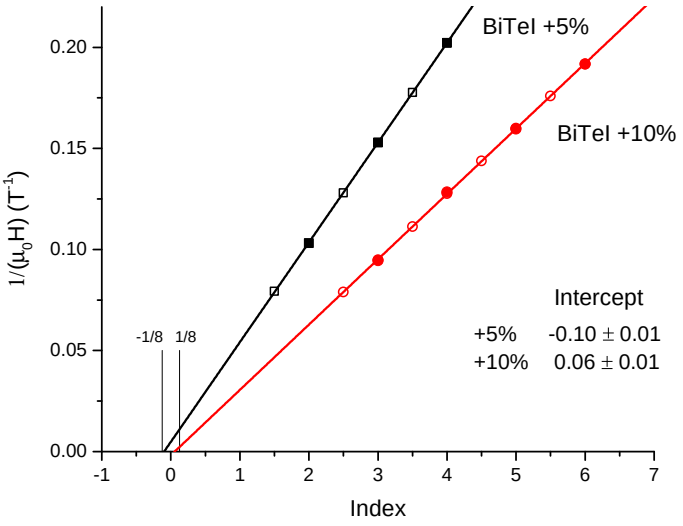

(a) IFS

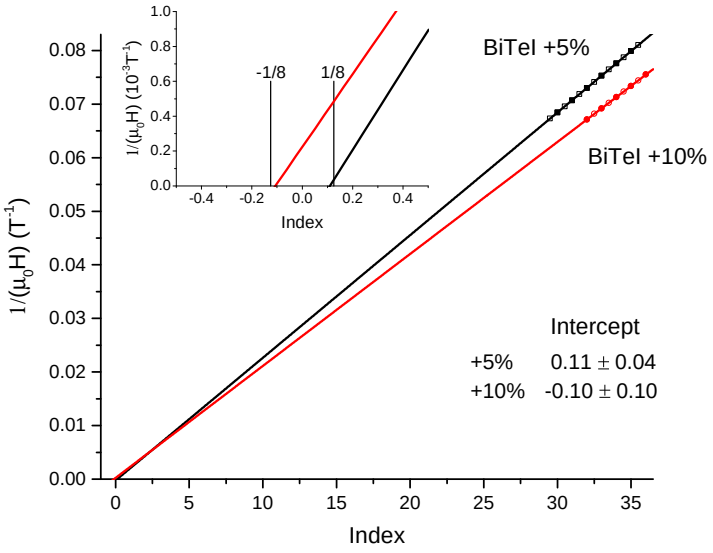

(b) OFS

Figure 4.36: Landau index plots for the (a) IFS and (b) OFS for both BiTeI samples measured at ambient pressure. The filled symbols indicate ρ_{xx} maxima while the open symbols indicate ρ_{xx} minima.

For our samples measured at atmospheric pressures, the Landau level indexing is carried out for both the IFS and the OFS quantum oscillations. As the phase is periodic in 2π, the indices can be shifted by integer amounts such that the intercept is between -0.5 and 0.5. The resulting plots are called fan diagrams and are shown in Figures 4.36a and 4.36b for the IFS and OFS oscillations respectively. The positions for the oscillation maxima are indicated by filled symbols while the positions for the oscillation minima are indicated by open symbols.

For the IFS oscillations, the straight line fits gave frequencies of 20.3 T and 30.6 T for the +5% and +10% sample respectively, consistent with the frequencies obtained from the Fourier transform (20 T and 30 T respectively). Extrapolating the straight line fit down to zero inverse field, the intercept gives a value of γ that is between $-1/8$ and $1/8$, indicating a non-trivial Berry phase associated with the IFS. The value of the intercept and the uncertainty from the fit are labelled on the plot for both samples.

Turning to the OFS oscillations, similar conclusions can also be drawn from the Landau level indexing process and a Berry phase that is between $-1/8$ and $1/8$ can be observed. This result is consistent with our expectations for this material as the band dispersion near the Dirac point caused by the spin-splitting from the Rashba interaction term is linear. For both the IFS and OFS, the Rashba interaction constrains the electron spin to be normal to its momentum, so that a circulating spin texture is formed around the Dirac point. This gives both Fermi surfaces a non-trivial Berry phase.

It is to be noted that the uncertainty associated with γ_{OFS} is much larger than for γ_{IFS} as the lowest integer index occurs at $n = 30$ and a much longer extrapolation is required for the determination of the intercept value. In order to improve the accuracy and reliability of the fit, higher magnetic fields would be required to access the lower Landau levels. This was carried out on the +10% sample under ambient pressure conditions and will be discussed subsequently.

High Pressure Transverse Resistivity

For the high pressure runs carried out in the piston-cylinder cell, the samples were contacted such that the voltage and current leads were diagonally across each other (measuring $R_{24,31} = V_{31}/I_{24}$ using the convention in Figure 4.34) in order to perform a Hall measurement.

Normally, we would expect oscillations in the Hall component to be phase-shifted from the longitudinal component by a factor of $\pi/2$ [24, 25, 32]. This can be observed in Figure 4.37, where the oscillatory behaviour for the various quantities are plotted in the same graph. $\Delta R_{24,31}(+B)$ and $\Delta R_{24,31}(-B)$ denote the background-subtracted signal obtained for the positive and negative field sweep, while ΔR_{xy} is obtained from

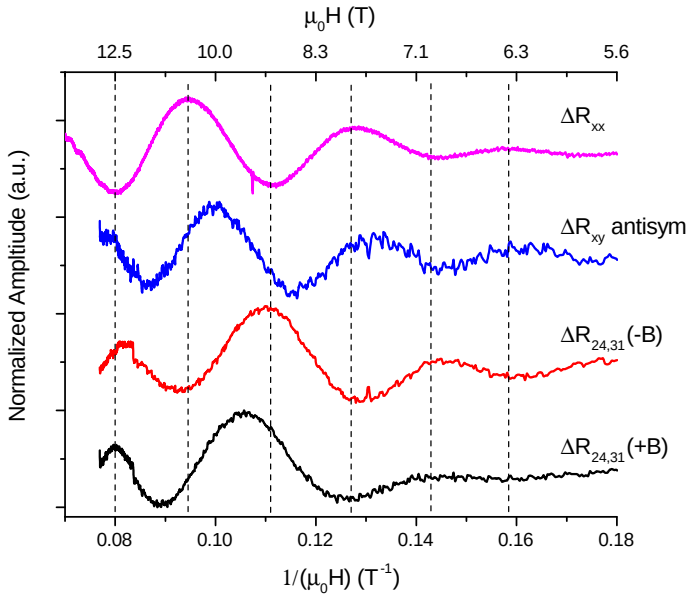

Figure 4.37: IFS oscillatory behaviour of R_{xx}, R_{xy}, $R_{24,31}(-B)$, $R_{24,31}(+B)$ for the 10% sample. $R_{24,31}(+B)$ and $R_{24,31}(-B)$ is the resistivity signal when the field is swept in the positive and negative direction, and R_{xy} is the Hall signal obtained by anti-symmetrising these two quantities. Dashed lines act as a guide to show the positions of the oscillation maxima and minima in R_{xx}.

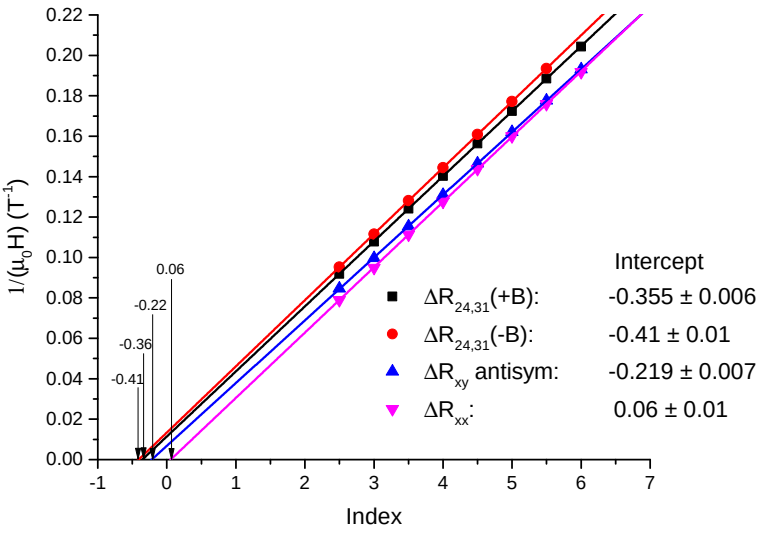

Figure 4.38: Indexing of the oscillation maxima and minima to determine the phase relationship between the measured (R_{xx}, $R_{24,31}(+B)$ and $R_{24,31}(-B)$) and calculated (R_{xy}) components for the 10% sample.

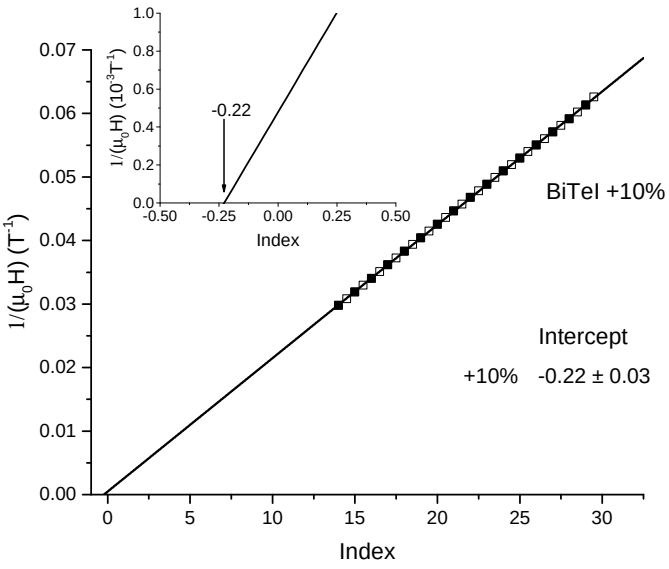

Figure 4.39: Landau level indexing for the high field Hall measurement of the +10% sample. The OFS peak positions of R_{xy} are marked with filled squares while the valley positions are marked with empty squares. The inset shows the extrapolated linear fit as $1/B$ tends to zero, and the intercept value of -0.22.

the anti-symmetrisation of these two quantities. Visually comparing the curves ΔR_{xx} and ΔR_{xy}, oscillations in the Hall component of the resistivity leads the longitudinal component by about $\pi/2$.

A numerical value for the phase difference between the two components can be obtained by curve fitting or by performing indexing on the two curves and taking the difference obtained from the intercept values. As shown in Figure 4.38, the phase difference between R_{xx} and R_{xy} obtained from the latter method is given by $(0.06-(-0.22))\times 2\pi = (0.56 \pm 0.01)\pi \approx \pi/2$.

This phase shift is also evident in the high field Hall measurement of the +10% sample, where the OFS oscillations are very clearly observed at fields up to 34 T. The Landau fan diagram is plotted in Figure 4.39, where we have used the same convention of labelling the maxima with integer indices. The intercept obtained by extrapolating $1/B$ to zero is close to 0.25 – i.e. a phase shift of $\pi/2$.

Using this information and also assuming that the phase relationship between R_{xx} and R_{xy} remains unchanged under pressure, we will apply a phase shift of $\pi/2$ to the phase obtained from our Hall measurements, i.e. labelling of maxima $N \rightarrow N + 0.25$. The fan diagrams of the IFS oscillations for the +5% and +10% sample measured at different pressures are shown as subplots of Figure 4.40. Due to the splitting of the IFS frequency for the +5% sample, two fan diagrams are plotted for the +5% sample. As the frequency of the IFS oscillations are generally quite small (about 20–40 T), Landau

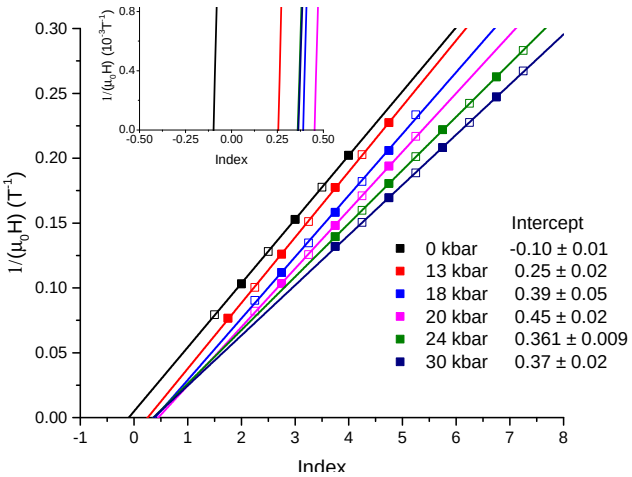

(a) Landau Level indexing of the lower frequency IFS oscillations for the +5% sample.

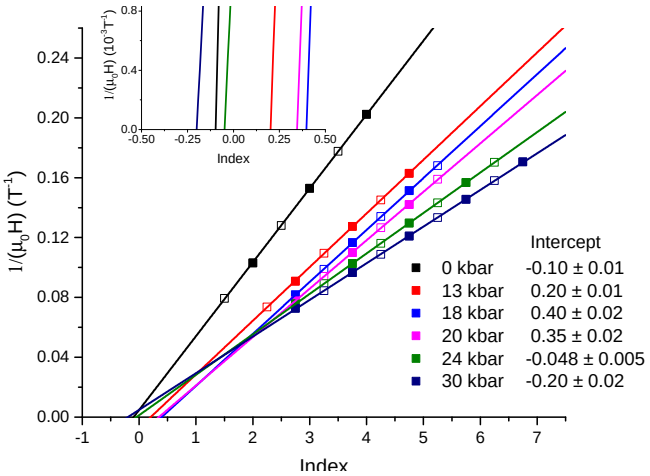

(b) Landau Level indexing of the higher frequency IFS oscillations for the +5% sample.

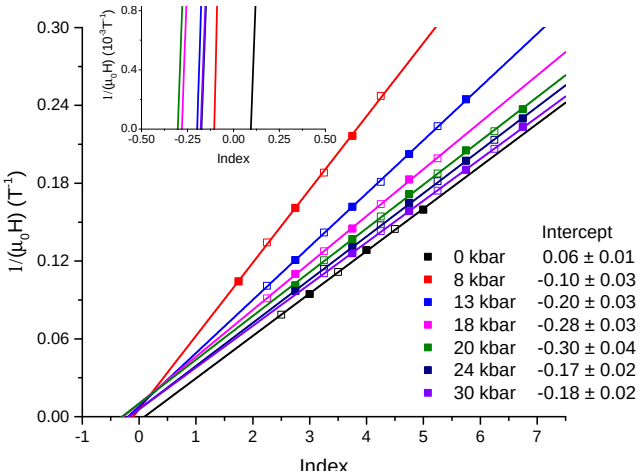

(c) Landau Level indexing of the IFS oscillations for the +10% sample.

Figure 4.40: Fan diagrams of the IFS oscillations for the two BiTeI samples.

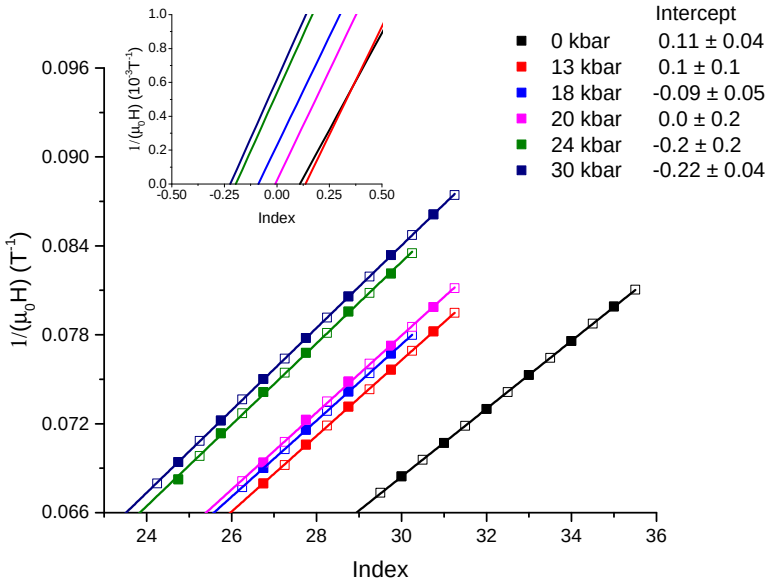

(a) Landau Level indexing of the OFS oscillations for the +5% sample.

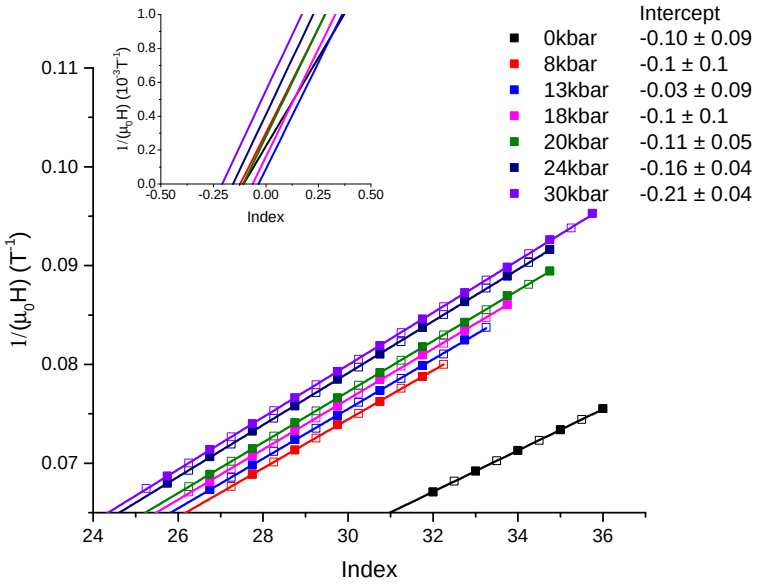

(b) Landau Level indexing of the OFS oscillations for the +10% sample.

Figure 4.41: Fan diagrams of the OFS oscillations for the two BiTeI samples.

levels that are close to the quantum limit can be accessed with our 15 T magnet and the straight line fit need not be extrapolated by much in order to obtain the phase factor γ.

The same procedure is repeated for the OFS oscillations (Figure 4.41) in order to obtain the the OFS phase factor as a function of pressure.

For the IFS index plots, it is observed that the positions of the maxima and minima are well described by a linear fit and that there is no bending in the fan diagram near the quantum limit. This indicates that any deviations from linearity due to effects of the Zeeman coupling term is small.

The phase factors for both the IFS and OFS oscillations are then plotted against pressure in Figures 4.42a and 4.42b respectively. In theory, the sign of the phase factor for the IFS and OFS should be opposite to each other as the two surfaces have spin chiralities opposite to each other. In practice, this is difficult to observe experimentally and the opposite signs for the IFS and OFS phase factors that we observe for our samples is probably a coincidence. Therefore, we will focus on how the magnitude of the phase factor changes as pressure is increased.

Looking at the IFS oscillations for the 5% sample, the phase factor starts off at a value close to zero at ambient pressure, before deviating at higher pressures. It is also observed that the magnitude of the phase factor for the higher and lower frequencies are similar in value for pressures below 20 kbar, before showing marked difference at pressures above 20 kbar. This is also the pressure point where the splitting in oscillation frequency becomes more pronounced in the FFT spectrum (see Figure 4.18). The phase factor for the lower frequency reaches a value that is close to 0.5 while the higher frequency drops to an intermediate value that is closer to 0. This is also observed in the 10% sample, where the phase factor first rises to a maximum (albeit not as high compared to the 5% sample) at about 20 kbar, before dropping to an intermediate value.

For the OFS oscillations, the phase factor for both samples has a value $|\gamma - \delta| \sim 0$ for pressures below 20 kbar. Above 20 kbar, the phase factor takes on an intermediate value of about 0.2.

Our measurements of the phase factor for BiTeI are fairly consistent with work done by Park *et al.* [27]. In their paper, they proposed that the band structure of BiTeI undergoes a transition at a pressure of about 20 kbar, resulting in a change in the shape of the IFS and OFS. This evolution of the inner Fermi surface is shown schematically in Figure 4.43, where the spindle-shaped surface is slowly deformed into a surface that is shaped like a peanut. Although the outer Fermi surface does not have the same spindle-shape as the inner Fermi surface, its behaviour under pressure is essentially the same – starting from a extremal belly cross sectional orbit at ambient pressure to having two extremal orbits, one corresponding to a belly and one to a neck orbit.

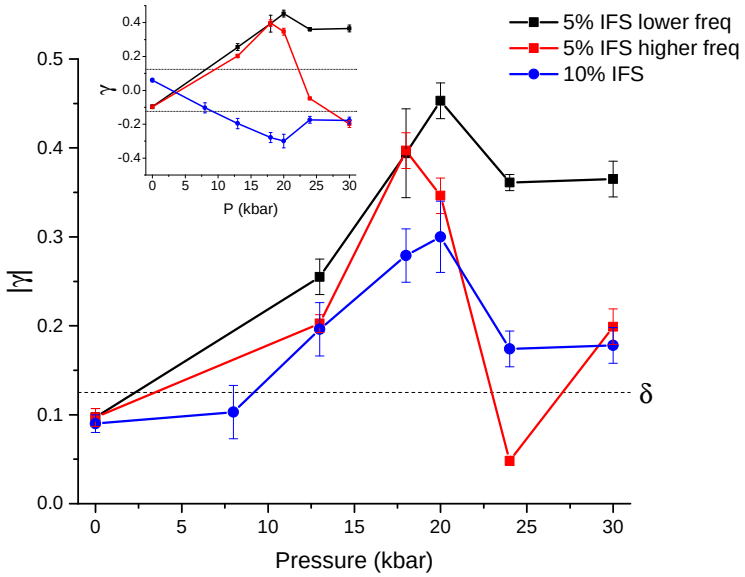

(a) Phase factor for IFS oscillations.

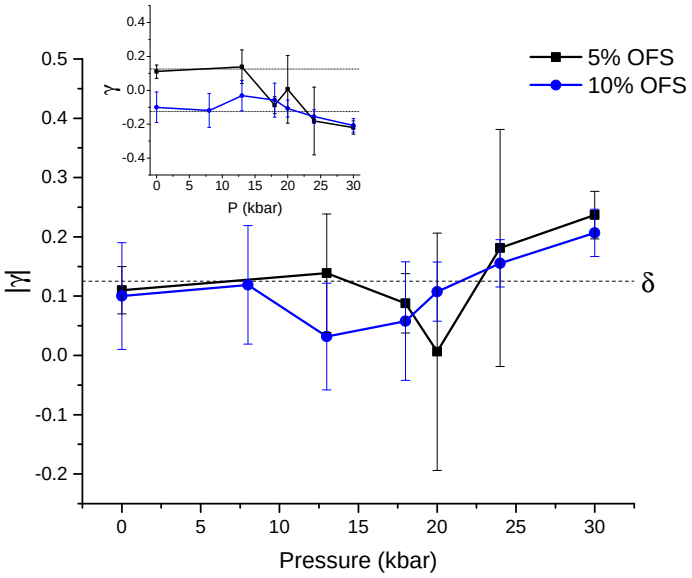

(b) Phase factor for OFS oscillations.

Figure 4.42: Magnitude of the phase factor obtained from the Landau fan diagrams plotted against pressure. Inset shows the raw value of the phase obtained from the fan diagram intercepts.

Even though their model predicts that past the critical pressure, the IFS and OFS should exhibit two frequencies each, Park only observed a frequency each for the IFS and OFS oscillations. They explained that for the OFS, the orbit that has a smaller k_z warping (i.e. the orbit centred about the A point) would give the dominant contribution. Whereas for the IFS, they state that impurity scattering is the dominating effect, and because the A-point experiences a larger inter-site mixing between Te and I atoms, oscillations centred about the A-point would experience more impurity scattering and thus be damped out. As a result, only the neck orbit would be observed for the OFS while the belly orbit would be observed for the IFS past the critical pressure.

For our 5% sample, we managed to observe two frequencies in our measurements; the phase of the smaller frequency showing a much larger deviation from the phase at ambient pressure compared to the phase of the larger frequency. This supports the notion of a change in curvature from a belly-type orbit into a neck-type orbit for the smaller frequency oscillation when the Fermi surface changes into a peanut-like surface. For the larger frequency, the change in phase is less pronounced as the orbit remains belly-type. This trend can also be observed in the 10% sample where only one frequency belonging to the dominant belly orbit is seen.

Furthermore, the splitting of IFS frequencies that was observed in the 5% sample but not in the 10% sample is consistent with the explanation proposed by Park. When more iodine is added into the sample growth process, there would be a higher probability of crystal defects arising due to inter-site mixing between the Te and I atoms when the crystal is grown. Thus, it is likely that the 10% sample experiences more impurity scattering due to these defects compared to the 5% sample, damping out the frequency corresponding to the neck orbit past the critical pressure.

Turning to the phase of the OFS frequencies, although the change in phase with pressure is not as significant compared to the IFS frequencies, we see that for both samples the phase starts to deviate from $|\gamma - \delta| \sim 0$ at pressures above 20 kbar, suggesting that there is a change in curvature in the Fermi surface from belly-type to neck-type. Since the OFS oscillations are far away from the quantum limit ($n \geq 25$), this result would have to be further confirmed under higher magnetic fields.

In conclusion, we have tracked how the the phase factor for the IFS and OFS varies under pressure using our quantum oscillation measurements. At ambient pressure, we obtained a non-trivial π Berry phase for both the IFS and OFS, consistent with expectations for a Rashba system. As pressure is increased, we observed a deviation from the ambient pressure π Berry phase for both 5% and 10% samples. This deviation is more pronounced for the lower IFS frequency of the 5% sample. The changes in the phase factor are explained by a model proposed by Park *et al.* in which the Fermi

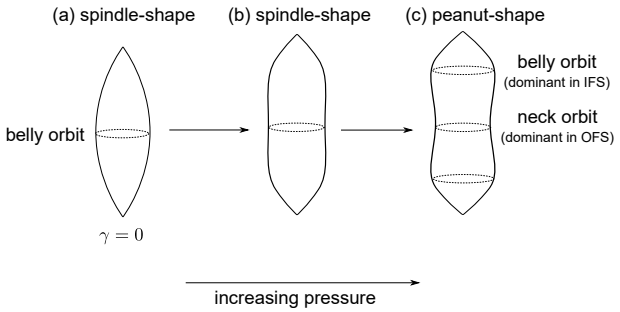

Figure 4.43: Evolution of the Fermi surface of BiTeI under pressure.

surface evolves from a spindle shape to a peanut shape under pressure. Large changes in the phase factor are caused by belly-type orbits changing to a neck-type orbit while belly-type orbits that remain unchanged do not cause a significant deviation.

This pressure work suggests a change in the topology of the Fermi surface (spindle shape to peanut shape), but does not give any strong indication of the emergence of a topological insulating phase that is predicted by Bahramy *et al.* [18]. We believe that insulating samples of BiTeI, where the chemical potential lies in the bandgap, would give useful insight for further investigating this pressure-induced phase transition as the quantum oscillations from the bulk states would not interfere with the signals from the surface state.

Chapter 5

Bi_2Te_3

5.1 Introduction

Compounds in the mineral group called the tetradymites consist mainly of elements bismuth (Bi), tellurium (Te) and sulphur (S), with trace amounts of selenium (Se). In particular, the compound Bi_2Te_3 that we are studying, belongs to this group of minerals. Bismuth telluride has a rhombohedral crystal structure, with a space group of $R\bar{3}m$ [69, 70]. The arrangement of the atoms can be visualised as a stack of layers, where each stack consists of 5 layers of atoms Te(1)-Bi-Te(2)-Bi-Te(1) (also called the quintuple layer). The stacks are repeated along the crystallographic c axis, with each adjacent stack being held together by van der Waals interactions (see Figure 5.1).

As mentioned previously in Section 3.4, powder X-ray diffraction measurements of our sample yielded hexagonal lattice parameters of $a = 4.39$ Å and $c = 30.5$ Å, consistent with values reported in previous studies [69, 70, 41].

Even before the prediction and discovery that Bi_2Te_3 is a topological insulator, extensive research has been previously conducted on this material due to its superior thermoelectric properties (good electrical conductivity, poor thermal conductivity, large Seebeck coefficient) making it a promising candidate for thermoelectric device applications [71, 72, 73]. The band structure and Fermi surface for Bi_2Te_3 have been studied both experimentally using SdH methods [74, 75, 71] and optical measurements [76], as well as through numerical computations [69, 77, 78].

Initially, there was disagreement between experimental results and theoretical calculations as theoretical work predicted six valence band maxima and two conduction band minima [69] while experiments indicate that there should be six extrema in both valence and conduction bands. This was only clarified when spin-orbit interactions were properly included into calculations [77, 78], that there are indeed six extrema in both valence and conduction bands of Bi_2Te_3.

Not long after spin-orbit interactions were shown to be crucial for understanding the band structure of Bi_2Te_3 , Zhang *et al.* [10] ran electronic band structure calculations on the layered compounds Bi_2Se_3, Bi_2Te_3, Sb_2Te_3 and Sb_2Se_3, and showed that spin-orbit

interactions resulted in band inversion in all except Sb_2Se_3, thus predicting the topological insulating behaviour in these materials. At the experimental forefront, ARPES work was carried out by Chen *et al.* [12] to probe the bulk and surface states of Bi_2Te_3. They report the existence of a single Dirac cone in the Brillouin zone of Bi_2Te_3, confirming that the material is indeed a 3D topological insulator. The ARPES measurements of the conduction and valence band dispersions along high symmetry directions of the surface Brillouin zone are reproduced in Figure 5.2 for comparison against our experimental results later.

Subsequent transport measurements carried out by Qu *et al.* [25] further corroborated the ARPES findings. Performing SdH measurements on several samples of Bi_2Te_3, they saw one low frequency oscillation in each sample, ranging from $\sim$ 20–40 T. From the rotation studies, they found that non-metallic samples have oscillation frequencies that follow a $1/\cos(\theta)$ dependence, characteristic of a 2D Fermi surface; while oscillations observed in metallic samples deviate from such a behaviour. They concluded that the oscillations observed in the non-metallic samples originate from a 2D surface state. Furthermore, an anomaly observed in the low field Hall conductance can be well explained using a two-band model in which the surface and bulk states contribute in parallel.

Growing Bi_2Te_3 crystals with bulk insulating properties has proved challenging, most likely due to antisite defects occurring in the crystal structure. Although samples of Bi_2Te_3 grown under a compositional gradient can show non-metallic behaviour, resistivity remained low ($< 0.01\,\Omega$ cm at liquid helium temperatures) [25] and bulk effects usually mask or interfere with surface transport studies. As a result, researchers have set out to find ways of tuning the Fermi level in order to make the samples less metallic and found that by substituting one of the Te atoms with Se, single crystals of Bi_2Te_2Se with high bulk resistivity values ($> 1\,\Omega$ cm) at low temperatures could be obtained. Moreover, quantum oscillation experiments carried out by Ren *et al.* [24] and Xiong *et al.* [32] demonstrated that just like the sister compounds Bi_2Te_3 and Bi_2Se_3, Bi_2Te_2Se is also a TI material, making it an ideal material for studying the surface quantum transport in TIs by suppressing contributions from the bulk.

High pressure studies on Bi_2Te_3 have been carried out prior to the discovery that it is a TI material. Sologub *et al.* [79] and Brandt *et al.* [80] both investigated the pressure dependence of the SdH effect on Bi_2Te_3 up to 12 kbar, with the former studying n- and p-type samples and the latter studying p-type and p-type doped (with Ge or In) samples. For the p-type samples, Sologub *et al.* [79] reported two quantum oscillation frequencies (magnetic field parallel to the trigonal axis) and observed that the lower-frequency oscillation increases with pressure while the higher-frequency oscillation decreases with

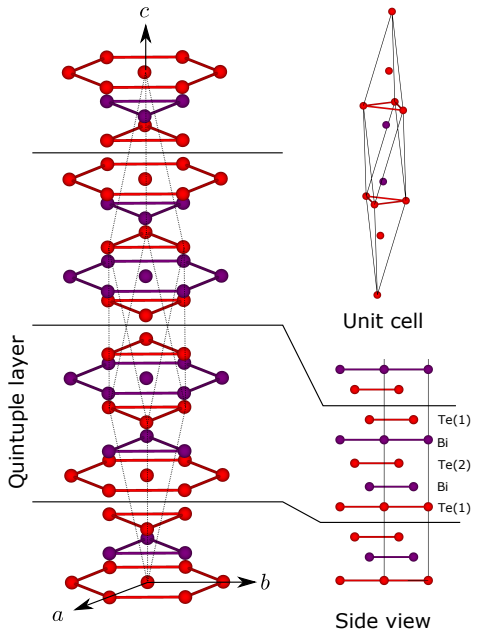

Figure 5.1: Crystal structure for Bi_2Te_3, generated using VESTA. The rhombohedral unit cell is shown in dotted lines.

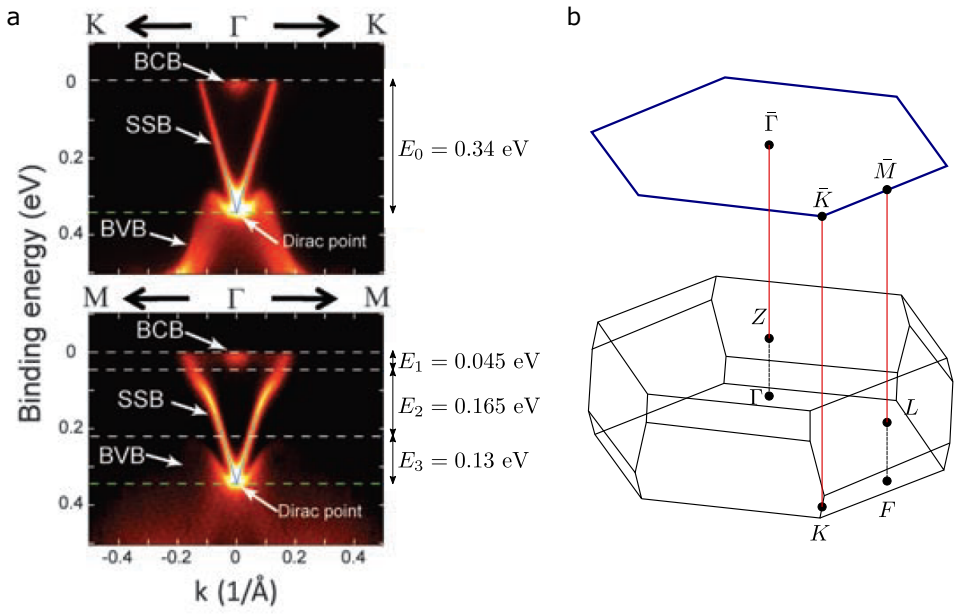

Figure 5.2: (a) ARPES measurements of the band dispersion carried out at at 15 K, along K–Γ–K (top) and M–Γ–M (bottom) directions, reproduced with permission from [12]. Labels for the energies are as follows: E_0 – binding energy of the Dirac point; E_1 – bulk conduction band binding energy; E_2 – bulk energy gap; E_3 – energy separation between the Dirac point and top of bulk valence band. (b) Three dimensional Brillouin zone for Bi_2Te_3 with the points of high symmetry labelled. The blue hexagon is the 2D projection onto the (1,1,1) surface.

pressure. Both groups attributed this phenomenon as an outflow of hole carriers from the principal valley to a lower hole band. For the n-type samples, only one frequency that increased with pressure ($\sim$ 35–42 T) was observed. In the late 1990s, Itskevich *et al.* [81] performed thermoelectric measurements of Bi_2Te_3 up to a pressure of 2.5 GPa. Observations of anomalies in their thermoelectric data led them to propose the existence of a electronic topological transition (ETT) occurring in Bi_2Te_3 .

An ETT is a change in the topology of the Fermi surface with no volume discontinuity nor change in the positions of the atoms in the crystal structure. This phenomenon was first noticed by Lifshitz [82] and is also known as a Lifshitz transition. The changes in the Fermi surface can be classified into two types: the first being the collapse of a 'neck' region of the Fermi surface, and the second type being the appearance or disappearance of a split-off region of the Fermi surface (see Figure 5.3). Such a transition can be approached continuously by using external tuning parameters like temperature, magnetic field, or in particular hydrostatic pressure.

In the vicinity of such transitions, the electron density of states is singular (non-smooth) which leads to anomalies in thermodynamic, transport and elastic properties of materials [82, 83]. Similar to critical points in conventional phase transitions, the ETT can be characterised in terms of critical exponents of a parameter $\zeta = E_F - E_F^c$, which is the Fermi level E_F measured from the critical point value E_F^c. The behaviour of ζ for 2D and 3D materials is summarised in Table 1 of [84]. Although TIs and ETTs share the same word 'topological', they are describing fundamentally different phenomena and the ETT proposed in Bi_2Te_3 is not necessarily related to the fact that Bi_2Te_3 is a 3D topological insulator material.

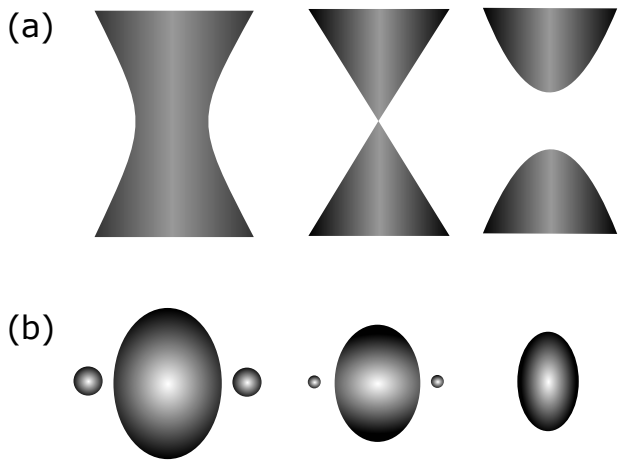

Figure 5.3: Schematic showing the two different types of topological change of Fermi surface (Figure adapted from [84]). (a) Collapse of a 'neck' of the Fermi surface. (b) Appearance or disappearance of a split-off region of the Fermi surface.

Further pressure work on the bismuth tetradymite materials only came about after the prediction and discovery of TI materials more than a decade later. Numerous high pressure studies have been conducted in order to map out the different phases of Bi_2Te_3. Nakayama *et al.* [85] performed powder X-ray diffraction studies to study the structural change in Bi_2Te_3 under high pressure up to 16.6 GPa. They observed two structural phase transitions at room temperature occurring at 8 GPa and 14 GPa. They also observed a minimum in the ratio c/a at 2 GPa, and attributed this as a sign of the ETT since there was no change in the material structure. The pressure range was extended up to 31 GPa by Polian *et al.* [86]. Signature of an ETT was observed when analysis of the Eulerian strain derived from X-ray data showed a kink at 3.2 GPa.

Room temperature transport properties of materials in the series Bi_2Te_3 -Sb_2Te_3 were studied by Jacobsen *et al.* [87] up to 10 GPa. A distinct kink observed in the resistivity and Seebeck coefficient measurements at around 8 GPa is consistent with the structural transition reported by other groups. In addition, they observed a slight change in slope in the electronic and thermal conductivity data at about 3 GPa. A more prominent feature was a shoulder in the Seebeck coefficient at the same pressure, possibly indicating the onset of the ETT. Zhang *et al.* [88] performed Hall effect and resistivity measurements of Bi_2Te_3, at temperatures between 300–420 K, up to a pressure of 28 GPa. They reported abnormal inflection points in their Hall and resistivity measurements occurring at 4, 8, 12, and 18 GPa, of which three of them (8, 12 and 18 GPa) are attributed to structural transitions while the 4 GPa anomaly is attributed to an ETT.

Manjón *et al.* [89] proposed that the ETT observed in Bi_2Te_3 is driven by the change in van der Waals forces between each stack in the layered material as pressure is increased. Near the critical pressure, band extrema associated with a Van Hove singularity in the electronic density of states crosses the Fermi level, leading to a strong redistribution of density of states near the Fermi level. This redistribution of density of states causes anomalies and discontinuous changes in electrical transport behaviour.

A comprehensive study of the evolution of the crystal structure, low temperature resistivity and Hall coefficient of Bi_2Te_3 with pressure was carried out by Zhang *et al.* [90]. They confirmed that Bi_2Te_3 undergoes several structural transitions from $R\bar{3}m$ (Phase I) to: (i) a mixture of $R\bar{3}m$ and C2/m (HP I) at 8 GPa, (ii) mixture of C2/m and C2/c (HP II) at 13 GPa, and (iii) Im-3m (HP III) at 16 GPa. Superconductivity was initially observed at 3.2 GPa with a T_c of 3 K. High pressure phases also showed superconductivity with the highest T_c of ~ 7 K observed in the pressure region corresponding to HP I and HP II. The authors made no mention of the ETT in Bi_2Te_3 .

Our work is to investigate how the transport properties of the TI material Bi_2Te_3 varies under pressure and probe the ETT using SdH oscillations.

5.2 Sample Preparation and Resistivity Characterization

The Bi_2Te_3 samples used for these measurements were grown using the chemical vapour transport method. Similar to the BiTeI samples, thin flakes of these samples could be easily obtained through exfoliation using scotch tape. Gold wire contacts were spot-welded onto them and conductive silver epoxy was used to provide extra mechanical support. The dimensions for the sample are estimated to be $394 \times 385 \times 10$ μm^3 (± 1 μm) from Figure 5.4.

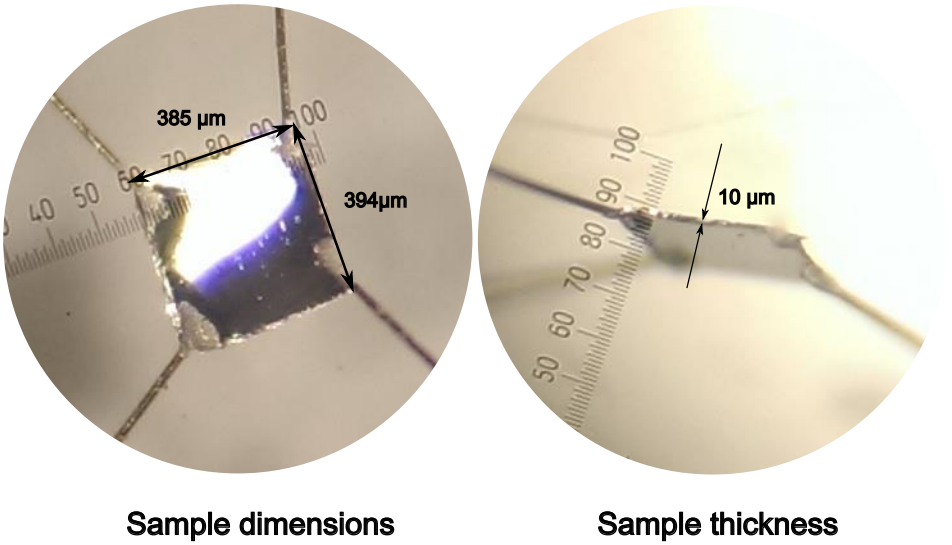

Figure 5.4: Left: Bi_2Te_3 sample with spot-welded gold wire contacts, strengthened with silver epoxy. Right: Sideways photograph for measuring thickness of sample.

Like the BiTeI samples, we find that the Bi_2Te_3 samples are metallic in nature from the measurements of the resistivity as well as the Hall effect. Down to a temperature of 4 K, the resistance of Bi_2Te_3 decreases with temperature, and a RRR value of 5.9 is obtained for the sample (Figure 5.5). For our square-like samples, the van der Pauw method was used to measure the resistivity. Comparing the size of the contacts against the dimensions of the sample, we estimate the fractional uncertainty associated with this technique to be 4%. The measured values for R_{vert} and R_{hor}, and the computed values for R_s and ρ_{xx} using equation 4.16 are shown in Table 5.1.

Hall measurements of the sample are carried out by sweeping the magnetic field from 13 T to -13 T, as shown in Figure 5.6. Since the sign of the slope is negative, Hall measurements indicate that the carriers in this material are predominantly n-type, similar to the BiTeI measurements. However, unlike the BiTeI samples, the Hall resistivity

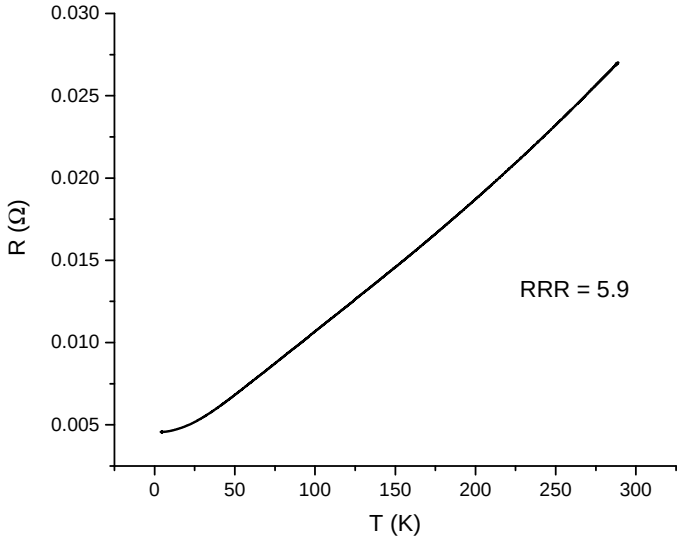

Figure 5.5: Metallic behaviour was observed in the resistance of the Bi_2Te_3 sample against temperature. The sample has a RRR value of 5.9.

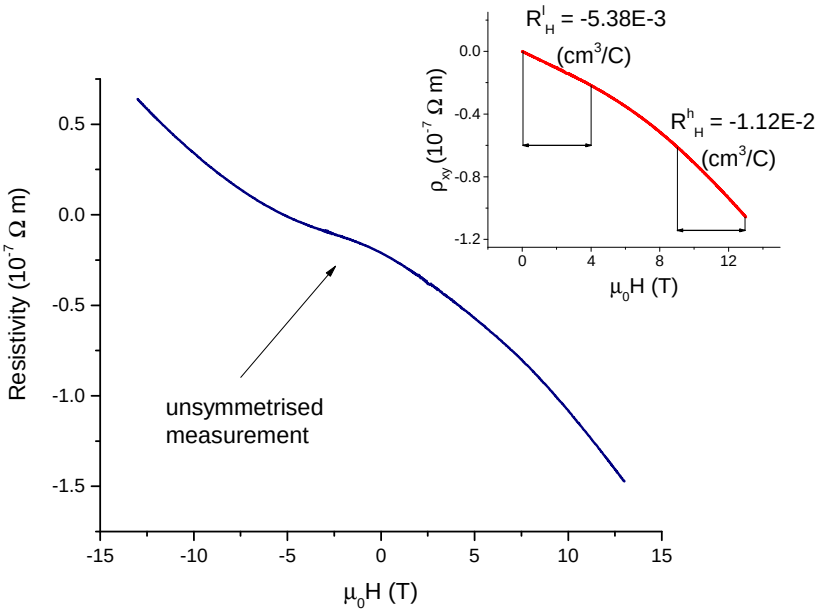

Figure 5.6: Ambient pressure hall effect measurement. Inset: Anti-symmetrised transverse resistivity ρ_{xy}. The transverse component shows a deviation from linearity.

showed a deviation from linear behaviour, even after anti-symmetrisation of the data (see inset). Performing a linear fit on the low field (0–4 T) and on the high field region (9–13 T), two values of the Hall coefficient are obtained: $R_H^l = -5.38 \times 10^{-3}\,\mathrm{cm}^3/C$ and $R_H^h = -1.12 \times 10^{-2}\,\mathrm{cm}^3/C$ for the low and high field regions respectively.

Since the Hall coefficient is inversely proportional to carrier concentration, an increase in the absolute value of the Hall coefficient implies a decrease in the carrier concentration, from $n^l = 1.2 \times 10^{21}\,\mathrm{cm}^3$ to $n^h = 5.6 \times 10^{20}\,\mathrm{cm}^3$. This non-linear behaviour was also seen in the samples Q1 and N1 in the work done by Qu *et al.* [25] (supplementary information Figure S5). We will return to this dataset after results from the quantum oscillation measurements are presented and attempt to model this non-linearity using the two-band model with model parameters inferred from the quantum oscillation study.

Sample	$R_{hor}(\Omega)$	$R_{vert}(\Omega)$	$R_s(\Omega)$	$\rho_{xx}(\Omega m)$	$\rho_{xy}(\Omega m)$	ρ_{xy}/ρ_{xx}
Bi_2Te_3 (CVT grown)	0.00250	0.00454	0.0155(6)	$1.6(2) \times 10^{-7}$	$1.1(1) \times 10^{-7}$ (13 T)	0.7(1)
Chen *et al.* [12] (0% Sn doped)	-	-	-	1.8×10^{-7}	1.4×10^{-6} (13 T)	7.8
Qu *et al.* [25] (N1 sample)	-	-	-	8.0×10^{-7}	8.0×10^{-6} (13 T)	10

Table 5.1: Longitudinal resistivity obtained from van der Pauw technique. Resistivity values of our sample are compared against Chen's (0% Sn doped) sample [12] and Qu's (N1) sample [25].

5.3 Quantum Oscillation Measurements

5.3.1 15T System and Tallahassee Results

Ambient pressure quantum oscillations measurements for Bi_2Te_3 were carried out in three different systems: first using the 15T system, the dilution refrigerator, and at the high field facility in Tallahassee. Unlike the BiTeI samples, the Bi_2Te_3 sample did not show clear quantum oscillations that could be easily identified within the field range provided by the 15T system and we had to use stronger fields to ascertain the existence of the quantum oscillations.

Plotted in Figure 5.7 are two sets of quantum oscillation data of the same sample, one measured at Tallahassee (top) and one measured using the 15T system (bottom). The oscillation data is obtained after performing a polynomial background subtraction from the signal. By sweeping the magnetic field to 15 T, a plausible low frequency oscillation can be seen appearing at fields larger than 8 T. A temperature study of the quantum oscillation amplitude is carried out and the fit gives a light effective mass of

about 0.16 m_e (inset). This measurement was repeated with higher fields at Tallahassee in order to clarify the existence of the oscillation frequency as well as to search for other possible frequencies. By overlaying the two signals on each other, the positions of the extrema on both sets of data match fairly well.

Performing a Fourier analysis on both sets of data, a single peak at 39 T was seen in the FFT spectrum for the 15T system measurement while three peaks were seen in the high field measurement (Figure 5.8). The first peak observed at $\sim$12 T is believed to be an artefact from background subtraction (as the position of the peak shifts drastically depending on the orders of polynomial subtraction used), whereas the 41 T peak is more robust to background subtraction. The third peak that is observed at 338 T is due to a higher frequency oscillation that can be seen at fields above 16 T.

By differentiating the signal with respect to field in Figure 5.9a, the two frequencies observed in the Tallahassee measurement become more prominent, and fits using the LK formula give frequencies of 40 T and 332 T. A slower field sweep from 19–34.5 T at 0.7 T/min, plotted in Figure 5.9b, gives a refined value of the higher frequency to be 337 T.

The Dingle reduction factor can be obtained by fitting the amplitude of the quantum oscillations to an exponential decay envelope function. This is shown in Figure 5.10 for each of the two frequencies observed in the Tallahassee measurement. The red lines represent the fitted curves while the dashed navy lines plot the Dingle reduction envelope function. This function is proportional to $\exp(-B_D/B)$, where B_D is the Dingle factor that is related to the mean free path l from equation 2.34 by $B_D = \frac{\hbar}{2e}\frac{C_F}{l}$. Substituting the relevant numbers, the mean free paths are 29 and 21 nm for the 40 and 337 T frequencies respectively.

5.3.2 Dilution Refrigerator Results

Experiments conducted on the 16 T dilution refrigerator also support the findings from runs conducted using the 15T system and in Tallahassee. The Bi_2Te_3 sample measured here was cleaved from the same crystal growth batch used in the previous experiments, and was prepared in the bar-shaped geometry for measuring longitudinal resistance as shown in Figure 5.11.

For this particular run, the magnetic field was swept from 4–16 T at a base temperature of 47 mK. Two quantum oscillation frequencies can be discerned from the measurement; a lower frequency at 52 T and a higher frequency at 322 T.

After performing a background subtraction on the data, the low frequency quantum oscillation is plotted against inverse field as shown in Figure 5.12. A band-pass FFT filter centred at 52 T is used to filter out high frequencies and the resultant signal is

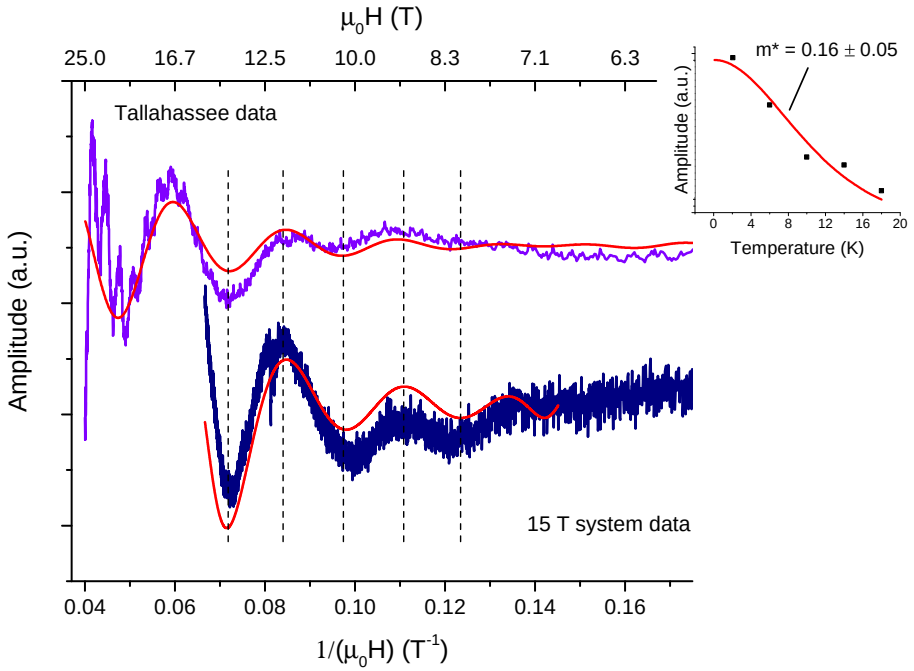

Figure 5.7: Ambient pressure quantum oscillation measurements of Bi_2Te_3 measured at Tallahassee (top) and using the 15T system (bottom). Dashed lines serve as a guide to indicate the positions of oscillation extrema. Red lines are the FFT filtered signals for both sets of measurements. Inset: Temperature dependence of the quantum oscillation amplitude measured using the 15T system.

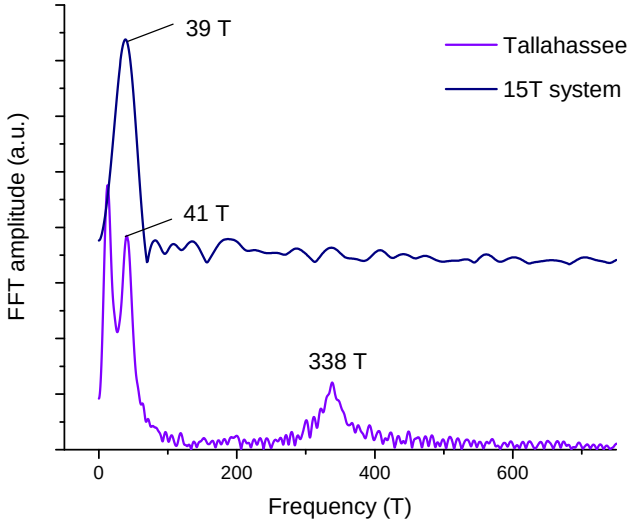

Figure 5.8: FFT spectra for both sets of measurements. Good agreement between the FFT peaks of 39 T and 41 T, corresponding to measurements done on 15T system and at Tallahassee respectively.

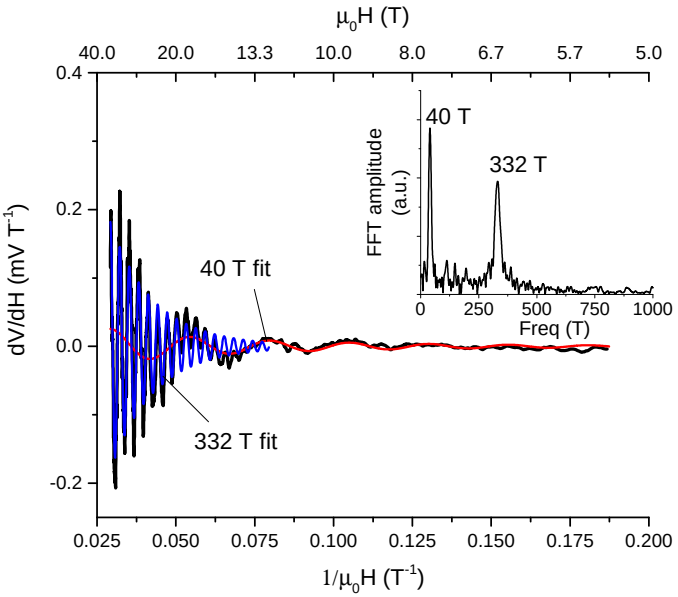

(a)

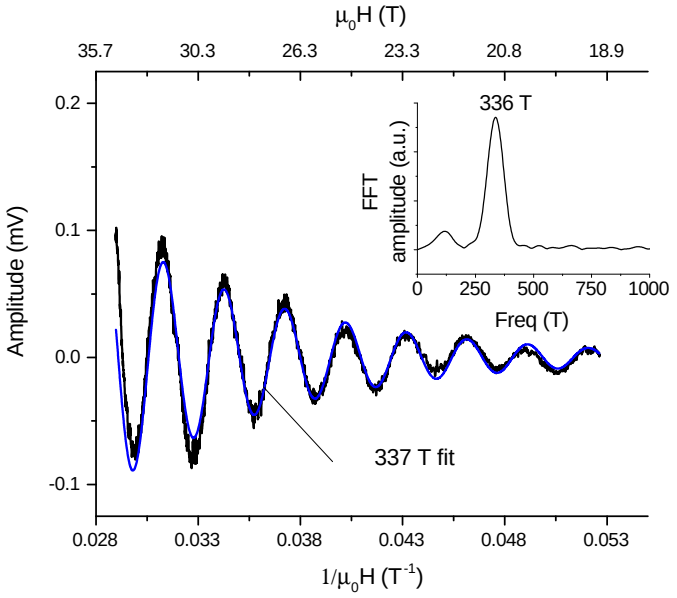

(b)

Figure 5.9: (a) High field measurements of the same sample with the red and blue curves belonging to the 40 T and 332 T frequency LK fits respectively. Inset: The two peaks can be clearly seen in the FFT spectrum. (b) Slower field sweep from 19–34.5 T after a fourth order polynomial background subtraction. Frequency obtained from fitting is 337 T (blue curve).

plotted in red. Temperature dependence of the quantum oscillation amplitude is also carried out, with the fit giving an effective mass of 0.17 m_e, in agreement with the measurements done on the 15T system.

A higher frequency oscillation appears at fields above $\sim$ 12.5 T, and by restricting the

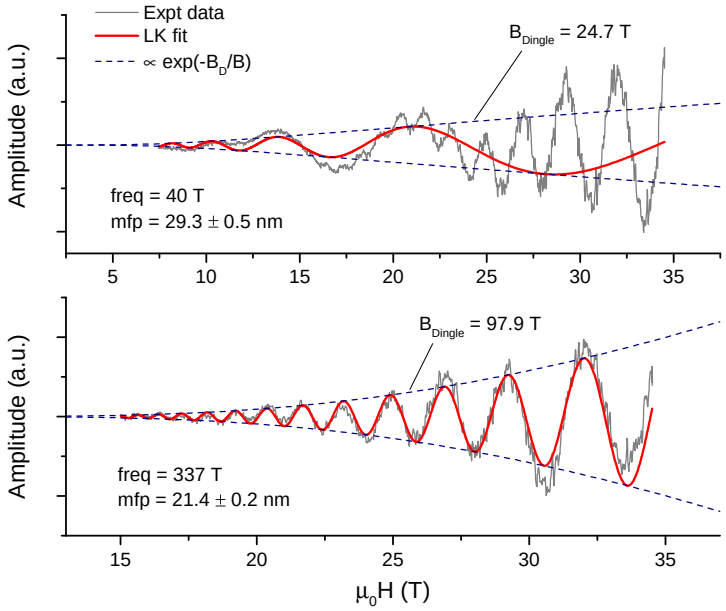

Figure 5.10: Dingle factor analysis. The red curve is the fit to the full LK equation, the dashed navy lines is the envelope function proportional to $\exp(-B_D/B)$. The calculated mean free paths are 29 and 21 nm for the 40 and 337 T frequencies respectively.

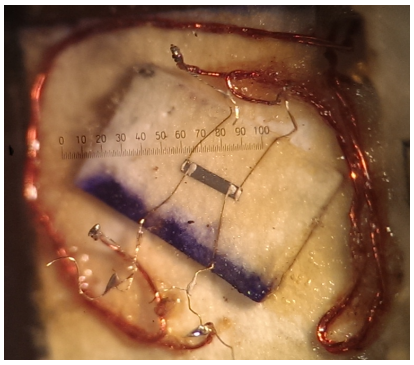

Figure 5.11: Bi_2Te_3 sample mounted on the rotation stage for resistivity measurements.

magnetic field window from 11–16 T, the higher frequency can be more clearly observed (Figure 5.13). From the FFT analysis, the frequency of this oscillation is 322 T, with an effective mass of 0.24 m_e.

The frequencies obtained for this sample are in good agreement with our previous measurements carried out in Tallahassee and on the 15T system, and the slight differences in frequencies might be due to shifts in the chemical potential of the samples that arise from crystal inhomogeneity.

From previous SdH experiments conducted by Qu *et al.* [25], they only reported one quantum oscillation frequency ($\sim$ 20–40 T) for Bi_2Te_3 . This is understandably so, as three of their samples Q1, Q2, Q3 have very low carrier densities with E_F lying in the band gap, thus the only observed quantum oscillation frequency would correspond to

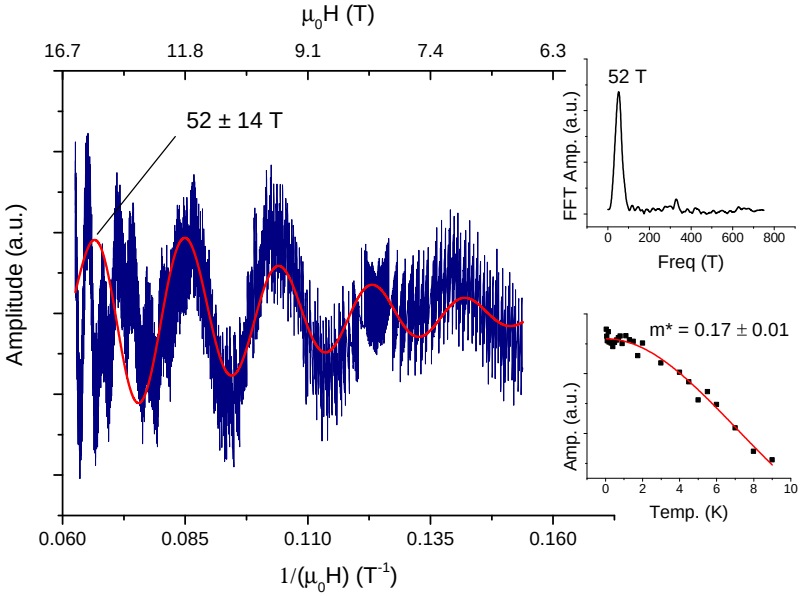

Figure 5.12: Quantum oscillations corresponding to a frequency of 52 T, as shown by the peak in the FFT spectrum (top inset) and the FFT filtered signal (plotted in red) centered about this peak. The cyclotron mass obtained for this frequency is 0.17 m_e (bottom inset).

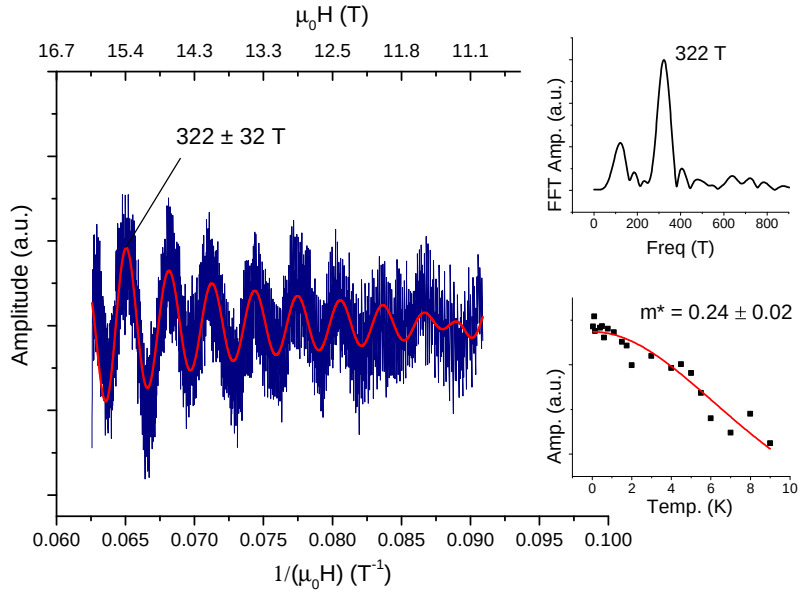

Figure 5.13: Narrower field range showing the higher frequency quantum oscillations. Band-pass filtered (centered about the 322 T peak in the FFT spectrum) signal is plotted in red. Top inset: FFT spectrum showing the peak at 322 T. Bottom inset: Cyclotron mass obtained for this frequency is 0.24 m_e.

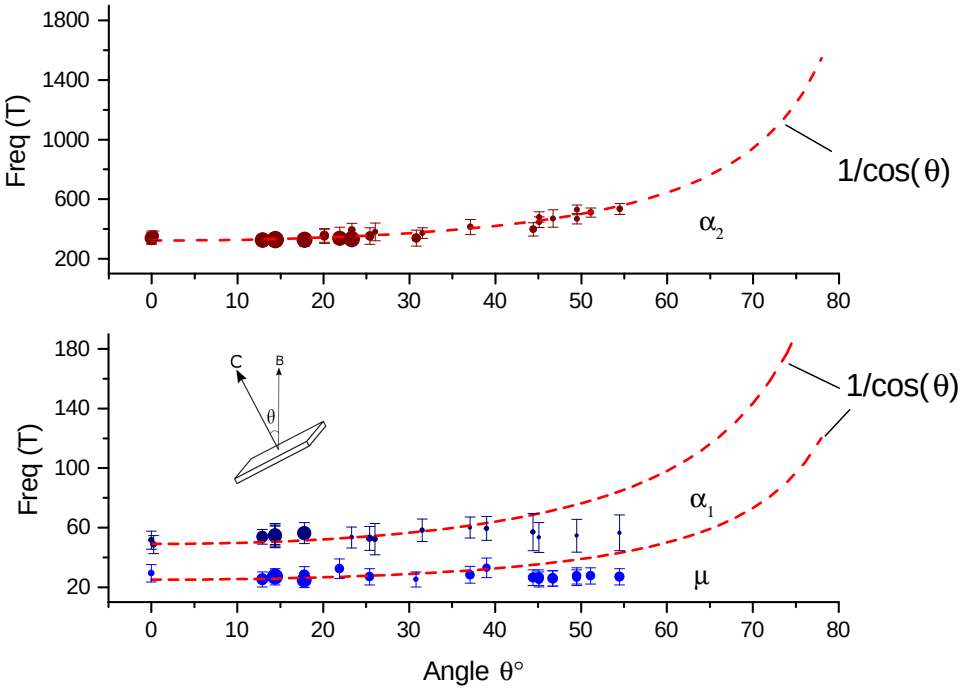

Figure 5.14: Angular dependence of the higher frequency oscillation labelled α_2 (top) and lower frequency oscillations labelled α_1, μ (bottom). The size of the data point is proportional to the FFT peak amplitude. For 2D Fermi surfaces, the angular dependence of the frequency varies with $1/\cos(\theta)$, shown by the dashed red line.

that of the topological surface state. However, they too only observed one frequency for their metallic sample N1 (23 T) and from their analysis, they attributed that to a Fermi surface belonging to a bulk conduction band state, whereas our measurements show that there are at least two frequencies for our metallic Bi_2Te_3 sample. In order to probe the nature of these frequencies for our sample, we performed a rotation study to investigate the angular dependence of the frequencies with respect to field.

Plotted in Figure 5.14 is the angular dependence of the SdH frequencies. The angle θ is defined as the angle the magnetic field makes with the normal of the sample stage (schematic shown in inset). For our experimental setup, the c axis of the sample is parallel to the field at $\theta = 0°$. The size of the frequency data point is directly proportional to the FFT peak amplitude and is normalised against the other data points within the same plot. For this particular rotation study, the highest angle reached was about 55°.

Measurements done between 0–25° gave the best quantum oscillation signals and frequencies with clear peaks in the FFT spectrum can be reliably extracted (larger data point). Possibly due to mechanical vibrations of the rotation mechanism at certain angles, measurements started becoming noisy at angles larger than 25°, giving rise to greater uncertainty in determining the frequency for the oscillation (smaller data point). The low frequency oscillation μ is believed to be some sort of background signal

as it disappears with high enough polynomial background subtraction. A 7th order polynomial fitting was chosen as a compromise to minimise the addition of artefacts into the signal due to over-fitting, but allowing this frequency to remain in the FFT spectrum as a result.

For a 2D Fermi surface, oscillation frequency depends only on the magnetic field component perpendicular to the sample, or in other words, oscillation frequency varies as $1/\cos\theta$. This $1/\cos\theta$ dependence is plotted as a red dashed line and the angular dependence of α_2 seems to suggest that the Fermi surface is of a 2D nature while the lower frequency α_1 appears to be independent of rotation angle, suggesting an isotropic 3D Fermi surface. This result is checked against the phase analysis from Landau level indexing in the following section.

5.3.3 Phase Analysis

From our Hall and longitudinal resistivity measurements as summarised in Table 5.1, our Bi_2Te_3 sample has comparable ρ_{xy} and ρ_{xx}. Using equation 2.48 to construct σ_{xx}, we were not able to resolve quantum oscillations in the conductivity, thus we were unable to perform indexing on the σ_{xx} data.

However, if we were to arbitrarily choose a labelling convention (e.g. labelling maxima as integers) and apply it to both frequencies, we can look at the phase difference obtained for the two frequencies to see if there is a π-shift. If such a π-shift is observed, we would be able to conclude that at least one of the Fermi surfaces has Dirac fermions resulting in a non-trivial Berry phase in the quantum oscillations.

The Landau fan diagrams for the lower and higher frequency are plotted in Figures 5.15a and 5.15b respectively. We adopt the convention of labelling the quantum oscillation maxima with integer values (filled squares) and half-integer values for the minima (empty squares) for *both* sets of frequencies. A straight line is used to fit each set of data and it is extrapolated to zero inverse field to obtain the intercept value. A magnified view of the intercepts is shown in the inset for both plots.

Within each Landau level plot, the values for the intercepts are consistent with each other even though the measurements were conducted on different samples of Bi_2Te_3. For the low-frequency oscillations, the intercepts obtained are close to the value 0.5, while the intercepts obtained for the higher-frequency oscillations are approximately 0. This corresponds to a phase difference of π between the oscillations, suggesting that one of the Fermi surfaces has a non-trivial Berry phase associated with it.

Although the transverse and longitudinal components of resistivity are comparable for our sample (see Table 5.1), if we follow the widely adopted convention $\Delta\sigma_{xx} \sim \Delta\rho_{xx} \sim \cos 2\pi(F/B+\gamma)$ [23, 91, 24] that is used for analyzing SdH oscillations observed

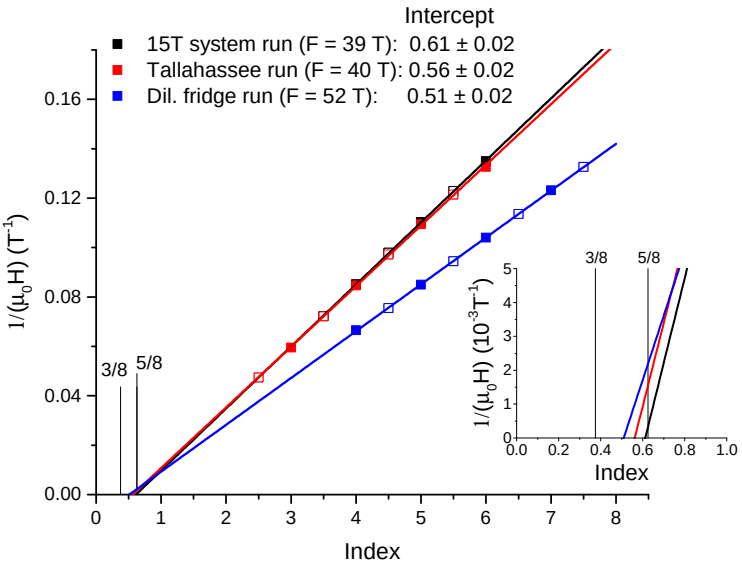

(a)

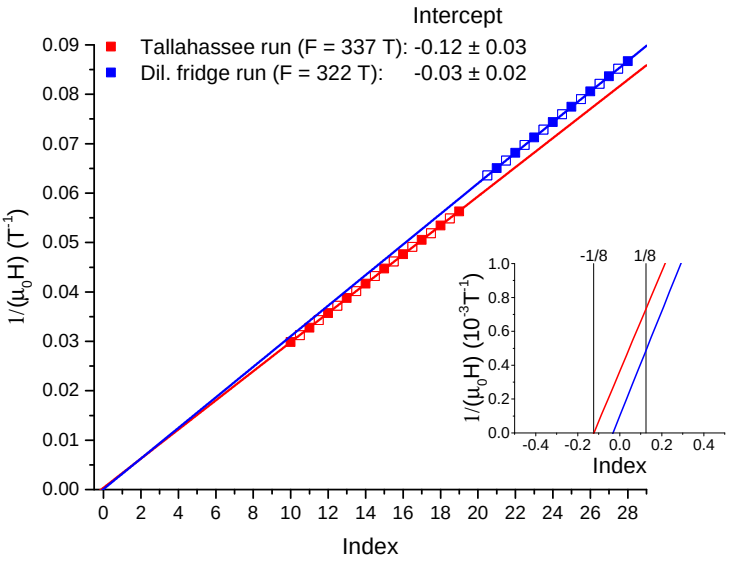

(b)

Figure 5.15: Landau level index plots for the (a) low frequency oscillations α_1 and (b) high frequency oscillations α_2. Filled squares correspond to oscillation maxima while empty squares correspond to oscillation minima. For the low frequency oscillations, the intercept obtained is ~ 0.5 whereas for the high frequency oscillations, the intercept obtained is ~ 0.

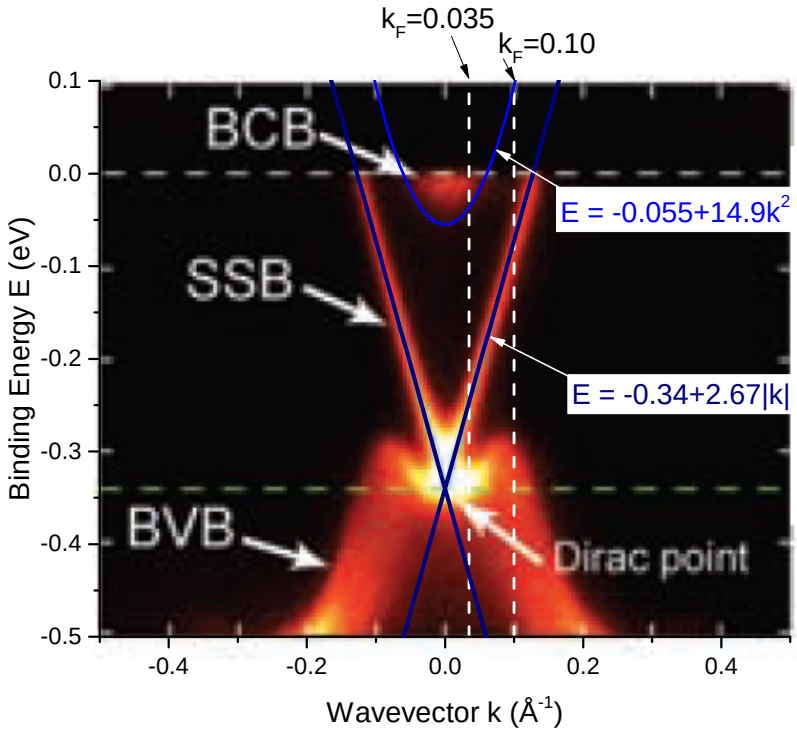

Figure 5.16: Band dispersion of Bi_2Te_3 reproduced from ARPES measurements carried out at at 15 K [12]. Equations describing the band dispersions for the surface state band and the bottom conduction band are plotted in navy and blue respectively. White dotted lines indicate the wavevector corresponding to the SdH oscillation frequencies observed in our experiments.

in the family of 3D topological insulators that contains bismuth, we can apply the results from equation 4.18 to obtain a value of $\gamma = 0\,(0.5)$ for the higher (lower) frequency. This indicates that the higher frequency oscillation has a Berry phase associated with it while the lower frequency oscillation does not, consistent with the findings from the rotation study.

5.3.4 Discussion

We compare our experimentally observed SdH frequencies against band dispersion results obtained from ARPES measurements carried out by Chen *et al.* [12]. Using the values reported by the authors: the binding energy of the Dirac point is $E_0 = 0.34$ eV, and the slope of the linear dispersion is 2.67 eV Å, the empirical equation describing the surface state band (SSB) dispersion can be written as $E = -0.34 + 2.67|k|$. For the bottom conduction band (BCB) dispersion, a quadratic dispersion is used to visually fit the ARPES data, and the empirical equation obtained is $E = -0.055 + 14.9k^2$. The equations are overlaid on top of the ARPES band dispersion and are shown in Figure 5.16.

The frequency of the quantum oscillation is related to the k-space extremal cross-sectional area by the Onsager relation given in equation 2.23. Rearranging this equation, we obtain the Fermi wavevector k_F in terms of frequency F:

$$k_F = \sqrt{\frac{2eF}{\hbar}}. \tag{5.1}$$

Substituting the experimentally observed frequencies into the equation, the Fermi wavevectors for the higher and lower frequencies are $k_F = 0.10$ Å^{-1} and $k_F = 0.035$ Å^{-1} respectively, and are plotted as white dashed lines in Figure 5.16. The intersection of the dashed lines with the equations describing the SSB and the BCB would give the chemical potential μ for the material. Since the dashed lines each intersect the equations twice, there are two possible scenarios: either the lower frequency oscillation corresponds to the SSB while the higher frequency oscillation corresponds to the BCB, or vice versa.

It is clear from the plot that the latter case (higher frequency corresponds to SSB; lower frequency corresponds to BCB) fits our experimental observations better and putting the numbers into the equations, we obtain $E_{BCB} = -0.036$ eV and $E_{SSB} = -0.073$ eV. Although the computed values of the energy level differ slightly from each other, this difference is much smaller compared to that of the first case (0.04 eV compared to 0.4 eV). This again suggests that the higher 337 T frequency observed in the SdH experiments is due to the 2D surface state band, while the lower 40 T frequency is due to a bulk 3D conduction band.

This discrepancy in the calculated values for the chemical potential can be due to slight differences in the band structure parameters between our sample and Chen's. We can estimate the band parameters associated with the BCB and the SSB using our SdH data if we make the following assumptions: near the bottom of the conduction band, the band structure is approximately quadratic in nature, and thus the band dispersion has the form $E_{BCB} = \hbar^2 k^2 / 2m_0$; while the SSB has a linear dispersion of the form $E_{SSB} = \hbar \nu_F k$.

Here we recall equation 4.11 for the cyclotron mass $m^* = (\hbar^2/2\pi)\, \partial A(E)/\partial E|_{E=E_F}$, where $A(E)$ is the area enclosed by the cyclotron orbit in k-space. Since $A = \pi k_F^2$, we can make use of the band dispersions E_{BCB} and E_{SSB} to express the area in terms of energy E in order to evaluate the derivative.

For the case of the linear SSB, we obtain $m^* = E_F/\nu_F^2 = \hbar k_F/\nu_F$. Thus, the cyclotron mass obtained from the temperature dependence of the quantum oscillation amplitude is related to the slope of the Dirac dispersion by $\nu_F = \hbar k_F/m^*$. Substituting the value of $m^* = 0.24$ and $k_F = 0.10$ into this equation, we obtain a value $\nu_F = 3.2(3)$ eV Å.

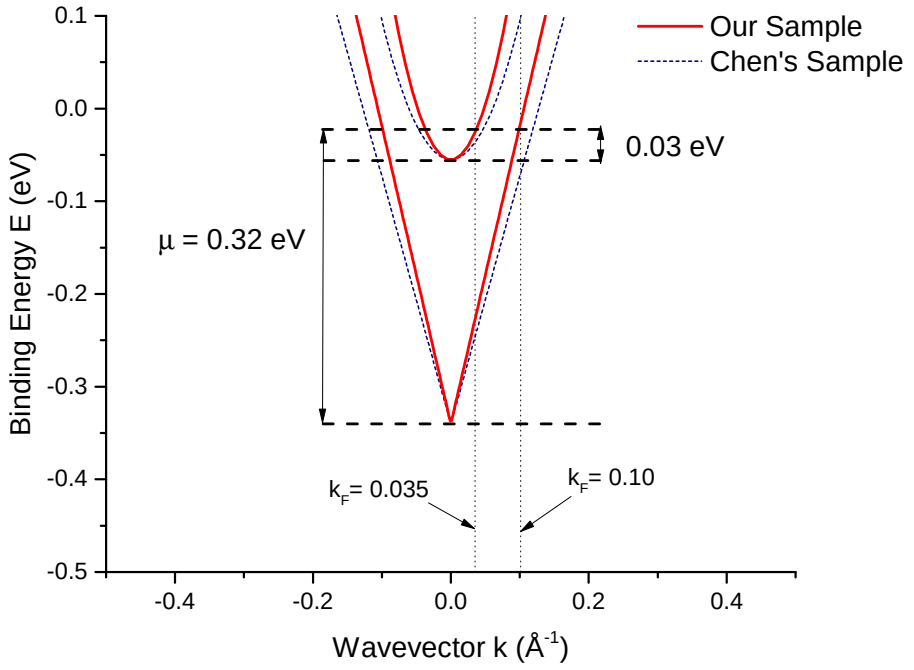

Figure 5.17: Comparison of band structure obtained from ARPES (dashed navy lines) and from SdH (solid red lines). The chemical potential is estimated to be 0.32 eV above the Dirac point.

For the case of BCB, repeating the calculations give the simple result $m^* = m_0 = 0.16(5)$, since we are assuming a parabolic behaviour near the BCB.

Thus, the band dispersions for the SSB and the BCB for our sample are modified to become $E = -0.34 + 3.21|k|$ and $E = -0.055 + 23.8k^2$ (if we also assume that the energy separation between the conduction band minimum and Dirac point remain unchanged). With these modified band parameters, substituting the values of k_F gives a much better estimate for the level of the chemical potential as the values obtained are closer together ($E_{BCB} = -0.026$ eV and $E_{SSB} = -0.016$ eV). Defining μ with respect to the Dirac point, the chemical potential for our sample is estimated to be $\mu = 0.32$ eV. The band dispersions obtained from our SdH measurements and from the ARPES measurements are plotted in Figure 5.17 for comparison.

Returning to the Hall effect data, since we have established that there are contributions from a surface state band and conduction band, we will use a two-band model to fit our experimental data in Figure 5.6:

$$\rho_{xy} = \frac{(n_s\mu_s^2 + n_b\mu_b^2)B + (\mu_s\mu_b)^2(n_s + n_b)B^3}{e((n_s\mu_s + n_b\mu_b)^2 + (\mu_s\mu_b)^2(n_s + n_b)^2B^2)}. \qquad \text{(2.59 revisited)}$$

Here, we have set $q \equiv e$, and allowed the polarity of the charge to be absorbed into

the parameters μ and n. The subscripts s and b represent carriers from the surface or bulk state respectively. The parameters μ and n in this model can be inferred from quantum oscillation measurements – carrier mobility takes the form:

$$\mu = \frac{e\tau}{m^*} = \frac{el}{\hbar k_F}, \tag{5.2}$$

where we have used the relations $l = \tau v_F$ and $v_F = \hbar k_F / m^*$.

Assuming that we have a spherical Fermi surface, carrier density for the bulk and surface is estimated from quantum oscillation measurements using:

$$\begin{aligned} n_{3D} &= \frac{2}{(2\pi)^3}\left(\frac{4}{3}\pi k_F^3\right) = \frac{k_F^3}{3\pi^2}, \\ n_{2D} &= \frac{2}{(2\pi)^2}(\pi k_F^2) = \frac{k_F^2}{2\pi}. \end{aligned} \tag{5.3}$$

Substituting the values of l and k_F into the equations, the calculated values of mobility μ and n are shown in Table 5.2.

	F (T)	m^* (m_e)	l (nm)	k_F (Å^{-1})	μ (m^{2}V^{-1}s^{-1})	n_{2D}/n_{3D} (m^{-2}/m^{-3})
SSB	340(30)	0.24(2)	21.4(2)	0.101(4)	0.032(1)	$1.6(1) \times 10^{17}$
BCB	40(5)	0.16(5)	29.3(5)	0.035(2)	0.13(1)	$1.5(2) \times 10^{24}$

Table 5.2: Summary of results obtained from ambient pressure quantum oscillation study of Bi_2Te_3 .

The effective 3D carrier density for the surface carriers n_s can be computed from the 2D density via $n_s = n_{2D}/t$, where $t = 10\,\mu$m is the thickness of our sample.

Using equation 2.59 with four free parameters (μ_s, μ_b, n_s, n_b) to fit the Hall data, we run into the problem of over-parametrizing our model leading to convergence issues. Instead, one of the parameters μ is constrained using the results from the SdH quantum oscillation measurements, which allowed the fitting routine to converge when suitable initial values of n_s and n_b were used (μ_s had to be perturbed slightly from the value given in Table 5.2 for the fit to converge). We found that when using n_s and n_b values that were derived from the quantum oscillation data as the initial guess, the non-linear fitting routine was unable to converge. By systematically increasing n_s and n_b by factors of 10 each time, the fits finally converged when an initial value of $\sim 10^{26}$ for n_s and n_b was used.

The results of the fit are shown in Figure 5.18 and the fit parameters shown in Table 5.3. Depending on whether μ_s or μ_b was fixed, we obtain slightly different values of the fit parameters, as shown in the inset. Both sets of parameters produce a fit (shown by dashed red line) that closely matches the experimental data.

For both fits, we find that n_s and μ_s have opposite signs to n_b and μ_b, suggesting

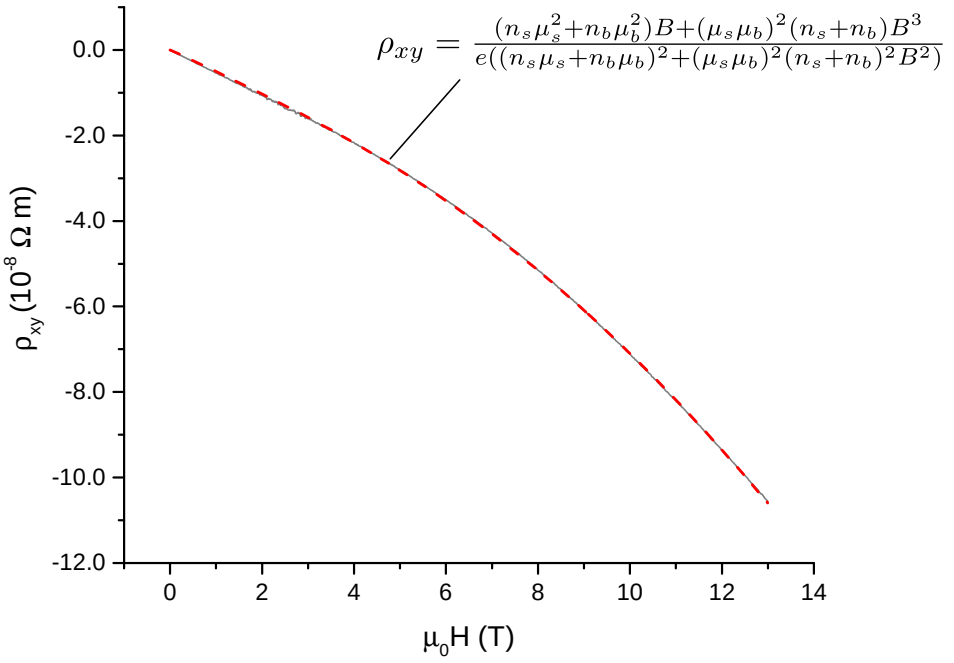

Figure 5.18: Two-band model used to fit the Hall resistivity. Dashed line represents the fitted curve.

that there are charge compensation effects happening in our sample.[1] In particular, the sign of the parameters indicate that the carriers for the bulk are electron-like while that for the surface are hole-like in nature, with a slightly higher density of negative carriers, resulting in an overall n-type behaviour for the sample.

Although this model can provide a good fit to the data, there are some discrepancies between the model parameters when compared to the results from quantum oscillation measurements. Notably, the carrier densities for the bulk carriers ($\sim 10^{24}$) as well as the effective density for the surface carriers ($\sim 10^{22}$) obtained from quantum oscillations are several orders of magnitude lower than that obtained from the fit. Moreover, given the Fermi level and band dispersion estimated from the SdH study, we expect carriers from both the surface state and bulk state to be n-type in nature. This is not consistent with the values obtained from the fit, which suggests the coexistence of charge carriers with opposite polarities instead. It might be possible that there are other bulk bands contributing to the conductivity and a three-band model might better capture the behaviour of our sample.

[1] The behaviour of the two band model under different permutations of the ratios n_1/n_2, μ_1/μ_2 is explored in more detail in Appendix.C

	Fix μ_s	Fix μ_b
n_s (m^{-3})	$1.95(9) \times 10^{25}$	$2.33(7) \times 10^{26}$
n_b (m^{-3})	$-3.78(1) \times 10^{26}$	$-5.91(2) \times 10^{26}$
μ_s (m^2/Vs)	0.055	0.0944(2)
μ_b (m^2/Vs)	-0.0164(4)	-0.13

Table 5.3: Parameters obtained from the two-band model fit. Highlighted cells represent the fixed parameters.

5.4 High Pressure Study of Bi_2Te_3

High pressure studies of Bi_2Te_3 were carried out in a piston-cylinder cell, alongside the other samples of BiTeI. The same sample that was measured under ambient conditions at the high field facility was used for this pressure study.

5.4.1 Resistivity and Hall Measurements

The longitudinal resistivity component for the sample, measured at the base temperature of 2 K, is plotted as a function of pressure in Figure 5.19. The general trend observed was that as pressure is increased, resistivity of the sample decreases. For our sample, the

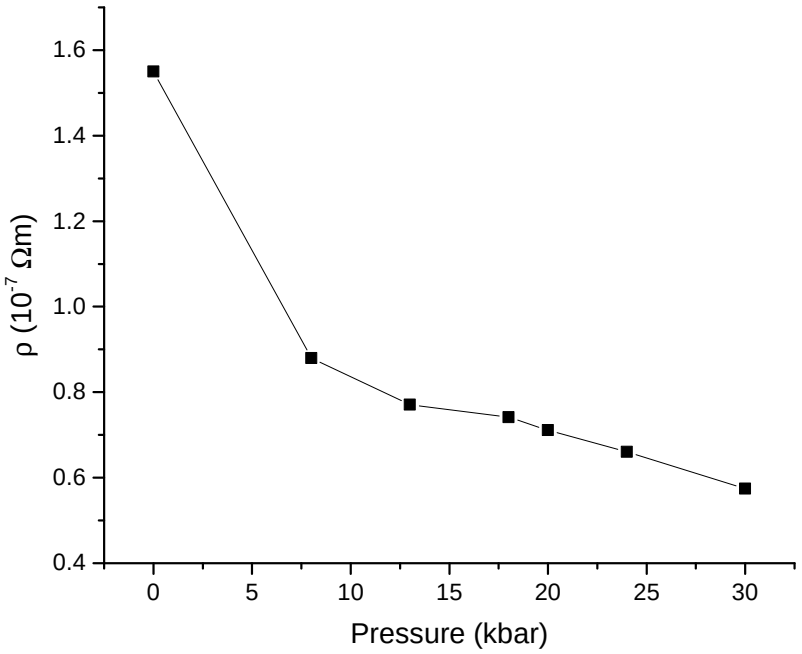

Figure 5.19: Resistivity of Bi_2Te_3 as a function of pressure. As pressure is increased, resistivity decreases and sample becomes more metallic.

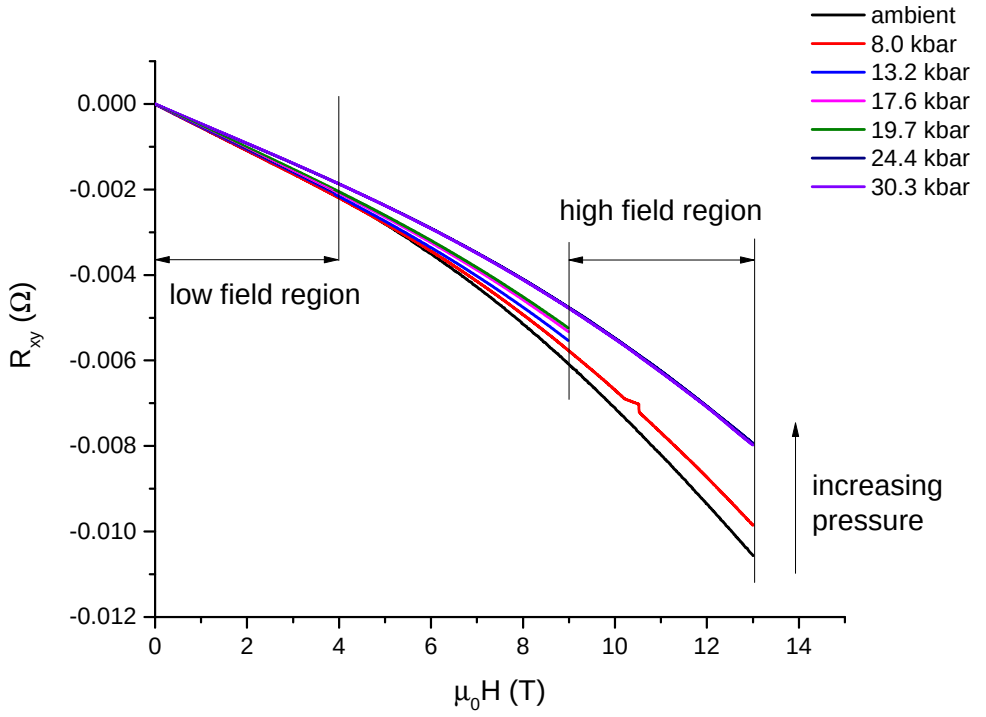

Figure 5.20: Transverse component of resistivity as a function of field, for the different pressure points.

resistivity drops by a factor of about three when pressurised to 30 kbar, with the largest change occurring between 0–8 kbar. The general trend of the resistivity is consistent with work carried out by Jacobsen *et al.* [87], as well as studies that demonstrated the semiconductor-to-metal transition of Bi_2Te_3 under pressure [90, 88].

The transverse component of resistivity R_{xy} is obtained by sweeping the magnetic field in both the positive and negative direction, followed by anti-symmetrising the data. The measurements carried out at each pressure point are plotted in Figure 5.20. For the pressure runs from 13 to 20 kbar, anti-symmetrised R_{xy} data was only measured up to 9 T as the experiment was conducted in the PPMS while anti-symmetrised R_{xy} data was available up to 13 T for the other pressure points.

For our sample of Bi_2Te_3 , R_{xy} does not vary linearly with magnetic field over the entire field range – the slope is not constant. We identified a low field region (0–4 T) and a high field region (9–13 T) where R_{xy} can be fitted with a linear equation in order to obtain the slope for the plot and hence the Hall coefficients (using equation 4.2) for the respective regions.

Since anti-symmetrised data for the high field region is absent for pressure points between 13 to 20 kbar, the unsymmetrised component of resistivity is used to estimate the Hall coefficient. For pressure runs (ambient, 8, 24, 30 kbar) where unsymmetrised and

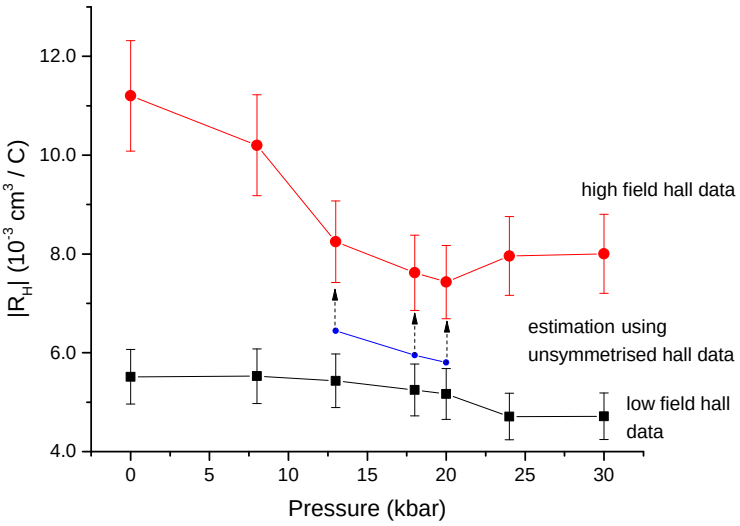

(a)

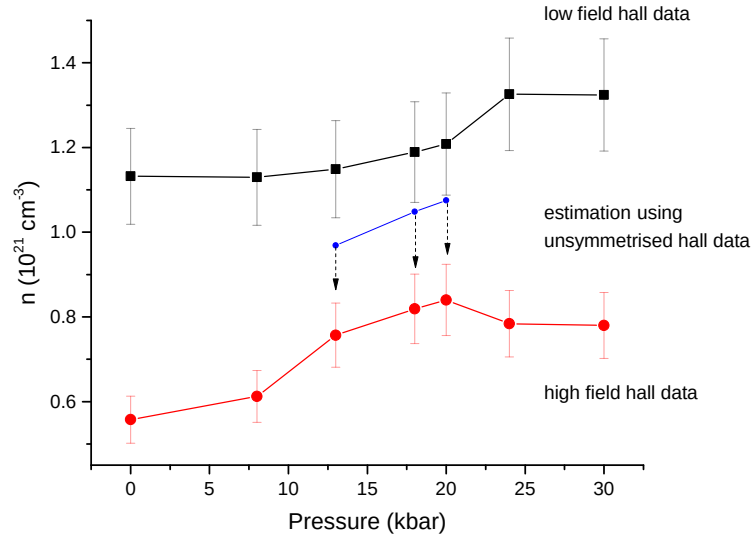

(b)

Figure 5.21: Pressure dependence of (a) Hall coefficient and (b) carrier density of Bi_2Te_3. Unsymmetrised data (blue), together with a correction factor of 1.25 is used to estimate anti-symmetrised data for $P = 13, 18, 20$ kbar.

anti-symmetrised data are available, it is found that the unsymmetrised data overestimates the high-field slope by a factor of about 1.2–1.3 compared to the anti-symmetrised data. With this as a guide, we will use a value of 1.25 as a correction factor to estimate the high-field slope for the pressure runs 13, 18 and 20 kbar.

The Hall coefficient as well as the carrier density are then computed and plotted as a function of pressure in Figures 5.21a and 5.21b respectively. Focusing on n and R_H

obtained from the low-field region, there is a kink in the plot at about 20 kbar. Although the change in carrier density is small – 1% increase in n at 24 kbar (compared to a 270% increase for Zhang's sample [88] at 40 kbar) – the derivative of n with respect to pressure shows a clear spike in that pressure region. Although the quantities for n and R_H for the high field region are not complete for the entire pressure range and certain values have to be estimated, they too show some sort of feature that occur at around 20 kbar.

Work done by previous groups report the existence of an electronic topological transition (ETT) of Bi_2Te_3 under pressure. However, the reported critical pressure for this ETT ranges between 20–40 kbar (values of 20 kbar reported by [85, 87], 32 kbar by [86] and 40 kbar by [88]). Our result appears to be consistent with previous findings and lends support that the ETT occurs at a pressure closer towards 20 kbar. Since the ETT is a type of transition that modifies the topology of the Fermi surface, quantum oscillation measurements are ideally suited to study such transitions.

5.4.2 Quantum Oscillation Measurements

Shubnikov-de Haas measurements of Bi_2Te_3 under pressure were carried out using the 15T system. Up to the maximum field of 15 T, we were unable to discern any oscillations with frequencies above 300 T in our pressure measurements, thus were unable to track the behaviour of the surface state band as a function of pressure. At low pressures, we were able to observe a low frequency oscillation, which is most likely from the BCB that we observed at ambient pressure. At 18 kbar, there are hints of a second frequency appearing, and this higher frequency becomes very apparent at 20 kbar. This frequency persisted up to 30 kbar.

The plots of the SdH measurements for the individual pressure runs will be grouped in pairs for comparison. For all the plots, a fifth order polynomial was used to fit the background signal, and the residual after background subtraction was plotted against inverse field. The temperature dependence of the quantum oscillation amplitude that was used to fit for the effective mass is shown as an inset on the right.

Figures 5.22a and 5.22b are the SdH plots for the pressure points 8 kbar and 13 kbar. Only one dominant frequency was observed at these pressures, 61 T at 8 kbar and 83 T at 13 kbar. At fields above 12.5 T for both pressure points, there appears to be contribution from another frequency. As this frequency did not give a sensible fit for the mass plot, it will be ignored.

Figures 5.23a and 5.23b are the SdH plots for the pressure points 18 kbar and 20 kbar. At 18 kbar, we observe signatures of a second frequency, as the resultant signal appears to be a superposition of two frequencies close together. This is indeed the case when a two frequency model (shown by the black dotted line) is used to fit the data, and the

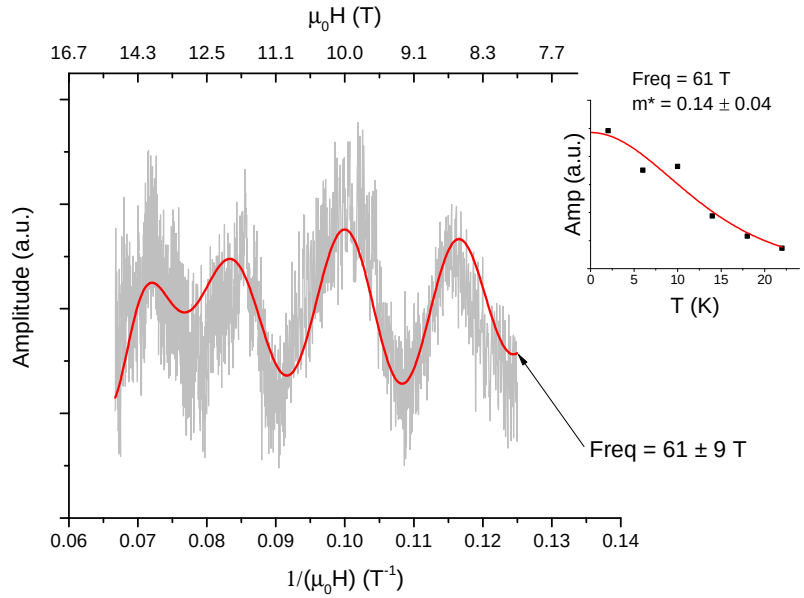

(a)

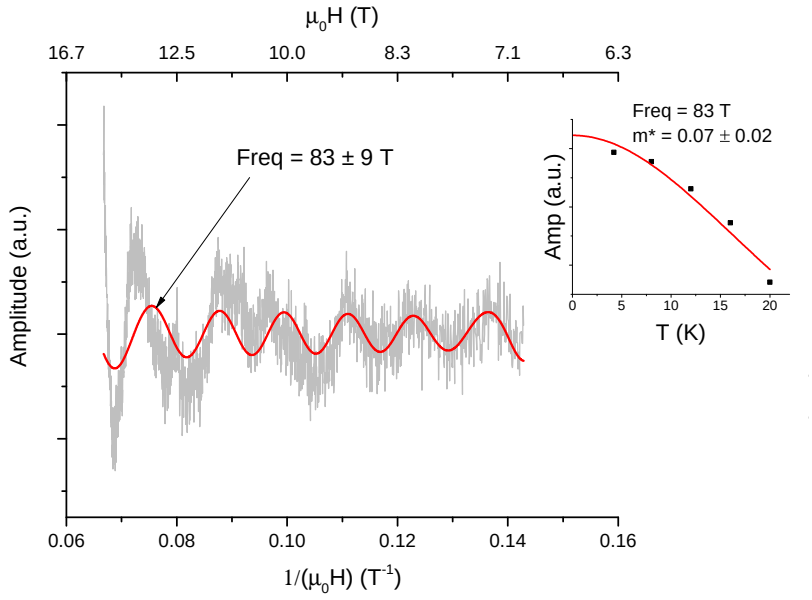

(b)

Figure 5.22: SdH oscillations at the pressure of (a) 8 kbar, (b) 13 kbar. One dominant frequency is observed at these pressures.

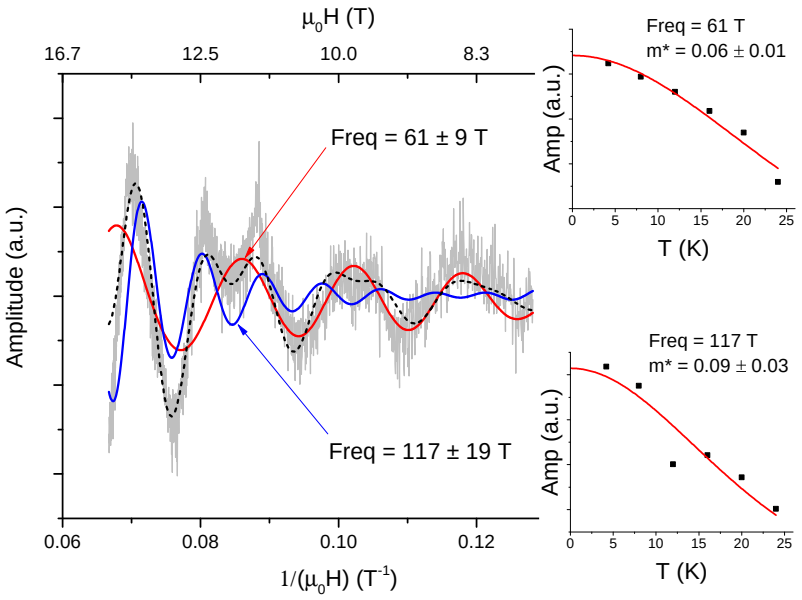

(a)

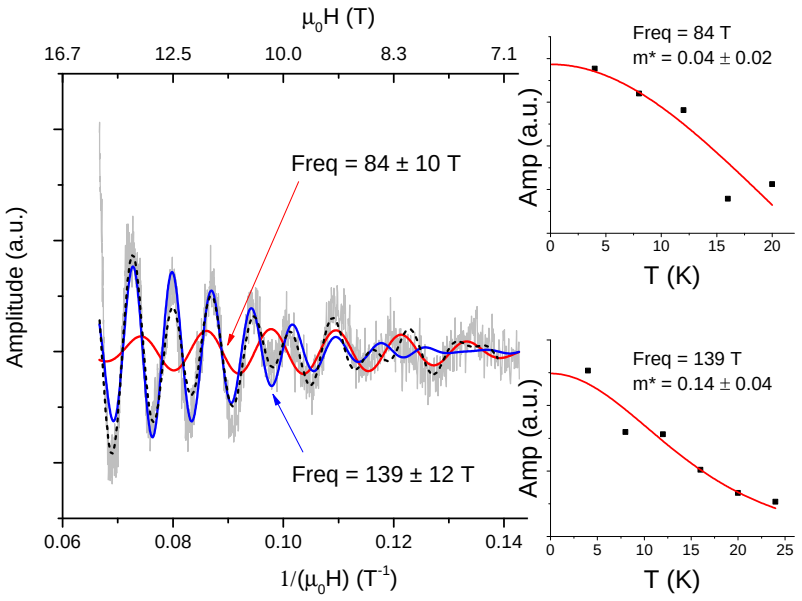

(b)

Figure 5.23: SdH oscillations at the pressure of (a) 18 kbar, (b) 20 kbar. The black dotted line is a two frequency fit to the data. At 18 kbar, there are hints of a second frequency appearing. This frequency can be clearly observed at 20 kbar, particularly at fields above 10 T.

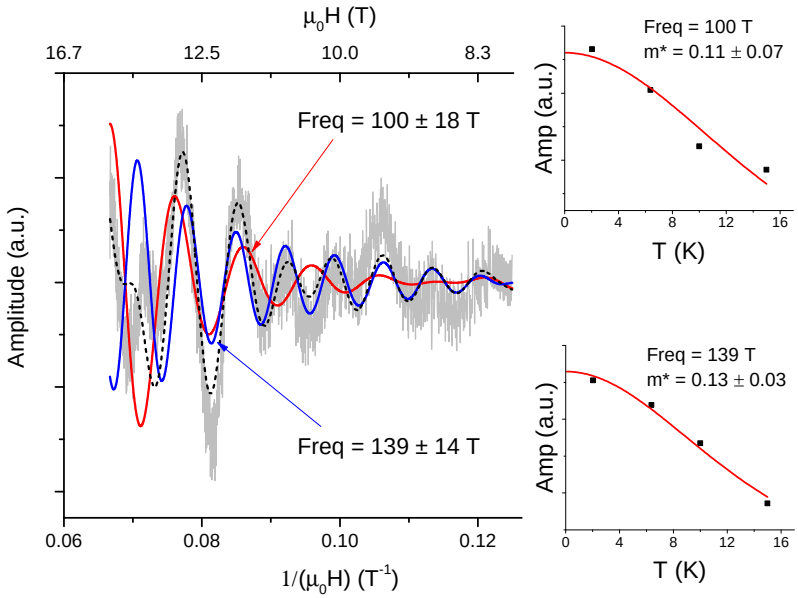

(a)

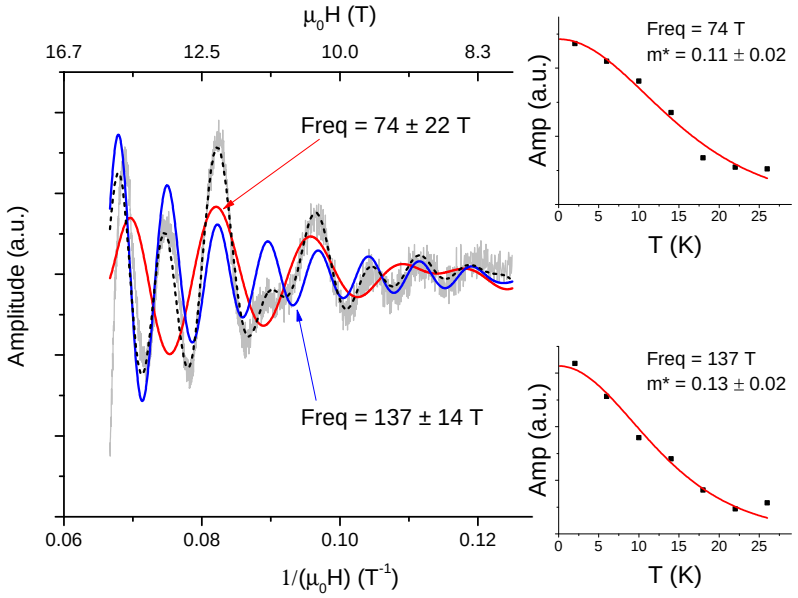

(b)

Figure 5.24: SdH oscillations at the pressure of (a) 24 kbar, (b) 30 kbar. The black dotted line is a two frequency fit to the data. The second frequency is observed to persist up to the maximum applied pressure of 30 kbar and there is little variation in the frequency or the effective mass with pressure.

frequencies are determined to be 61 and 117 T. Using the FFT band-pass filter, their individual contributions to the overall signal can be isolated and plotted. At 20 kbar, the second frequency (139 T) becomes apparent and it is the dominant signal at fields above 10 T. At fields below 10 T, the amplitude of the lower frequency (84 T) becomes larger and becomes the more dominant oscillation signal.

Lastly, Figures 5.24a and 5.24b are the SdH plots for the pressure points 24 kbar and 30 kbar. For these two pressure points, the signal can be well fitted by a two frequency model and the individual frequencies are overlaid on the plot as a visual reference. The $\sim$139 T oscillation shows little variation in both frequency and effective mass from 20 to 30 kbar.

5.4.3 Discussion

The quantum oscillation frequency and effective mass is plotted as a function of pressure in Figure 5.25. The frequencies are represented by circles, whose areas are proportional to the amplitude of the FFT peak, while the effective masses are represented as triangles.

We observe a gradual increase in the BCB frequency up to 13 kbar, followed by a slight drop at 18 kbar. At this pressure, another oscillation with a slightly higher frequency can just about be resolved. This higher frequency oscillation becomes more apparent at pressures above 18 kbar and does not show much variation in frequency at these pressures. For the effective mass plot, m^* for the lower frequency oscillation decreases with increasing pressure initially, reaching a minimum at 20 kbar before increasing again. Above 20 kbar, m^* for the higher frequency oscillation remains constant in pressure.

From our quantum oscillation study of Bi_2Te_3 under pressure, a new frequency is observed at a pressure of 20 kbar, while Hall measurements showed anomalies in the carrier density in the pressure range of 20–24 kbar. Since these experimental observations are unlikely to be associated with a structural change of Bi_2Te_3 as X-ray diffraction studies conducted by other groups [85, 86, 90] have already shown that the structural transition occurs at a much higher pressure of 80 kbar, we interpret these observations as indications of an electronic topological transition in Bi_2Te_3 that occur at a pressure of about 20 kbar.

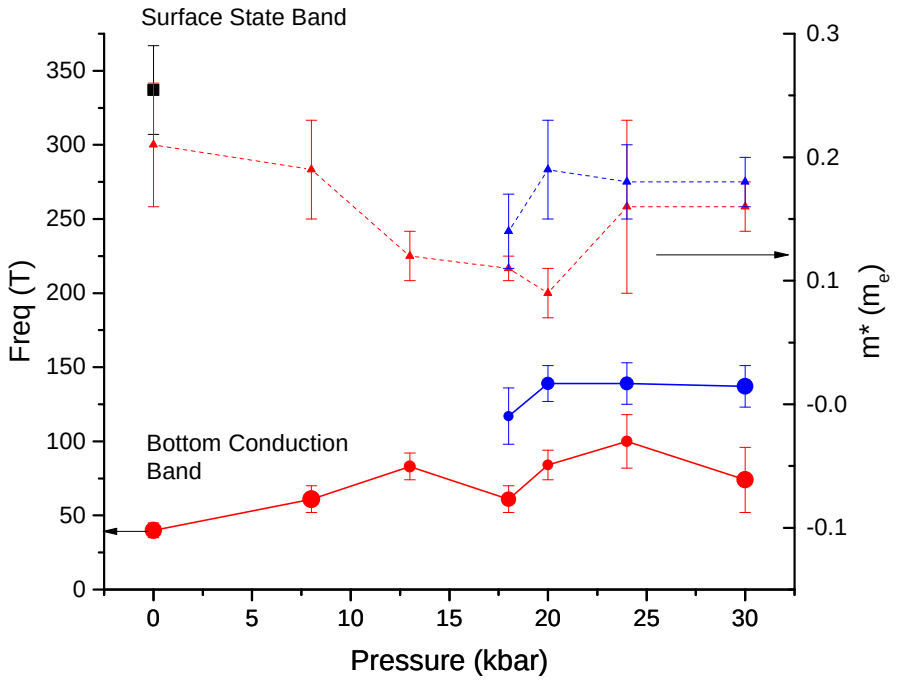

Figure 5.25: Pressure dependence of the quantum oscillation frequency (circles) and effective mass (triangles). The size of the frequency data point is proportional to the amplitude of the FFT peak. The lower frequency is plotted in red while the higher frequency is plotted in blue colour.

Chapter 6

Conclusion

In this work, two materials BiTeI and Bi_2Te_3 were studied by performing Shubnikov-de Haas measurements under pressure. Using the piston-cylinder cell, we were able to track the evolution of the quantum oscillation frequencies up to a modest pressure of 30 kbar.

For the BiTeI samples, we were able to reliably observe the evolution of two Fermi surface sheet orbits with pressure. The inner Fermi surface expands ($\sim$20–40 T) while the outer Fermi surface shrinks ($\sim$470–360 T) as pressure is increased. The frequencies can be fairly well described using a model Rashba Hamiltonian and we were able to obtain parameters for the model Hamiltonian by fitting experimentally observed quantum oscillation frequencies and effective masses to this model. Using these parameters, we were able to calculate the carrier densities for our sample which showed good agreement with experimental Hall measurements. At ambient pressure, phase analysis of the quantum oscillations showed that both inner and outer Fermi surfaces exhibit non-trivial π-Berry phase, consistent with theoretical expectations. At higher pressures, we observed a splitting of frequencies associated with the inner Fermi surface for the 5% sample, but not for the 10% sample. This splitting of frequencies, together with the changes in quantum oscillation phase, can be explained by a change in the Fermi surface topology and is consistent with previous reports of a pressure-induced topological transition occurring in BiTeI.

For the Bi_2Te_3 sample, we observed two quantum oscillation frequencies based on several measurements conducted on different samples. Results suggest that the low-frequency ($\sim$40 T) oscillation originates from the bulk conduction band while the higher-frequency ($\sim$ 337 T) oscillation corresponds to the surface state band. This finding is supported by performing phase analysis on the oscillations, the partial rotation study conducted on our dilution refrigerator, as well as a comparison to ARPES band structure results carried out by other groups. When the sample was pressurised, we observed the emergence of a new frequency at a pressure of 18 kbar. Pressure dependence of the Hall coefficient also shows a kink at around 20 kbar. Our observations support the findings of an electronic topological transition occurring in Bi_2Te_3 and our results indicate that the critical pressure occurs at around 20 kbar.

Due to the limitations of our experimental setup, the longitudinal and transverse resistivity measurements of our samples could only be carried out at ambient pressure. Without both components at higher pressures, it is not possible to construct the conductivity for our samples so that a proper Landau indexing phase analysis could be carried out. A proper phase analysis would give us more confidence in the evolution of the quantum oscillation phase with pressure. Thus, it would be desirable if the samples were contacted in a way such that both longitudinal and transverse components could be measured simultaneously (e.g. Hall bar geometry with six contacts).

Appendix A

Fast Fourier Transform

In order to help with the analysis of quantum oscillations observed in measurements, a program called QFFT was written in MATLAB. This program has been maintained and incrementally developed with additional functionality by colleagues within the group (Mike Sutherland, Swee Goh, Xiaoye Chen and myself) over the years. A graphical user interface (GUI) makes the analysis more convenient and accessible even for users not familiar with programming in MATLAB.

The majority of the functions coded into QFFT is to treat and process the experimental data in order to obtain the quantum oscillation signal. Writing the resistivity trace as

$$\rho(B) = \rho_0(B) + \rho_{osc}(B), \tag{A.1}$$

where ρ_{osc} and ρ_0 are the oscillatory and non-oscillatory signals of the resistivity data respectively.

First, QFFT performs a polynomial fit for ρ_0, which is then subtracted from ρ to leave behind the signal corresponding to the oscillations. In general, the lowest possible polynomial order is used for fitting and subtracting the background signal ρ_0, as high order polynomials might overfit the data and leave behind spurious peaks in the FFT spectrum. Determining a suitable polynomial order for performing background subtraction is conducted through a trial and error process, and the peaks observed in the FFT spectrum have to be cross-checked (e.g. sensible temperature dependence of FFT amplitude from equation 2.35, theoretical predictions of frequencies) to make sure they are not introduced during background subtraction.

As the oscillations are periodic in $1/B$ while the measurements are carried out in B, the data would have to be converted into inverse field, followed by linear interpolation to ensure that the data is evenly spaced in inverse field. Next, the dataset is padded with zeroes in order to make the total number of data points a power of 2 (improves computational efficiency of FFT algorithm) and to increase the sampling in the transformed domain. Finally, the dataset is multiplied by a suitable windowing function (QFFT uses

the Hamming window), which smooths the data in the time-domain, reducing spectral leakage in the frequency-domain. More details regarding the theory and considerations of the FFT can be found in [92].

The oscillations are then fed into the FFT routine of MATLAB, and the resultant frequency spectrum is plotted in the GUI. Other functions in QFFT include LK fits, temperature dependence fits and band-pass filtering of frequencies.

Appendix B

BiTeI Table of Results

Band parameters obtained from quantum oscillation measurements using equations 4.10 and 4.12.

	P (kbar)	$F^+(T)$	$F^-(T)$	$m^+(m_e)$	$m^-(m_e)$	f	$m_0(m_e)$	μ(eV)	α(eVÅ)	E_R(eV)
0% Sample	0.7	43 ± 10	502 ± 42	–	–	0.43 ± 0.09	–	–	–	–
	9.2	49 ± 10	483 ± 32	0.057 ± 0.003	0.16 ± 0.03	0.36 ± 0.08	0.11 ± 0.02	0.17 ± 0.03	3.0 ± 0.5	0.06 ± 0.02
	20.3	56 ± 10	470 ± 32	0.062 ± 0.003	0.16 ± 0.03	0.31 ± 0.06	0.11 ± 0.02	0.17 ± 0.03	2.8 ± 0.4	0.05 ± 0.01
5% Sample	0	20 ± 3	440 ± 32	0.042 ± 0.003	0.19 ± 0.02	0.7 ± 0.1	0.12 ± 0.01	0.09 ± 0.01	3.0 ± 0.3	0.07 ± 0.01
	13.2	29 ± 4	393 ± 39	0.044 ± 0.003	0.16 ± 0.02	0.49 ± 0.07	0.10 ± 0.01	0.12 ± 0.02	2.9 ± 0.3	0.06 ± 0.01
	17.6	32 ± 2	398 ± 35	0.045 ± 0.003	0.14 ± 0.02	0.45 ± 0.04	0.09 ± 0.01	0.15 ± 0.02	3.4 ± 0.4	0.07 ± 0.01
	19.7	34 ± 9	389 ± 39	0.050 ± 0.003	0.13 ± 0.02	0.4 ± 0.1	0.08 ± 0.01	0.16 ± 0.03	3.5 ± 0.6	0.07 ± 0.02
	24.4	36 ± 4	371 ± 34	0.052 ± 0.003	0.14 ± 0.02	0.38 ± 0.05	0.09 ± 0.01	0.14 ± 0.02	3.0 ± 0.4	0.05 ± 0.01
	30.3	41 ± 4	360 ± 34	0.049 ± 0.003	0.13 ± 0.02	0.33 ± 0.05	0.08 ± 0.01	0.16 ± 0.02	3.1 ± 0.4	0.05 ± 0.01
10% Sample	0	30 ± 8	472 ± 33	0.055 ± 0.003	0.22 ± 0.02	0.6 ± 0.1	0.14 ± 0.02	0.10 ± 0.03	2.5 ± 0.5	0.06 ± 0.02
	8	18 ± 4	409 ± 29	0.054 ± 0.003	0.17 ± 0.02	0.8 ± 0.1	0.16 ± 0.02	0.06 ± 0.02	2.1 ± 0.4	0.05 ± 0.02
	13.2	25 ± 3	398 ± 27	0.045 ± 0.003	0.13 ± 0.02	0.57 ± 0.07	0.11 ± 0.01	0.10 ± 0.02	2.8 ± 0.3	0.06 ± 0.01
	17.6	28 ± 5	396 ± 28	0.047 ± 0.003	0.12 ± 0.02	0.51 ± 0.09	0.11 ± 0.01	0.11 ± 0.03	2.8 ± 0.4	0.06 ± 0.02
	19.7	29 ± 3	391 ± 30	0.049 ± 0.003	0.13 ± 0.02	0.48 ± 0.06	0.11 ± 0.01	0.11 ± 0.02	2.7 ± 0.3	0.05 ± 0.01
	24.4	30 ± 4	380 ± 27	0.050 ± 0.003	0.15 ± 0.02	0.46 ± 0.06	0.11 ± 0.01	0.11 ± 0.02	2.6 ± 0.3	0.05 ± 0.01
	30.3	31 ± 4	378 ± 28	0.051 ± 0.003	0.14 ± 0.02	0.45 ± 0.06	0.12 ± 0.01	0.11 ± 0.02	2.5 ± 0.3	0.05 ± 0.01

Table B.1: Band parameters calculated from SdH frequencies and effective masses for the three samples.

Appendix C

Two-band model

The two-band model given in equation 2.59 can be rewritten as:

$$\rho_{xy} = \frac{1}{en_1} \frac{(\mu_2^{-1} + \frac{n_2}{n_1}\mu_1^{-1})B + (1 + \frac{n_2}{n_1})B^3}{(\mu_2^{-1} + \frac{n_2}{n_1}\mu_1^{-1})^2 + (1 + \frac{n_2}{n_1})^2 B^2}. \tag{C.1}$$

Depending on the type of charge carriers, density of carriers and carrier mobilities relative to each other, the equation would exhibit different behaviour as a function of B.

C.1 Same Charge

When the carriers have the same charge and mobilities, the two-band model effectively becomes a single-band model where the total density is given by the sum of the two individual densities n_1 and n_2, and we obtain a linear ρ_{xy} with B. With increasing n_2/n_1, the total number of carriers increases, resulting in a decrease in the slope which is basically the Hall coefficient $1/en_{tot}$. This can be seen in Figure C.1

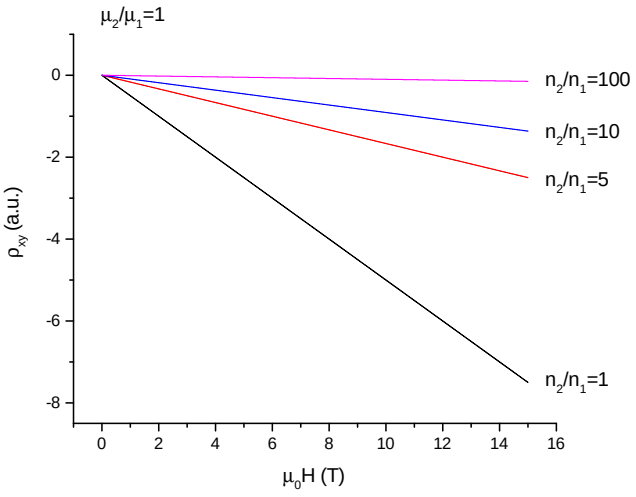

Figure C.1: The case where $\mu_2 = \mu_1$. When n_2 is increased, Hall coefficient (slope) decreases.

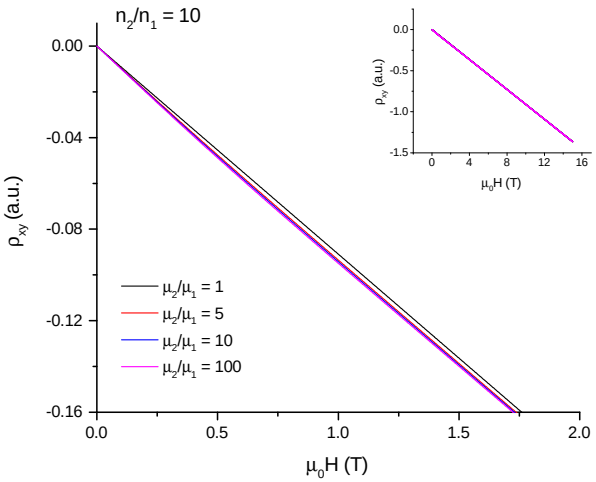

Figure C.2: The case where $n_2 > n_1$, $\mu_2 > \mu_1$. ρ_{xy} is almost linear in B and independent of μ.

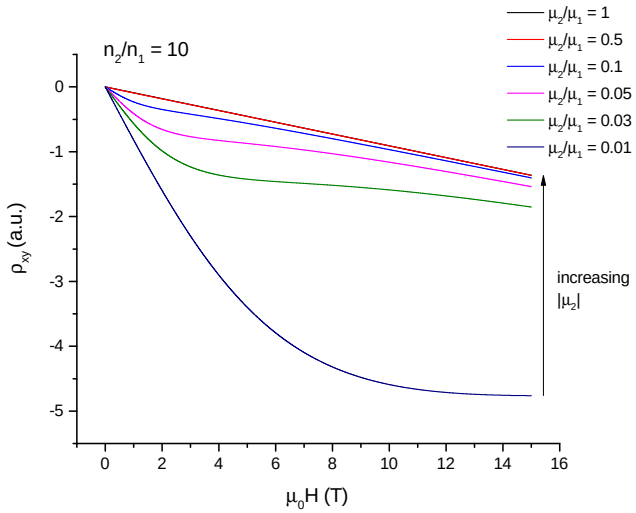

Figure C.3: The case where $n_2 > n_1$, $\mu_2 < \mu_1$. Competing effects between carrier density and mobility, resulting in non-linear behaviour at low fields.

When there is an imbalance of carrier densities, e.g. $n_2 > n_1$, if the mobility of carrier 2 is larger than carrier 1, we can ignore contributions from carrier 1 and once again obtain a single-band model where the slope is almost constant and independent of carrier mobility (Figure C.2). However, when the mobility of carrier 2 is smaller than carrier 1, we have to take into account competing contributions from both carriers, which leads to a saturation of transverse resistivity at low fields, before becoming linear in B again in the high field limit (Figure C.3). This saturation of resistivity was observed in [24] where the authors observed low carrier density, high mobility for the surface state; and high carrier density, low mobility for the bulk state.

C.2 Opposite Charge

When there are carriers of opposite charge, we can look at two cases: the uncompensated case where $n_1 \gg n_2$ and the compensated case where $n_2 \simeq n_1$.

For the uncompensated case plotted in Figure C.4, if the mobility of carrier 2 is smaller than that of carrier 1, we can ignore contributions from carrier 2 and the system approximates to a single-band model. When mobility of carrier 2 is larger than carrier 1, we once again get competing effects from the different carriers, and the model predicts a change in sign of the Hall coefficient as the field is swept. At high fields, transverse resistivity becomes linear in B.

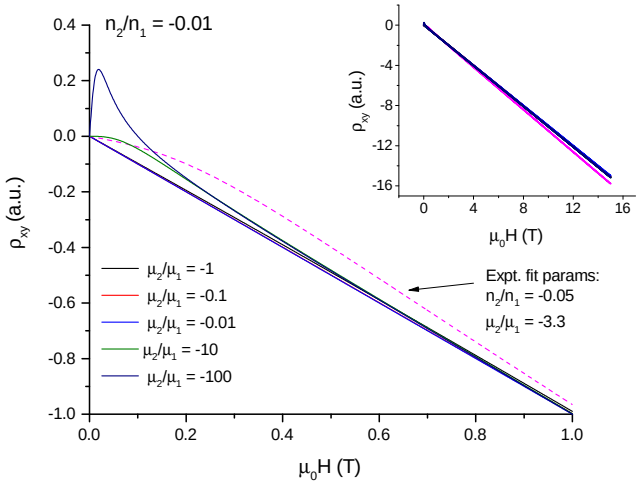

Figure C.4: The case where $n_2 \ll n_1$. When $\mu_2 < \mu_1$, revert back to single-band model. When $\mu_2 > \mu_1$, the model predicts a sign change in transverse resistivity before becoming linear in B at high fields.

When the densities for the two carriers are equal, the metal can be considered fully compensated and analysis shows that the transverse resistivity is quadratic in field [93, 94, 95]. When compensation is not quite perfect (e.g. $n_2 = 0.9n_1$), we still see a quadratic dependence on field, depending on the relative values of the carrier mobilities. As shown in Figure C.5, contribution to the overall transverse resistivity decreases with decreasing mobility of carrier 2, the two-band model approximates to a single-band model and thus the quadratic behaviour becomes less pronounced. On the other hand, when mobility of carrier 2 is increased in Figure C.6, competing effects between the positive and negative carriers results in a region where transverse resistivity is positive before becoming negative as field is further increased.

For our Bi_2Te_3 sample, Hall measurements suggest that there are carriers of opposite charge, and depending on which set of fitting parameters is used, we can be either be in

the (i) $n_2 \ll n_1$, $\mu_2 < \mu_1$, or in the (ii) $n_2 \lesssim n_1$, $\mu_2 < \mu_1$ regime.

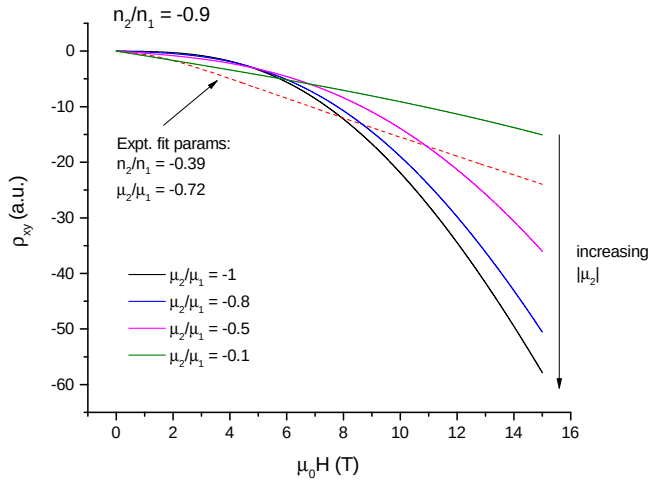

Figure C.5: The case where $n_2 \lesssim n_1$. As $|\mu_2|$ becomes smaller, ρ_{xy} tends towards linearity.

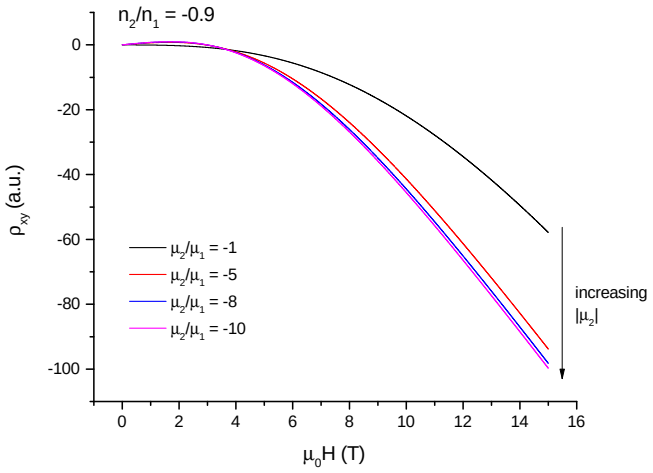

Figure C.6: The case where $n_2 \lesssim n_1$. As $|\mu_2|$ becomes larger, competition between the positive and negative carriers results in a region where ρ_{xy} changes sign.

Bibliography

[1] L. Landau, "The theory of a Fermi liquid," *Soviet Physics Jetp-Ussr*, vol. 3, no. 6, pp. 920–925, 1957.

[2] L. D. Landau, "On the theory of phase transitions," *Ukr. J. Phys.*, vol. 11, pp. 19–32, 1937.

[3] K. v. Klitzing, G. Dorda, and M. Pepper, "New method for high-accuracy determination of the fine-structure constant based on quantized Hall resistance," *Physical Review Letters*, vol. 45, no. 6, p. 494, 1980.

[4] D. J. Thouless, M. Kohmoto, M. P. Nightingale, and M. Den Nijs, "Quantized Hall conductance in a two-dimensional periodic potential," *Physical Review Letters*, vol. 49, no. 6, p. 405, 1982.

[5] M. Z. Hasan and C. L. Kane, "Colloquium: topological insulators," *Reviews of Modern Physics*, vol. 82, no. 4, p. 3045, 2010.

[6] B. A. Bernevig, T. L. Hughes, and S.-C. Zhang, "Quantum spin Hall effect and topological phase transition in HgTe quantum wells," *Science*, vol. 314, no. 5806, pp. 1757–1761, 2006.

[7] M. König, S. Wiedmann, C. Brüne, A. Roth, H. Buhmann, L. W. Molenkamp, X.-L. Qi, and S.-C. Zhang, "Quantum spin Hall insulator state in HgTe quantum wells," *Science*, vol. 318, no. 5851, pp. 766–770, 2007.

[8] L. Fu and C. L. Kane, "Topological insulators with inversion symmetry," *Physical Review B*, vol. 76, no. 4, p. 045302, 2007.

[9] D. Hsieh, D. Qian, L. Wray, Y. Xia, Y. S. Hor, R. J. Cava, and M. Z. Hasan, "A topological Dirac insulator in a quantum spin Hall phase," *Nature*, vol. 452, no. 7190, p. 970, 2008.

[10] H. Zhang, C.-X. Liu, X.-L. Qi, X. Dai, Z. Fang, and S.-C. Zhang, "Topological insulators in Bi2Se3, Bi2Te3 and Sb2Te3 with a single Dirac cone on the surface," *Nature physics*, vol. 5, no. 6, p. 438, 2009.

[11] Y. Xia, D. Qian, D. Hsieh, L. Wray, A. Pal, H. Lin, A. Bansil, D. Grauer, Y. S. Hor, R. J. Cava, *et al.*, "Observation of a large-gap topological-insulator class with a single Dirac cone on the surface," *Nature physics*, vol. 5, no. 6, p. 398, 2009.

[12] Y. Chen, J. G. Analytis, J.-H. Chu, Z. Liu, S.-K. Mo, X.-L. Qi, H. Zhang, D. Lu, X. Dai, Z. Fang, *et al.*, "Experimental realization of a three-dimensional topological insulator, Bi2Te3," *science*, vol. 325, no. 5937, pp. 178–181, 2009.

[13] D. Pesin and A. H. MacDonald, "Spintronics and pseudospintronics in graphene and topological insulators," *Nature materials*, vol. 11, no. 5, p. 409, 2012.

[14] T. Yokoyama and S. Murakami, "Spintronics and spincaloritronics in topological insulators," *Physica E: Low-dimensional Systems and Nanostructures*, vol. 55, pp. 1–8, 2014.

[15] X.-L. Qi, T. L. Hughes, and S.-C. Zhang, "Topological field theory of time-reversal invariant insulators," *Physical Review B*, vol. 78, no. 19, p. 195424, 2008.

[16] L. Fu and C. L. Kane, "Superconducting proximity effect and Majorana fermions at the surface of a topological insulator," *Physical review letters*, vol. 100, no. 9, p. 096407, 2008.

[17] C. Nayak, S. H. Simon, A. Stern, M. Freedman, and S. D. Sarma, "Non-Abelian anyons and topological quantum computation," *Reviews of Modern Physics*, vol. 80, no. 3, p. 1083, 2008.

[18] M. Bahramy, B. Yang, R. Arita, and N. Nagaosa, "Emergence of non-centrosymmetric topological insulating phase in BiTeI under pressure," *Nature Communications*, vol. 3, p. 679, 2012.

[19] D. Shoenberg, *Magnetic oscillations in metals*. Cambridge University Press, 2009.

[20] J. Singleton, *Band theory and electronic properties of solids*, vol. 2. Oxford University Press, 2001.

[21] N. W. Ashcroft, N. D. Mermin, and S. Rodriguez, *Solid state physics*. Saunders College, 1978.

[22] I. Lifshitz and L. Kosevich, "On the theory of the shubnikov-de haas effect," *Sov. Phys. JETP*, vol. 6, pp. 67–77, 1958.

[23] K. Eto, Z. Ren, A. Taskin, K. Segawa, and Y. Ando, "Angular-dependent oscillations of the magnetoresistance in Bi2Se3 due to the three-dimensional bulk Fermi surface," *Physical Review B*, vol. 81, no. 19, p. 195309, 2010.

[24] Z. Ren, A. Taskin, S. Sasaki, K. Segawa, and Y. Ando, "Large bulk resistivity and surface quantum oscillations in the topological insulator Bi2Te2Se," *Physical Review B*, vol. 82, no. 24, p. 241306, 2010.

[25] D.-X. Qu, Y. S. Hor, J. Xiong, R. J. Cava, and N. Ong, "Quantum oscillations and Hall anomaly of surface states in the topological insulator Bi2Te3," *Science*, vol. 329, no. 5993, pp. 821–824, 2010.

[26] H. Murakawa, M. Bahramy, M. Tokunaga, Y. Kohama, C. Bell, Y. Kaneko, N. Nagaosa, H. Hwang, and Y. Tokura, "Detection of Berrys phase in a bulk Rashba semiconductor," *Science*, vol. 342, no. 6165, pp. 1490–1493, 2013.

[27] J. Park, K.-H. Jin, Y. Jo, E. Choi, W. Kang, E. Kampert, J.-S. Rhyee, S.-H. Jhi, and J. S. Kim, "Quantum oscillation signatures of pressure-induced topological phase transition in BiTeI," *Scientific reports*, vol. 5, 2015.

[28] L. Ye, J. G. Checkelsky, F. Kagawa, and Y. Tokura, "Transport signatures of Fermi surface topology change in BiTeI," *Physical Review B*, vol. 91, no. 20, p. 201104, 2015.

[29] Y. Ando, "Topological insulator materials," *Journal of the Physical Society of Japan*, vol. 82, no. 10, p. 102001, 2013.

[30] A. R. Wright and R. H. McKenzie, "Quantum oscillations and Berry's phase in topological insulator surface states with broken particle-hole symmetry," *Physical Review B*, vol. 87, no. 8, p. 085411, 2013.

[31] A. Taskin, Z. Ren, S. Sasaki, K. Segawa, and Y. Ando, "Observation of Dirac holes and electrons in a topological insulator," *Physical Review Letters*, vol. 107, no. 1, p. 016801, 2011.

[32] J. Xiong, A. C. Petersen, D. Qu, Y. S. Hor, R. J. Cava, and N. Ong, "Quantum oscillations in a topological insulator Bi2Te2Se with large bulk resistivity," *Physica E: Low-dimensional Systems and Nanostructures*, vol. 44, no. 5, pp. 917–920, 2012.

[33] Z. Ren, A. Taskin, S. Sasaki, K. Segawa, and Y. Ando, "Fermi level tuning and a large activation gap achieved in the topological insulator Bi2Te2Se by Sn doping," *Physical Review B*, vol. 85, no. 15, p. 155301, 2012.

[34] J. Xiong, Y. Luo, Y. Khoo, S. Jia, R. Cava, and N. Ong, "High-field Shubnikov–de Haas oscillations in the topological insulator Bi2Te2Se," *Physical Review B*, vol. 86, no. 4, p. 045314, 2012.

[35] F. Pobell, *Matter and methods at low temperatures*. Springer Science & Business Media, 2007.

[36] QuantumDesign, *Physical Property Measurement System hardware manual*. 2008.

[37] G. K. White, *Experimental techniques in low-temperature physics*. New York, NY; Oxford University Press, 1987.

[38] OxfordInstruments, *High field magnet system Operator's handbook*. 1993.

[39] J. Ekin, *Experimental Techniques for Low-Temperature Measurements: Cryostat Design, Material Properties and Superconductor Critical-Current Testing*. Oxford university press, 2006.

[40] A. Shevelkov, E. Dikarev, R. Shpanchenko, and B. Popovkin, "Crystal structures of bismuth tellurohalides BiTeX (X= Cl, Br, I) from X-ray powder diffraction data," *Journal of Solid State Chemistry*, vol. 114, no. 2, pp. 379–384, 1995.

[41] A. Mansour, W. Wong-Ng, Q. Huang, W. Tang, A. Thompson, and J. Sharp, "Structural characterization of Bi2Te3 and Sb2Te3 as a function of temperature using neutron powder diffraction and extended X-ray absorption fine structure techniques," *Journal of Applied Physics*, vol. 116, no. 8, p. 083513, 2014.

[42] K. S. Novoselov, A. K. Geim, S. V. Morozov, D. Jiang, M. I. Katsnelson, I. V. Grigorieva, S. V. Dubonos, and A. A. Firsov, "Two-dimensional gas of massless Dirac fermions in graphene," *Nature*, vol. 438, no. 7065, pp. 197–200, 2005.

[43] I. Walker and C. Moss, "Spot welder for making small electrical contacts," *Review of scientific instruments*, vol. 69, no. 7, pp. 2747–2756, 1998.

[44] K. Yokogawa, K. Murata, H. Yoshino, and S. Aoyama, "Solidification of high-pressure medium daphne 7373," *Japanese journal of applied physics*, vol. 46, no. 6R, p. 3636, 2007.

[45] I. Walker, "Nonmagnetic piston–cylinder pressure cell for use at 35 kbar and above," *Review of scientific instruments*, vol. 70, no. 8, pp. 3402–3412, 1999.

[46] N. Suresh and J. Tallon, "Thermodynamic properties of Pb determined from pressure-dependent critical-field measurements," *Physical Review B*, vol. 75, no. 17, p. 174502, 2007.

[47] D. Dunstan, "Theory of the gasket in diamond anvil high-pressure cells," *Review of scientific instruments*, vol. 60, no. 12, pp. 3789–3795, 1989.

[48] I. Spain and D. Dunstan, "The technology of diamond anvil high-pressure cells: Ii. operation and use," *Journal of Physics E: Scientific Instruments*, vol. 22, no. 11, p. 923, 1989.

[49] D. Dunstan and I. Spain, "Technology of diamond anvil high-pressure cells: I. principles, design and construction," *Journal of Physics E: Scientific Instruments*, vol. 22, no. 11, p. 913, 1989.

[50] H. Mao, J.-A. Xu, and P. Bell, "Calibration of the ruby pressure gauge to 800 kbar under quasi-hydrostatic conditions," *Journal of Geophysical Research: Solid Earth*, vol. 91, no. B5, pp. 4673–4676, 1986.

[51] A. Drozdov, M. Eremets, I. Troyan, V. Ksenofontov, and S. Shylin, "Conventional superconductivity at 203 kelvin at high pressures in the sulfur hydride system," *Nature*, vol. 525, no. 7567, pp. 73–76, 2015.

[52] Y. A. Bychkov and E. Rashba, "Properties of a 2D electron gas with lifted spectral degeneracy," *JETP lett*, vol. 39, no. 2, p. 78, 1984.

[53] K. Ishizaka, M. Bahramy, H. Murakawa, M. Sakano, T. Shimojima, T. Sonobe, K. Koizumi, S. Shin, H. Miyahara, A. Kimura, *et al.*, "Giant Rashba-type spin splitting in bulk BiTeI," *Nature materials*, vol. 10, no. 7, pp. 521–526, 2011.

[54] M. Kanou and T. Sasagawa, "Crystal growth and electronic properties of a 3D Rashba material, BiTeI, with adjusted carrier concentrations," *Journal of Physics: Condensed Matter*, vol. 25, no. 13, p. 135801, 2013.

[55] C. Bell, M. Bahramy, H. Murakawa, J. Checkelsky, R. Arita, Y. Kaneko, Y. Onose, M. Tokunaga, Y. Kohama, N. Nagaosa, *et al.*, "Shubnikov–de Haas oscillations in the bulk Rashba semiconductor BiTeI," *Physical Review B*, vol. 87, no. 8, p. 081109, 2013.

[56] C. Martin, E. Mun, H. Berger, V. Zapf, and D. Tanner, "Quantum oscillations and optical conductivity in Rashba spin-splitting BiTeI," *Physical Review B*, vol. 87, no. 4, p. 041104, 2013.

[57] J. Park, E. Kampert, K.-H. Jin, M. J. Eom, J. Ok, E. Choi, F. Wolff-Fabris, K. Lee, N. Hur, J.-S. Rhyee, *et al.*, "Spin-chiral bulk Fermi surfaces of BiTeI proven by quantum oscillations," *arXiv preprint arXiv:1306.1747*, 2013.

[58] I. Žutić, J. Fabian, and S. D. Sarma, "Spintronics: Fundamentals and applications," *Reviews of modern physics*, vol. 76, no. 2, p. 323, 2004.

[59] E. Bauer, G. Hilscher, H. Michor, C. Paul, E. Scheidt, A. Gribanov, Y. Seropegin, H. Noël, M. Sigrist, and P. Rogl, "Heavy fermion superconductivity and magnetic order in noncentrosymmetric CePt3Si," *Physical review letters*, vol. 92, no. 2, p. 027003, 2004.

[60] M. Tran, J. Levallois, P. Lerch, J. Teyssier, A. Kuzmenko, G. Autes, O. Yazyev, A. Ubaldini, E. Giannini, D. Van Der Marel, *et al.*, "Infrared-and Raman-spectroscopy measurements of a transition in the crystal structure and a closing of the energy gap of BiTeI under pressure," *Physical review letters*, vol. 112, no. 4, p. 047402, 2014.

[61] X. Xi, C. Ma, Z. Liu, Z. Chen, W. Ku, H. Berger, C. Martin, D. Tanner, and G. Carr, "Signatures of a pressure-induced topological quantum phase transition in BiTeI," *Physical review letters*, vol. 111, no. 15, p. 155701, 2013.

[62] D. VanGennep, S. Maiti, D. Graf, S. Tozer, C. Martin, H. Berger, D. Maslov, and J. Hamlin, "Pressure tuning the Fermi level through the Dirac point of giant Rashba semiconductor BiTeI," *Journal of Physics: Condensed Matter*, vol. 26, no. 34, p. 342202, 2014.

[63] Y. Chen, M. Kanou, Z. Liu, H. Zhang, J. Sobota, D. Leuenberger, S. Mo, B. Zhou, S. Yang, P. Kirchmann, *et al.*, "Discovery of a single topological Dirac fermion in the strong inversion asymmetric compound BiTeCl," *Nature Physics*, vol. 9, no. 11, p. 704, 2013.

[64] F. Chen, D. Zhao, Z. Xiang, C. Shang, X. Luo, B. Pan, S. Li, T. Wu, and X. Chen, "Quantum oscillations in Rashba semiconductor BiTeCl," *Physical Review B*, vol. 90, no. 20, p. 201202, 2014.

[65] M. Bahramy, R. Arita, and N. Nagaosa, "Origin of giant bulk Rashba splitting: Application to BiTeI," *Physical Review B*, vol. 84, no. 4, p. 041202, 2011.

[66] J. Lee, G. Schober, M. Bahramy, H. Murakawa, Y. Onose, R. Arita, N. Nagaosa, and Y. Tokura, "Optical response of relativistic electrons in the polar BiTeI semiconductor," *Physical review letters*, vol. 107, no. 11, p. 117401, 2011.

[67] L. J. van der Pauw, "A method of measuring specific resistivity and Hall effect of discs of arbitrary shapes," *Philips research reports*, vol. 13, pp. 1–9, 1958.

[68] D. C. Look, "Electrical characterization of GaAs materials and devices," 1989.

[69] S. Mishra, S. Satpathy, and O. Jepsen, "Electronic structure and thermoelectric properties of bismuth telluride and bismuth selenide," *Journal of Physics: Condensed Matter*, vol. 9, no. 2, p. 461, 1997.

[70] S. Nakajima, "The crystal structure of Bi2Te(3-x)Sex," *Journal of Physics and Chemistry of Solids*, vol. 24, no. 3, pp. 479–485, 1963.

[71] B. Schroeder, A. Von Middendorff, H. Köhler, and G. Landwehr, "Magneto-seebeck effect and Shubnikov-de Haas effect in n-type bismuth telluride," *physica status solidi (b)*, vol. 59, no. 2, pp. 561–568, 1973.

[72] R. Venkatasubramanian, T. Colpitts, E. Watko, M. Lamvik, and N. El-Masry, "Mocvd of Bi2Te3, Sb2Te3 and their superlattice structures for thin-film thermoelectric applications," *Journal of Crystal Growth*, vol. 170, no. 1-4, pp. 817–821, 1997.

[73] B. Yoo, C.-K. Huang, J. Lim, J. Herman, M. Ryan, J.-P. Fleurial, and N. Myung, "Electrochemically deposited thermoelectric n-type Bi2Te3 thin films," *Electrochimica acta*, vol. 50, no. 22, pp. 4371–4377, 2005.

[74] H. Köhler, "Non-parabolicity of the highest valence band of Bi2Te3 from Shubnikov-de Haas effect," *physica status solidi (b)*, vol. 74, no. 2, pp. 591–600, 1976.

[75] H. Köhler, "Non-parabolic e (k) relation of the lowest conduction band in Bi2Te3," *physica status solidi (b)*, vol. 73, no. 1, pp. 95–104, 1976.

[76] G. Thomas, D. Rapkine, R. Van Dover, L. Mattheiss, W. Sunder, L. Schneemeyer, and J. Waszczak, "Large electronic-density increase on cooling a layered metal: Doped Bi2Te3," *Physical Review B*, vol. 46, no. 3, p. 1553, 1992.

[77] G. Wang and T. Cagin, "Electronic structure of the thermoelectric materials Bi2Te3 and Sb2Te3 from first-principles calculations," *Physical Review B*, vol. 76, no. 7, p. 075201, 2007.

[78] B.-L. Huang and M. Kaviany, "Ab initio and molecular dynamics predictions for electron and phonon transport in bismuth telluride," *Physical Review B*, vol. 77, no. 12, p. 125209, 2008.

[79] V. Sologub, M. Shubnikov, E. Itskevich, L. Kashirskaya, R. Parfen'ev, and A. Goletskaya, "Change of Bi2Te3 band structure under hydrostatic compression," *Soviet Journal of Experimental and Theoretical Physics*, vol. 52, p. 1203, 1980.

[80] N. Brandt and V. Kulbachinskii, "Pressure spectroscopy of impurity states and band structure of bismuth telluride," *Semiconductor science and technology*, vol. 7, no. 7, p. 907, 1992.

[81] E. Itskevich, L. Kashirskaya, and V. Kraidenov, "Anomalies in the low-temperature thermoelectric power of p-Bi2Te3 and Te associated with topological electronic transitions under pressure," *Semiconductors*, vol. 31, no. 3, pp. 276–278, 1997.

[82] I. Lifshitz *et al.*, "Anomalies of electron characteristics of a metal in the high pressure region," *Sov. Phys. JETP*, vol. 11, no. 5, pp. 1130–1135, 1960.

[83] Y. M. Blanter, M. Kaganov, A. Pantsulaya, and A. Varlamov, "The theory of electronic topological transitions," *Physics Reports*, vol. 245, no. 4, pp. 159–257, 1994.

[84] Y. Yamaji, T. Misawa, and M. Imada, "Quantum and topological criticalities of lifshitz transition in two-dimensional correlated electron systems," *Journal of the Physical Society of Japan*, vol. 75, no. 9, p. 094719, 2006.

[85] A. Nakayama, M. Einaga, Y. Tanabe, S. Nakano, F. Ishikawa, and Y. Yamada, "Structural phase transition in Bi2Te3 under high pressure," *High Pressure Research*, vol. 29, no. 2, pp. 245–249, 2009.

[86] A. Polian, M. Gauthier, S. M. Souza, D. M. Trichês, J. C. de Lima, and T. A. Grandi, "Two-dimensional pressure-induced electronic topological transition in Bi2Te3," *Physical Review B*, vol. 83, no. 11, p. 113106, 2011.

[87] M. Jacobsen, S. Sinogeikin, R. Kumar, and A. Cornelius, "High pressure transport characteristics of Bi2Te3, Sb2Te3, and BiSbTe3," *Journal of Physics and Chemistry of Solids*, vol. 73, no. 9, pp. 1154–1158, 2012.

[88] J. Zhang, C. Liu, X. Zhang, F. Ke, Y. Han, G. Peng, Y. Ma, and C. Gao, "Electronic topological transition and semiconductor-to-metal conversion of Bi2Te3 under high pressure," *Applied Physics Letters*, vol. 103, no. 5, p. 052102, 2013.

[89] F. Manjon, R. Vilaplana, O. Gomis, E. Pérez-González, D. Santamaría-Pérez, V. Marín-Borrás, A. Segura, J. González, P. Rodríguez-Hernández, A. Muñoz, *et al.*, "High-pressure studies of topological insulators bi2se3, bi2te3, and sb2te3," *physica status solidi (b)*, vol. 250, no. 4, pp. 669–676, 2013.

[90] S. Zhang, J. Zhang, X. Yu, J. Zhu, P. Kong, S. Feng, Q. Liu, L. Yang, X. Wang, L. Cao, *et al.*, "The comprehensive phase evolution for Bi2Te3 topological compound as function of pressure," *Journal of Applied Physics*, vol. 111, no. 11, p. 112630, 2012.

[91] A. A. Taskin and Y. Ando, "Berry phase of nonideal Dirac fermions in topological insulators," *Physical Review B*, vol. 84, no. 3, p. 035301, 2011.

[92] D. Donnelle and B. Rust, "The fast fourier transform for experimentalists. part i. concepts," *Computing in Science & Engineering*, vol. 7, no. 2, pp. 80–88, 2005.

[93] C. Hurd, *The Hall effect in metals and alloys*. Springer Science & Business Media, 2012.

[94] E. Fawcett, "High-field galvanomagnetic properties of metals," *Advances in Physics*, vol. 13, no. 50, pp. 139–191, 1964.

[95] A. B. Pippard, *Magnetoresistance in metals*, vol. 2. Cambridge University Press, 1989.